Using zircons to disentangle back-veining and hybridization of diorite dykes: an example from the Gangdese Arc, Tibet

Roberto Weinberg, Jean-François Moyen, Jian-Kang Yi, Di-Cheng Zhu, Oliver Nebel, Shaorong Chen, Qiang Wang

OXFORD UNIVERSITY PRESS | Journal of Petrology

Draft Manuscript for Review

Using zircons to disentangle back-veining and hybridization of diorite dykes: an example from the Gangdese Arc, Tibet

Journal:	*Journal of Petrology*
Manuscript ID	JPET-Jan-22-0002.R2
Manuscript Type:	Original Manuscript
Date Submitted by the Author:	n/a
Complete List of Authors:	Weinberg, Roberto; Monash University, School of Earth, Atmosphere and Environment Moyen, Jean-Francois; Laboratoire Magmas et Volcans; OPGC, CNRS, Université Jean Monnet, Yi, Jian-Kang; China University of Geosciences, Beijing Zhu, Dicheng; China University of Geosciences, Beijing, Nebel, Oliver; Monash University, School of Earth, Atmosphere and Environment Chen, Shaorong; China University of Geosciences, Beijing Wang, Qing; China University of Geosciences Beijing, ;
Keyword:	zircon, zircon saturation temperature, magma hybridization, magma mingling, geothermometry
Journal of Petrology now offers Virtual Collections of published papers. You may choose up to three collections from the list below. Virtual collections will increase the visibility of your work.:	Continental Collision Zones < Province Themes, Continental Crustal Genesis and Evolution < Process Themes, Partial Melting < Process Themes

Using zircons to disentangle back-veining and hybridization of diorite dykes : an example from the Gangdese Arc, Tibet

Roberto F. Weinberg[1*], Jean-François Moyen[2], Jian-Kang Yi[3], Di-Cheng Zhu[3], Oliver Nebel[1], Shaorong Chen[3], Qiang Wang[3]

[1]School of Earth, Atmosphere and Environment, Monash University, Clayton, VIC, 3800, Australia.

[2] Université de Lyon, Laboratoire Magmas et Volcans, UJM-UCA-CNRS-IRD, 23 rue Dr. Paul Michelon, 42023 Saint Etienne, France

[3] State Key Laboratory of Geological Processes and Mineral Resources, China University of Geosciences, Beijing 100083, China

*Corresponding author Telephone: +61 3 9905 4902. Fax: +61 3 9905 4903. E-mail: Roberto.weinberg@monash.edu

ABSTRACT

Thermo-chemical modelling and chemical data suggest that the genesis of arc melts commonly involves re-melting of older intrusions, triggered by the injection of mantle-derived melts, followed by magma mixing. Remelting and mixing may lead to complex zircon populations, which can be used to gain insights into the conditions of mixing. This paper investigates a case where such processes can be studied through the compositional and thermal record provided by zircons preserved in a diorite dyke swarm that remelted host rock tonalites in the Gangdese Batholith in Tibet. Autocrystic zircons from the diorite yield consistent ages of 46-47 Ma even though they can be altered, having highly enriched trace elements, reaching ~1 wt% in Fe, Ca, Y, U, Th, and anomalously high values of LREE and Ti. Granitic magmas derived from the tonalite, back-veined the dykes and mixed with the dioritic mush, transferring small quantities of 77-79 Ma zircon xenocrysts. The xenocrysts are euhedral with little evidence for resorption, indicating they were apparently stable during the process of tonalite anatexis and transfer to the diorite magma. This requires that: (i) tonalite melting occurred at low temperatures with minimal zircon dissolution, and (ii) the diorite either cooled rapidly before significant resorption of the grains or was already saturated in zircon when mixing occurred. Zircon saturation temperatures of the diorite are relatively low, indicating that xenocrystic zircons were transferred to a highly crystalline dioritic mush. This requires either liquefaction by injection of the back-veining felsic magma to allow for mixing or pervasive throughflow of the diorite mush by the felsic magma leaving behind zircon xenocrysts. The findings suggest that the dykes triggered low-T, water-fluxed melting of the host tonalite, and that these anatectic melts invaded the diorite mush initially through the interstices leading to mixing and this may have caused the breakdown of the crystalline framework leading to liquefaction and renewed magma flow. Dyking and assimilation of wall-rock through back-veining as recorded in these rocks could be common in transcrustal arcs. However, this process could be hidden due to a combination of the

similarity in the isotopic and chemical nature of arc rocks, and resorption of zircon xenocrysts during mixing. This process may explain some complex chemistry of arc magmatic rocks and their minerals that are not easily explained by endmember models, such as pure re-melting of older arc rocks or fractional crystallization of mantle-derived melts.

Key words: geothermometry; magma hybridization: magma mingling; zircon; zircon saturation temperature

INTRODUCTION

The origin of granitic magmas in arcs is at the center of a long-standing debate focused on whether they are derived from the fractionation of basaltic magmas (Jagoutz & Klein, 2018, Müntener & Ulmer, 2018), or the remelting of older arc intrusions (Collins *et al.*, 2020, Moyen *et al.*, 2021, Symington *et al.*, 2014, Weinberg & Dunlap, 2000b) or magma mixing (Reubi & Blundy, 2009). In this regard, evidence for zircon recycling through the system as xenocrysts and antecrysts, combined with Ti-in-zircon thermometry and zircon saturation temperatures, can be used to explore and constrain the processes controlling arc magma evolution, such as whether mixing or assimilation processes were involved and when and how they occurred. The term xenocryst refers here to zircon incorporated from the surrounding host rocks during magma transit and emplacement, whereas the term antecrysts refers to zircon formed in an earlier pulse of magma and that was transferred to the current host. The term autocryst refers to zircon crystallized from the host magma (Miller *et al.*, 2007).

Zircon has a number of properties that makes it useful in constraining magmatic processes. It is an excellent marker of the time of magma crystallization, and its trace elements indicate contemporaneous crystallization or dissolution of other minerals (Rubatto & Hermann, 2007). Its Hf isotopic composition is a sensitive indicator of melt sources and mixing between magmas from different sources (Kemp *et al.*, 2007), and in the case of xenocrystic zircon, Hf isotopic

ratio can be used to determine its source. Further to that, Ti-in-zircon thermometry (Watson *et al.*, 2006), in combination with zircon saturation temperatures of magma (Boehnke *et al.*, 2013, Watson & Harrison, 1983), constrain magma crystallization histories (Schiller & Finger, 2019) and the conditions prevalent during fractionation and mixing (Barnes *et al.*, 2019, Harrison *et al.*, 2007, Miller *et al.*, 2003, Miller *et al.*, 2007, Siégel *et al.*, 2018). These data can then be linked to modeling of the chemical evolution of melt and crystals during crystallization to define zircon saturation temperature and the expected Ti-content of zircons (Barnes *et al.*, 2019, Lee & Bachmann, 2014).

There is often a mismatch between temperatures derived from Ti-in-zircon and from zircon saturation. In samples with many zircon xenocrysts, this mismatch can be caused by the added Zr. In samples with few or no xenocrysts, the mismatch can be caused either by fractional crystallization that changes the Zr content and composition of the interstitial melt, or by changes in the total Zr content through accumulation of zircons and other minerals, or through loss of Zr-rich interstitial melt (Barnes *et al.*, 2019). Zircon saturation temperatures unaccompanied by modeling of fractional crystallization have been used to suggest that arc granites typically record relatively low zircon saturation temperatures, and to postulate that granitic arc magmas are typically cold (<800 ^{o}C), derived from water-fluxed re-melting of older arc rocks (Collins *et al.*, 2016, Collins *et al.*, 2020). However, zircon saturation temperature is strongly dependent on the initial Zr content of the magma and the evolution of the residual melt composition during crystallization (Miller *et al.*, 2003).

In this paper, we explore the nature of zircon autocrysts in diorite dykes and the fate of zircon xenocrysts transferred from the host rock as a result of anatexis of the host rock, back-veining and mixing, in an outcrop in the Gangdese Batholith in Tibet (Zhu *et al.*, 2015). We use zircon U-Pb ages and grain morphology, combined with zircon saturation temperatures and Ti-in-zircon thermometry to constrain the thermal conditions and magma crystallinity during mixing.

The discussion is underpinned by compositional modelling of a crystallizing melt and the trace element composition of zircons in the evolving melt.

The paper starts with a brief description of the Gangdese Batholith and field relationships between the diorite dykes and host rocks investigated here, including the back-veining and hybridization of the dykes caused by melting of the host. The methodology is then described, followed by characterization of the tonalite and diorite samples and their zircons, including U-Pb dating, Hf-isotope and trace element composition. Whole-rock chemistry is used as the basis for modeling diorite magma crystallization and determining zircon saturation temperatures, as well as to model tonalite melting occurring as the diorite cooled. Modelled zircon saturation temperatures and zircon trace element compositions are also derived from these models and form the basis for discussion of the timing of magma mixing and xenocryst transfer, and the validity of Ti-in-zircon thermometry for these zircons. Results show how these approaches combined can be used to cast light on both the physical details of hybridization, and to exemplify some of the pitfalls associated with interpreting the data.

GANGDESE BATHOLITH AND DABU GEOLOGY

The Gangdese Batholith (Fig. 1) and its western continuation in NW India and Pakistan, the Ladakh and Kohistan Batholiths, is a 2500 km-long calc-alkaline magmatic arc that extends across the southern Tibetan Plateau. It is an Andean-type continental arc formed as a result of oceanic subduction of the Neo-Tethys oceanic lithosphere under the Lhasa Terrane at the Asian continental margin until collision with India at 55 ± 5 Ma shut down the arc (Ji *et al.*, 2009, Yin & Harrison, 2000, Zhu *et al.*, 2019). Magmatism started at ~210 Ma and continued intermittently until collision ended typical subduction-related magmatism and initiated post-collisional magmatism. Subduction-related magmatism is marked by two intense pulses of magmatic activity, one at 90 ± 5 Ma and the other at 55-50 Ma (Zhu *et al.*, 2019). The 90 ± 5

Ma event is linked with ridge subduction (Zhang *et al.*, 2010) or slab rollback (Ma *et al.*, 2013) of the Neo-Tethyan oceanic lithosphere, whereas the 55-50 Ma event is attributed to collision followed by slab breakoff (Zhu *et al.*, 2019) or lithosphere removal (Kapp & DeCelles, 2019). The dykes investigated here belong to the syn-collisional event, which was the most intensive magmatic pulse in the Gangdese belt (Zhu *et al.*, 2019), and includes the voluminous Linzizong volcanic successions (Zhu *et al.*, 2015). Oligocene-Miocene post-collisional magmatism was dominated by silicic rocks resulting from the remelting of arc magmatic rocks and their hybridization with metasomatized lithospheric mantle-derived ultrapotassic melts (e.g. Wang *et al.*, 2018).

Magmatic rocks from the 90 ± 5 Ma events show coherent "depleted mantle-like" zircon $\varepsilon_{Hf}(t)$ (+15 to +10) and positive whole-rock $\varepsilon_{Nd}(t)$ (around +3.0) with a few outliers (Ji *et al.*, 2009, Ma *et al.*, 2013, Zhang *et al.*, 2020, Zhu *et al.*, 2011) that may reflect varying degrees of incorporation of ancient crustal components from the Gangdese basement into the juvenile magmas. Rocks related to the 55 ± 5 Ma event are characterized by a wide range in zircon $\varepsilon_{Hf}(t)$ (between -6 and +15)(Zhu *et al.*, 2022) and whole-rock ε_{Nd} (mostly from +5.0 to −3.0). This more evolved isotopic signature has generally been attributed to the involvement of Indian continent-derived materials (Chu *et al.*, 2011, Wang *et al.*, 2015).

Rocks of the Gangdese arc only rarely have zircon xenocrysts (Zhu *et al.*, 2015). To our knowledge no xenocrysts have been reported in syn-collisional plutonic rocks in this arc and only a few have been reported for the Linzizong volcanic rocks (a few xenocrysts formed at ~90 Ma and older, Zhu *et al.*, 2015). This contrasts with rocks from the Ladakh Batholith, the western continuation of the Gangdese Batholith, which show migmatization and where zircons define a ca. 20 Ma age range (Weinberg & Dunlap, 2000a, White *et al.*, 2011) including recycling of 68 Ma zircons in a 49 Ma magma. Despite this exception, the general rarity of zircon xenocrysts could indicate that: a) remelting of older arc intrusions is a minor process

(Jagoutz & Klein, 2018), b) because zircons are rare in mafic arc rocks, few or no zircons are passed on to the felsic magmas they produce upon remelting, or c) zircon xenocrysts are resorbed during relatively high-temperature melting (Miller *et al.*, 2003).

This paper focuses on an outcrop of the Gangdese Batholith along the road from Zedong to Nyingchi (Fig. 1a) at N29.2625 º and E92.4119 º close to Dabu village. Here, a diorite dike swarm (Fig. 2a, b) intrudes a homogeneous leucocratic tonalite and is back-veined by magmas resulting from the melting of the tonalite host. The dykes are typically 1-3 m wide and are continuous for more than 100 m. In detail, the dyke contacts are irregular at the dm-cm scale, and back-veined (Fig. 2c, d) and dyke tips narrow considerably over a few metres. At the contact, the tonalite has a centimetric layer of more felsic and finer-grained granitic rock that is continuous with dykelets intruding the diorite (Fig. 2c). These dykelets are irregular and intrude and gradually vanish into a heterogeneous diorite (Fig. 2e, f). We have determined whole-rock chemistry and investigated zircons from three samples of diorite and three samples of tonalite host rock, all homogeneous at hand-specimen scale.

METHODOLOGY

Whole-rock geochemical analysis

Fresh rocks samples were crushed, hand-picked, and then powdered using an agate mill to a grain size < 200 mesh at the Yuneng Mineral Separation Service Company at Langfang, Hebei Province, China. Major element analyses of whole rock were conducted on Agilent 7700e ICP-MS at the Wuhan SampleSolution Analytical Technology Co., Ltd., Wuhan, China. The sample pre-treatment of whole rock major element analysis was made by melting method. The detailed sample-digesting procedure was as follows: (1) Sample powder (200 mesh) was placed in an oven at 105 ℃ for drying of 12 hours; (2) ~1.0g dried sample was accurately weighed and placed in the ceramic crucible and then heated in a muffle furnace at 1000℃ for 2 hours. After

cooling to 400℃, this sample was placed in the drying vessel and weighted again in order to calculate the loss-on-ignition (LOI); (3) 0.6 g sample powder was mixed with 6.0 g flux and 0.3 g oxidant (NH4NO3) in a Pt crucible, which was placed in the furnace at 1050℃ for 15 minutes. The flux is a mixture of lithium tetraborate, lithium metaborate and lithium fluoride (45:10:5). Then, this molten sample was quenched in air for 1 minute to produce flat discs on the fire brick for the XRF analyses.

Zsx Primus II wavelength dispersive X-ray fluorescence spectrometer (XRF) produced by RIGAKU, Japan, was used for the analysis of major elements in the whole rock, The X-ray tube is a 4.0Kw end window Rh target. The analytical conditions were voltage: 50kV, current: 60mA. All major element analysis lines are Kα. The standard curve uses the national standard material of China, rock standard sample: GBW07101-14. The data were corrected by the theoretical α coefficient method. The relative standard deviation (RSD) is less than 2% and the average bias of the measurements was of -0.1% for SiO_2 and has its highest values of + 1.3% for MgO and -1.6% for P_2O_5.

Trace element analyses of whole rock were conducted on Agilent 7700e ICP-MS at the Wuhan SampleSolution Analytical Technology Co., Ltd., Wuhan, China. Four rock reference materials (AGV-2, BHVO-2, BCR-2, and RGM-2) were used to calibrate the contents of trace elements of analytical samples. The detailed sample-digesting procedure was as follows: (1) Sample powder (200 mesh) was placed in an oven at 105 ℃ for drying of 12 hours; (2) 50 mg sample powder was accurately weighed and placed in a Teflon bomb; (3) 1 ml HNO_3 and 1 ml HF were slowly added into the Teflon bomb; (4) Teflon bomb was placed in a stainless steel pressure jacket and heated to 190 ℃ in an oven for >24 hours; (5) after cooling, the Teflon bomb was opened and placed on a hotplate at 140 ℃ and evaporated to incipient dryness, and then 1 ml HNO_3 was added and evaporated to dryness again; (6) 1 ml of HNO_3, 1 ml of MQ water and 1 ml internal standard solution of 1ppm In were added, and the Teflon bomb was resealed and placed in the

oven at 190 ℃ for >12 hours; (7) the final solution was transferred to a polyethylene bottle and diluted to 100 g by the addition of 2% HNO_3.

LA-ICP-MS zircon U-Pb dating and trace element analysis

Zircons were separated using conventional and magnetic techniques at the Yuneng Mineral Separation Service Company at Langfang, Hebei Province, China. Cathodoluminescence (CL) images, obtained at the Institute of Geology, Chinese Academy of Geological Sciences (Beijing), were used to check the internal textures of single zircons and to select suitable positions for U-Pb dating and Hf isotope analysis. The zircon U–Pb isotope and trace element analyses were carried out using LA-ICP-MS at the Mineral Laser Microprobe Analysis Laboratory (Milma Lab), China University of Geosciences (Beijing). Detailed analytical procedure was described by Zhang et al. (2019) and provided in Supplementary Data Electronic Appendix 1 (all the Electronic Appendices may be downloaded from http://www.petrology.oupjournals.org/). A beam diameter of 35 μm was used for the first round of analyses, whereas for the second round 35 μm was only used for sample 17DB01-2 used and 25 μm for the remainder, which was also used for the third round. Zircon 91500 was used as an external standard for correcting U–Pb dating, and glass NIST 610 was used as an external standard for trace element calibration. Off-line analyses were performed using an Excel-based software ICPMSDataCal (Liu *et al.*, 2008, Liu *et al.*, 2010). Uncertainties in trace element measurements are between 5 and 10%. Common Pb correction was calculated using the program ComPbCorr#3.17 (Andersen, 2002). Concordia diagrams and mean calculations were made using ISOPLOT (v. 3.0) (Ludwig, 2003). Samples were analysed during three sessions, but they gave similar results (Supplementary Data Electronic Appendix 2) and so we present merged results.

Zircon Hf isotopic analysis

Zircon Hf isotopic analyses were conducted in the same domain of the grain as for U-Pb analyses, as defined by CL images. Analyses used a Neptune Plus MC–ICP–MS (Thermo Fisher Scientific, Germany), coupled to a New Wave 193 excimer ArF laser–ablation system at the Milma Lab, China University of Geosciences (Beijing) with a beam size of 35 μm, laser pulse frequency of 8 Hz and energy density of 3.7 J/cm^2. Makeup gas of argon and carrier gas of helium with the addition of nitrogen mixed in a T–branch pipe prior to introduction into the MC–ICP–MS. In the experiment, L4 to H3 Faraday cups were used to collect ^{171}Yb, ^{173}Yb, ^{175}Lu, ^{176}Hf, ^{177}Hf, ^{178}Hf, ^{179}Hf, and ^{180}Hf, respectively with the integration time of 0.131 s. The carrier and makeup gas flows were optimized by a line scan (spot size of 35 μm and scan speed of 5 μm/s) ablating NIST SRM 610 to obtain maximum signal intensity for ^{232}Th, while minimizing ^{232}Th^{16}O/^{232}Th ratio. For each analysis, 50 s integration for gas blank and 50 s integration for signal collection were set up with a total of 800 cycles of raw data. Zircon 91500 (Blichert-Toft, 2008) was used as an external standard for correcting mass discrimination. Zircon standard Plešovice (Sláma *et al.*, 2008) and GJ-1 (Morel *et al.*, 2008) were analyzed as unknown sample that were inserted between zircon 91500 and the samples. Raw data was converted by Neptune Plus software and then processed using Iolite software (Paton *et al.*, 2011).

The initial ^{176}Hf/^{177}Hf ratios and $\varepsilon_{Hf}(t)$ values were calculated with reference to the chondritic reservoir (CHUR) at the time of zircon growth from the magmas. The decay constant for ^{176}Lu of 1.867×10^{-11} year^{-1} (Söderlund *et al.*, 2004), the chondritic ^{176}Hf/^{177}Hf ratio of 0.282785 and ^{176}Lu/^{177}Hf ratio of 0.0336 (Bouvier *et al.*, 2008) were adopted. Depleted mantle model ages (T_{DM}) were calculated with reference to the depleted mantle at a present–day ^{176}Hf/^{177}Hf ratio of 0.28325, and ^{176}Lu/^{177}Hf = 0.0384 (Griffin *et al.*, 2000). The Hf isotope crustal model age (T_{DM}^{C}) was calculated by assuming that its parental magma was derived from an average

continental crust, with $^{176}Lu/^{177}Hf = 0.015$, that originated from the depleted mantle source (Griffin *et al.*, 2002).

SAMPLES: GEOCHEMISTRY AND PETROGRAPHY

Six samples were investigated: three diorites and three tonalites (see Supplementary Data Electronic Appendix 3 for photographs of the sampling location; coordinates N29.263 and E92.4112). All diorite samples are homogeneous dark grey, and tonalite samples are white to light grey. Whole-rock chemistry in Table 1 shows that the diorites are of intermediate composition ($53 < SiO_2 < 58$ wt.%) and the tonalites felsic ($SiO_2 = 68$-69 wt.%). The rocks have $K_2O/Na_2O < 1$, and both rock types are magnesian and calc-alkalic, based on Frost et al. (2001) descriptors (Fig. 3). The diorites are metaluminous, and the tonalites weakly peraluminous (ASI 1.00 to 1.05) (Fig. 3). Trace elements for both rock types are similar, with negative anomalies of Nb and positive anomalies of Pb and Sr in MORB-normalized diagrams (Fig. 4, Ta also defines a negative anomaly, not shown). HREE exhibit low values of 0.1 – 1 times MORB values, and are lower in the tonalites than in the diorites. All samples have Zr/Hf between 35.6 and 40.7, and La/Yb (not normalized) between 7 and 31 for the tonalite and 6 to 13 for the diorite. Although the two rock types were emplaced some 30 Myr apart (see section 7 below), they display very similar geochemical properties, consistent with their arc setting.

The diorite dykes are fine-grained and massive, and are composed of plagioclase (~70%-75%), biotite (~15%-20%), amphibole (~10%-15%) and quartz (~5%-10%). Plagioclase is zoned with lamellar twinning and the grains are subhedral to euhedral, 100 to 400 μm long, some reaching 1 mm in length, tending towards subequant grains, with crystal faces in some places forming mosaics with 120° intersection between grains. Amphibole is twinned, anhedral to subhedral, with green to brown pleochroism and 50-1500 μm long (generally 100-200 μm). In sample 18DB01-4, the longer Hbl grains include biotite grains. Biotite is subhedral to euhedral, with

light-brown to dark-brown pleochroism, forming isolated grains with rectangular sections 100-1000 μm long (generally 300-400 μm), or forming aggregates with hornblende. The accessory minerals are apatite, zircon, epidote and opaque minerals, and sample 17DB01-2 has titanite. Diorite zircon grains have inclusions and cavities and typically appear in the felsic matrix rather than as inclusions in the mafic minerals, which lack pleochroic haloes. The nature of the zircon grains is described in the next subsection. Apatite forms needles reaching 300-400 μm, occasionally 600 μm, mostly in the felsic matrix, but can be found included in hornblende and biotite. Epidote grains can be either included in biotite as subhedral grains, possibly primary, or in the felsic matrix where it could be a result of alteration of plagioclase. The tonalite is medium grained (grain-size: 1 to 2 mm), lacking a foliation and is composed of plagioclase (~60%-70%), quartz (~20%-30%), biotite (~5%-8%), minor K-feldspar, and with apatite, zircon in among the felsic minerals, and Fe-Ti oxides as accessory phases. Samples 18DB01-3 and 18DB01-1 also have titanite. Plagioclase occurs mainly as subhedral to euhedral laths. Biotite is anhedral to subhedral and displays yellowish to dark-brown pleochroism.

ZIRCON CATHODOLUMINESCENCE

Zircons from the tonalite typically vary in size from 150 to 250 μm (ranging from 100 to 400 μm) and are bipyramidal prismatic with well-developed, fine oscillatory zoning (Fig. 6), or common sector zoning, with some internal truncation of early zonation. Zircons from the diorite vary in size from 100 to 400 μm and the majority of grains have roughly rectangular shapes defined by two parallel rationale faces, forming the longer sides of the rectangle, and two shorter, irregular sides. Some grains have a pyramidal ending. Samples 18DB01-4 and 18DB01-2 have a second morphological type of zircon comprising euhedral grains, with well-developed, fine prismatic oscillatory and sector zoning, similar to zircons from the tonalites (compare grains in Fig. 6c and xenocrysts in Fig. 6d). The latter are considered xenocrysts and comprise 7% of the population (11 grains out a total 162 in the mount for sample 18DB01-4). From this

we estimate that they add only ~ 5 ppm Zr to the 74 ppm content of the whole rock for this sample. Sample 18DB01-2 has an even smaller proportion of these xenocrystic zircons. We neglect this added amount when considering zircon saturation temperatures below.

CL images of zircons from the diorite define three distinct zircon groups (excluding the xenocrysts in samples 18DB01-4 and 18DB01-2): a) clean and grey grains; b) grains with considerable clean, grey parts and with metamict domains with cauliflower-like pattern and partly quenched to black CL; and c) fully metamict grains with or without very thin grey rims (Fig. 6) that are either entirely or mostly quenched, preserving weak cauliflower-like patterns in very dark regions. Based on these distinctions, the spots were divided into 4 types depending on their position: Type 1 are from clean and grey areas in grains from group (a); Type 2 are spots from the clean, grey part of grains from group (b), and Type 3 are from the metamict part of the same grains; and Type 4 are spots from fully metamict, quenched grains of group (c). Types 3 and 4 are commonly associated with anomalous zircon trace element compositions as we will see in the next subsection.

ZIRCON GEOCHEMISTRY

Zircons from the tonalite host rock and xenocrysts from diorites have similar trace element composition, with U and Th contents below 2100 and 1800 ppm, respectively, similar REE patterns (Fig. 7, Supplementary Data Electronic Appendix 2), and Ti contents between 1 and 10 ppm (Supplementary Data Electronic Appendix 2). These values contrast starkly with the autocrysts from the diorite that show higher abundances of REE (Fig. 7) and anomalously high values of U-Th-Ca-Fe-Y, each with values approaching or surpassing 1 wt.% (Fig. 8) (for more zircons with high trace element contents see Gagnevin *et al.*, 2010). Their Ti contents are between 1 and >500 ppm (15 out 260 analyses yielded Ti > 30 ppm) (Fig. 8d).

Hafnium is an incompatible element during crystallization of felsic magmas (Claiborne *et al.*, 2010), with a bulk partition coefficient remaining below one even during zircon crystallization, despite zircon's high Hf uptake. Conversely, titanium, is a compatible element that enters mafic silicates and common accessories, such as Fe-Ti oxides and titanite. Thus, during magma crystallization, Hf increases while Ti decreases in the melt leading to the negative trend of Hf against Ti in Fig. 9. The same is not true for U, Th and Yb, which show unexpected positive trends against Ti, for diorite zircons, indicative of an apparently compatible behaviour of these elements during crystallization (Fig. 9), contrasting with the incompatible trends in Claiborne et al. (2010).

ZIRCON U-Pb AGES AND Hf ISOTOPES

The three tonalite and three diorite rock samples in Table 1were dated. The diorite samples yielded ages of 46-47 Ma and the tonalite samples yielded ages of 77-79 Ma and (Figs. 10 and 11). Given the close mean ages for the diorite samples and their relatively large spread, indicated by high MSWDs (>4), we consider that the dykes were essentially contemporaneous. Zircons with CL types 3 and 4 with quenched, metamictic CL features, tend to be richer in U, Th and other trace elements compared to types 1 and 2 (Fig. 8). In order to determine if types 3 and 4 have been affected by Pb-loss, U-Pb dates were compared with those for CL types 1 and 2 (Figs. 10d and 12). Results show no significant differences and dates vary from ~44 to 51 Ma independently of CL type. We have therefore considered all concordant U-Pb analyses.

Two tonalite samples have ages that overlap within error at ~79 Ma and have small MSWD (Fig. 11a,c). The third sample, however, has a slightly younger mean age at 77.2 ± 0.5 Ma and a high MSWD=4.8 (Fig. 11b). This sample has three times more analyses than the other two, suggesting that the tonalites may have a large true spread in dates. Two of the three diorite samples (Fig. 11d-e) have xenocrysts with the same range of dates and same trace element

chemistry as the tonalite zircons (Fig. 7) confirming the interpretation based on CL images (Fig. 6). Analyses with >10% discordancy as well as a small number of outliers were not considered here.

Hafnium isotopes for subpopulations of the dated zircons from all 6 samples were obtained. They are typical of those of the Gangdese arc yielding $\varepsilon_{Hf(t)}$ between +4 and +13 (*Fig. 13; Supplementary Data Electronic Appendix 2*). The values for the tonalites are similar to those of the diorite with the exception that the latter have a wider variation (+4 to +13 compared to +6 to +10). Xenocrysts of diorite sample 18DB01-4 plot together with the tonalite zircons.

CHEMICAL MODELLING OF MELT EVOLUTION AND ZIRCON CRYSTALLIZATION

Methods

The crystallization of zircons during cooling of magmas has been modelled using a procedure similar to the ones described by Schiller and Finger (2019) (see also Harrison *et al.*, 2007, Kirkland *et al.*, 2021). In a cooling closed system, magma crystallizes and the residual melt evolves chemically. Zr is initially incompatible and its content increases until zircon becomes saturated at which point it becomes compatible and starts decreasing in the melt upon further fractionation. Thus, zircon crystallizes out of this residual melt, whose composition evolves and differs from the composition of the bulk rock. In a closed-system, the melting process upon heating follows the opposite direction to the one described above.

In our models, we first calculate the closed-system evolution of the rock using phase equilibria, and in particular the amount and composition of the residual melt at a given temperature. Zr is partitioned between melt and solids using known partition coefficients, and the Zr content in the melt is compared with the zircon saturation value; any Zr above the saturation value at this point

354 is then used to form zircon. Other trace elements are then partitioned between liquid and all
355 solids, zircon included. The most important assumptions in this process are that the composition
356 of the diorite and tonalite correspond to melt compositions, and that this is a closed system
357 behaviour, i.e. we assume batch rather than fractional crystallization (or indeed batch melting, as
358 both are exactly similar in a closed system): neither melt nor crystals are removed from the
359 system, and the system properties are calculated independently for each point.

360 The details of the procedure are given in Supplementary Data Electronic Appendix 5. Phase
361 equilibrium is modelled using PerpleX version 6.9.0 (Connolly, 2005, Connolly & Petrini,
362 2002) and the minerals and melt models by Holland et al. (2018), that allow incorporation of
363 Fe^{3+} and Ti, using one-dimensional T profiles at a fixed P of 5 kbar. Zircon saturation values are
364 based on the saturation model of Boehnke et al. (2013) and results for the model of Watson and
365 Harrison (1983) are also shown for comparison. These models include a dependence on the melt
366 composition expressed as the parameter M, the cation ratio (Na + K + 2Ca)/(Al x Si), which is
367 obtained from the phase equilibrium model. Partition coefficient values for trace elements vary
368 considerably in the literature. We use those compiled by Laurent (2012), using values for felsic
369 rocks (SiO_2 > 63 %), which are appropriate for both rock types since the residual melt, even in
370 the diorite, is almost always at these values. For Th, U, HFSE and REE, the zircon-melt
371 partition coefficients are modified using the temperature parametrization of Claiborne et al.
372 (2018). Temperature-dependent coefficients for other minerals are unavailable and have the
373 potential to modify our results. Finally, we calculated Ti contents in zircon as a function of
374 temperature using the model of Ferry and Watson (2007). As their equation relies on the activity
375 of Si and Ti, both were calculated from the phase equilibrium model (following Schiller &
376 Finger, 2019). PerpleX outputs chemical potentials that must be converted into activities.

377 Given the pressure dependence of ~5 ^{o}C/kb for the Ti-in-zircon thermometer determined by
378 Ferry and Watson (2007), our calculated temperatures could be overestimates for the lower

pressure used here (5 kb) compared to the 10 kb used in Ferry and Watson's calibration. All parameters are calculated along the 1D temperature profile used for phase equilibrium, simulating closed-system cooling (or heating) of the magma or the rock. After the phase equilibrium modelling, all steps are performed using a homemade R script (available from J-F Moyen on request).

Evolution of melt and zircon

Crystallization of a melt in a closed system is modelled using diorite sample 18DB01-4, the most mafic of the diorites with 54% SiO_2 and 73 ppm Zr. We carried out two calculations, with 3 and 6 % H_2O. A value close to the average of the tonalite samples was used with SiO_2 = 68.3 % and 140 ppm Zr (Table 1). A low H_2O content of 2 wt.% was assumed for modelling the tonalite in order to investigate its remelting triggered by limited quantities of H_2O delivered from the diorite intrusion.

In the model, the diorite crystallizes Amp-Pl-Cpx accompanied later by Bt that increases in proportion towards the end of the crystallization history, with quartz appearing close to the solidus temperature (T_{sol} =677 ^oC; Fig. 14a). Water saturation is reached at 687 ^oC, close to the solidus for the case with 3 wt.% H_2O, and at 754 ^oC for 6 wt.% H_2O, nearly 80 ^oC above the solidus. The tonalite crystallizes Pl+Opx at high temperature and at ~800 °C, Opx reacts to Bt. Kfs appears relatively late in the history and H_2O becomes saturated a few degrees above the solidus (T_{sol}= 650 ^oC). The evolution of the melt fraction for all calculations is depicted in Fig. 14b.

The Zr content in the melt increases with crystallization until the melt reaches zircon saturation (Fig. 14c). After this point the melt follows the zircon saturation curve controlled primarily by temperature and secondarily by melt composition, expressed by its M-value that evolves as

crystallization proceeds (Fig. 14d). The temperature of zircon saturation for the diorite with 73 ppm Zr in the melt at the start is 714 or 711 °C using Boehnke et al.'s (2013) calibration, and is only weakly sensitive to the H_2O content, corresponding to melt fractions of 23 to 26 %, respectively. The saturation temperature is ~ 30 - 40 °C higher when using the calibration of Watson and Harrison (1983) corresponding to melt fractions of 26 to 35 wt.%. For the case with 6 wt.% H_2O, zircon saturation is reached at temperatures lower than H_2O saturation. The tonalite initially with 140 ppm Zr and 2 wt.% H_2O reaches zircon saturation at 805 °C and 41% melt (Boehnke *et al.*, 2013), while H_2O becomes saturated a few degrees before the solidus at 650 °C. Thus, zircon saturation temperature of the tonalite is ~ 150 °C above the solidus and 100 °C higher than that of the diorite due to its lower M-values and higher Zr content (140 ppm vs 73 ppm).

For the diorite models, crystallization leads to a gradual decrease in the M value of the melt fraction from close to 2.2 at the liquidus, to a minimum of 1.4 at the solidus (Fig. 14d). The tonalite is different. M values vary only weakly, first decreasing from M=1.45 at the liquidus (not shown) to 1.32 at the start of crystallization of quartz and biotite at which point M increases gently reaching 1.40 at the solidus, similar to the residual melt in the diorite close to its solidus.

The $a(SiO_2)$ and $a(TiO_2)$ in Fig. 14e were used to calculate the expected value of Ti-in-zircon. Despite considerable variation in activities during crystallization, the calculated Ti-in-zircon curves are similar to those calculated using fixed value of $a(SiO_2)$ =1 and $a(TiO_2)$ =0.7 (compare continuous and dashed lines in Fig. 14f). Thus, these values are a good approximation of the behaviour of the metaluminous magmas (see discussion in Schiller & Finger, 2019).

Modelling results indicate that prior to zircon saturation in the dioritic magma, most Zr is hosted in the melt with some going initially into hornblende and biotite as magma cools. At zircon saturation, nearly half the Zr is hosted by these other minerals (Fig. 14g) but as the proportion of zircon increases, these non-zircon minerals record a decrease in the total Zr content that they host. At the solidus, a little over 20 ppm is hosted by non-zircon minerals, and the remaining ~50 ppm is hosted by zircon, corresponding to a (modal) proportion of just under 0.01 % zircon. During tonalite crystallization, few minerals take in Zr, so nearly all of the ~140 ppm is hosted in zircon, corresponding to about 0.03 modal % in the rock.

The decrease in Zr content hosted by non-zircon minerals is a result of the modeling calculations considering the whole-rock chemical composition and distributing the available elements according to the mineral proportions stable at the new temperature. This means that minerals and melt are in equilibrium at all times during cooling. After zircon becomes saturated, the Zr content in the melt decreases as temperature decreases so that the amount of Zr that goes into the non-zircon minerals decreases according to the partition coefficient, kept constant. In a real system, complete equilibrium at all times during cooling may not occur. In this case, some Zr may be trapped in early-formed minerals, in disequilibrium with the cooling melt. The net effect would be slightly less zircon being formed than in the calculations presented.

DISCUSSION

Ages and source of xenocrysts

Field evidence in Fig. 2 indicates that tonalite remelted at the contact with the diorite and back-veined the dykes, causing hybridization that is recorded by felsic dykelets and irregular diffuse leucocratic patches in the diorite. Melting of the tonalite is inferred to be at relatively low temperatures in the presence of aqueous fluids because of the leucocratic nature of the tonalites

446 with little biotite available and no anhydrous peritectic phase such as garnet or orthopyroxene
447 associated with anatexis.

448 The 46-47 Ma age of the diorite dykes places them amongst the syn-collisional, compositionally
449 diverse magmatic flare-up recorded in the southern Lhasa terrane centred around ~50±5 Ma
450 (Zhu *et al.*, 2019). These rocks typically have a wide range of $\varepsilon_{Hf(t)}$ varying between -6 and +15
451 (Fig. 4 in Zhu *et al.*, 2022). The tonalite age of 77-79 Ma with $\varepsilon_{Hf(t)} = +9 \pm 1$ makes it part of
452 the pre-collisional magmatism that had $\varepsilon_{Hf(t)}$ values between +4 and +15.

453 Two out of three diorite samples have older zircon xenocrysts (sample 18DB01-4 and 18DB01-
454 2) that comprise ≤7% of the grains imaged for each diorite sample. These xenocrysts are likely
455 derived from the tonalite host rock as they have the same distinctive euhedral prismatic shape
456 and internal CL zonation (Fig. 6), similar $\varepsilon_{Hf(t)}$ values (Fig. 13), the same range of U-Pb dates
457 from ~80 Ma to 69 Ma (Fig. 11) and similar trace element composition (Fig. 7).

458 **Anomalous zircon composition**

459 Figures 8 and 9 indicate that the diorite zircons have anomalous trace element composition.
460 They have very high trace elements contents, such as U-Th-HREE-Y-Ti, and low values of
461 LREE index (LREE-I, Bell *et al.*, 2016). The elements U, Th and Y define positive trends with
462 Ti. Given that Ti is expected to decrease in zircon during cooling and melt fractionation, the
463 trends suggest that these elements behave compatibly during crystallization, contrary to
464 expectations (Claiborne *et al.*, 2010). Hf is incompatible in the melt defining a negative trend
465 against Ti, as expected, but unexpectedly it also defines a negative trend against U due to its
466 compatible behaviour. The high contents of trace elements indicate the that self-irradiated,
467 damaged diorite zircons may have been altered as a result of reaction with melts or fluids

(Geisler *et al.*, 2007, Hoskin, 2005, Hoskin & Schaltegger, 2003). For example, the values of Ti in some analyses are above 30 ppm, reaching up to a few hundred ppm, and these are generally accompanied by high concentration of other trace elements (Fig. 8).

Metamict and quenched zircon types 3 and 4 (Fig. 6) tend to have high concentration of trace elements (Ca, Fe, REE, U and Th) in contrast to zircon types 1 and 2 (Fig. 8). Despite these differences, they all yield similar U-Pb dates with no systematic change that could be ascribed to Pb-loss (Figs. 10d and 12). In order to determine the extent of alteration, we investigated the relationships between CL types (Fig. 6) and trace element chemistry for each analytical spot, considering signal counts of each analysis during data acquisition using the ICPMSDataCal software. The main findings are that spots with anomalously high trace element abundances typically have one or more of these features:

a) high Th+U contents (>3000 ppm) commonly but not always located in zones of quenched CL. We note however, that there are quenched areas with low Th+U contents (<1000 ppm) indicating that quenching may be related to other factors;
b) anomalous values of LREE, expressed by low values of LREE-I (Fig. 8a,b);
c) anomalous signal plateaus of Fe in CL quenched areas, commonly accompanied by other anomalous signal plateaus for Ca, Ti, LREE, Th and Y (Fig. 15), probably a result of inclusions or domains affected by self-irradiation damage and reaction between zircon and fluid or melt (Geisler *et al.*, 2007);
d) located in zircon sectors characterized by CL types 3 and 4.

We found that taking any of these indicators separately is an insufficient predictor of the spot having a number of chemical anomalies. The strongest predictor of zircons having several such anomalies is having anomalous peaks or plateaus in the count curves, in particular for Fe and Ca. Therefore, we used anomalous peaks or plateaus of Fe and Ca as key indicators of

metamictization and re-equilibration (Geisler *et al.*, 2007) and exclude these analyses from consideration in Ti-in-zircon thermometry. While in most cases, analyses with anomalies of Fe and Ca generally have at least one other feature in the list above, there is a very small number of analyses that have no other indicator of alteration. These were also removed. We have checked the remainder of the data for Ti count anomalies, and found only four analyses with minor Ti anomalous peaks or plateaus. These lacked Fe or Ca anomaly and were therefore evaluated with the rest of the results in the next section.

Uranium, Th and HREE normally behave incompatibly during crystallization and are expected to define a negative trend when plotted against Ti contents (Claiborne *et al.*, 2010). However, these elements in diorite zircons behave compatibly defining a positive trend instead (Fig. 9). In order to further evaluate this behaviour, we have compared the observed data with modelled zircon composition. For both tonalite and diorite, zircon composition is scattered, and modelled composition evolution reproduces them poorly (Fig. 16). The analytical results define a positively correlated array, at high angle to the negative trend of the model calculations or the trend defined by the zircons of Claiborne et al. (2010) (grey field in Fig. 16). This means that the processes controlling zircon trace element intake in the diorite is unaccounted for by our calculations and used assumptions.

Ti-in-zircon thermometry

In this section, only zircons that passed the culling described above, deemed as potentially unaltered, were considered. As we have seen in section 8, converting Ti contents to temperatures requires assumptions regarding TiO_2 and SiO_2 activities. Figure 14f compares two results, one using "conventional" estimates of $a(SIO_2) = 1$ and $a(TiO_2) = 0.7$, and the other using the calculated activities at each point during crystallization (Fig. 14e). The difference between the two is small.

Zircons from tonalites

Analyses of 122 spots from the three tonalite samples and xenocrysts from the diorite, yielded a range in Ti contents from 1.2 to 9.2 ppm (1.2 to 8.5 ppm for the xenocrysts), with a very similar mean (3.3 ppm for the tonalites, 4.0 ppm for the xenocrysts). These values yield temperatures (using ideal activities) from 577 to 786 ^{o}C. Uncertainties for Ti values between 1-2 ppm are between 20-30%, decreasing to below 10% for values >5 ppm, with a detection limit of ~0.5 ppm. While the low-T end of the range likely reflects sub-solidus resetting, the high-T end is lower than but comparable to the zircon saturation temperatures estimated at between 800 and 820 °C (depending on the model used, Fig. 14c).

Zircons from diorites

The Ti-in-zircon values of diorite autocrysts are less well-behaved. Zircons from sample18DB01-4 have Ti contents between 1.4 and 17.7 ppm, which translates to temperatures between 613 and 895 ˚C (using a(SiO_2) = 1, a(TiO_2) = 0.7), or 614 and 842 ˚C (using activities from our model). Since our models also predict the onset of zircon crystallization at low temperatures (710 - 750 ˚C depending on the model chosen, Fig. 14c), this is a significant mismatch, and these “hot” zircons cannot be simply related to zircon saturation temperature estimates.

Similarly, for sample 17DB01-2, Ti ranges between 1.3 and 16.3 ppm (equivalent to a maximum T of 832 ˚C), with a mean of 7.9 ppm. Sample 18DB01-2 (with higher Zr =102 ppm and hence a higher value of the zircon saturation temperature) has Ti contents between 1.5 and

23.3 ppm (equivalent to a maximum T of 915 ˚C), and a mean of 7.1 ppm. Thus, in all cases the maximum Ti-in-zircon temperatures are more than 100 ºC above the estimated zircon saturation temperature, when the diorite still had ~40-55% melt fraction depending on the H_2O content. In all cases, the calculated temperatures for the lowest Ti grains are up to 50 ˚C below the solidus. As our model relies on zircon saturation in melt, we cannot model subsolidus resetting of Ti composition (discussed in Fu *et al.*, 2008).

Modelling zircon crystallization

While the tonalite zircons yield Ti-in-zircon temperatures that cover the expected range derived from the calculations, the diorite zircons do not. For these, the maximum Ti-in-zircon temperatures surpass substantially the modelled zircon saturation temperature in common with findings elsewhere (Barnes *et al.*, 2019, Claiborne *et al.*, 2006, Harrison *et al.*, 2007).

There are two ways of calculating the zircon saturation temperatures. One approach uses the whole-rock composition as an estimate of the magma composition. It assumes that zircon would crystallize from a liquid whose composition equates that of the rock, for which a high M value results in unrealistically high Zr solubility and low saturation temperatures (see Harrison *et al.*, 2007). In this case, diorite sample 18DB01-4, with M=2.4, would yield a saturation temperature of 575 ˚C, which should preclude it from crystallizing zircon. This mismatch with reality is

because the approach does not include the evolution of the residual melt with crystallization, which would cause the Zr content to increase and the melt composition to evolve to lower M values, with lower Zr solubility.

The second approach, the one taken here, considers the evolving composition of the melt during crystallization and determines when zircon crystallizes from this residual liquid, whose composition departs from the bulk composition, becoming enriched in Zr and increasingly more felsic (lower M) (Harrison *et al.*, 2007, Lee & Bachmann, 2014). This approach leads to higher and more realistic zircon saturation temperatures than the first approach (Harrison *et al.*, 2007). Here, using this approach and including Zr uptake by other minerals such as Hbl, Bt and Pl, we found zircon saturation occurs just above 700 °C for the diorite models, some 100 °C lower than the maximum values derived from Ti-in-zircon, as seen in the previous subsection. This discrepancy implies that some other processes must be at play.

Significance of high-Ti zircons

A population of zircons from the diorites show Ti contents > 7 ppm, corresponding to > ~730 ^{o}C, higher than the zircon saturation temperature derived from our models. These same diorite zircons have high contents of U, Th, HREE that define apparently compatible trends (Figs. 9 and 16). Several explanations, not necessarily mutually exclusive, could account for these observations:

a) High-T zircons are xenocrysts or antecrysts. This is unlikely because the high-T zircons have the same internal texture, $\varepsilon_{Hf(t)}$ and U-Pb ages as low-T grains.

b) Presence of inclusions or "non-formula" impurities in zircons. The diorite zircons do have inclusions and cavities and are also partly metamictic with quenched CL images. The high-Ti values, coupled with high Th and REE values, could be due to inclusions of Ti-rich phases, such as titanite or allanite, where the trends with Ti would represent mixing lines. We have excluded analyses with anomalous peaks or plateaus of trace elements in the count curves (section 9.2), and modelling results show that inclusions of titanite would cause a much more rapid increase in Ti contents compared to Nd (Fig. 16a). However, it is possible that metamictization and reaction with fluids and subsequent recrystallization (Geisler *et al.*, 2007) gave rise to micrometer-scale inclusions of assorted Ti-U-Th-REE rich minerals in the zircon matrix. Alternatively, self-irradiation damage gave rise to pore space that hosts "non-formula" impurities (Geisler *et al.*, 2007). At present, either alternative is valid and we conclude that despite exclusion of anomalous analyses, the Ti contents of the remaining zircons may also have been affected, explaining the high-Ti contents and positive trend between Ti and U-Th-Yb (Fig. 9). If this is the case, the Ti-in-zircon values of the diorite zircons do not reflect temperature of crystallization (Fu *et al.*, 2008).

c) Loss of Zr during diorite crystallization (Barnes *et al.*, 2019). In this case, the original melt had higher Zr content than the bulk rock has now, because some of the high-Zr melt was extracted leaving behind a poorer cumulate. If the diorite melt had initially higher Zr than the final rock, it would have reached zircon saturation at higher temperatures than the ones

592 calculated in Fig. 14. The interstitial melt of a crystallizing dioritic magma becomes increasingly
593 enriched in Zr until zircon saturation, at which point the melt starts to lose Zr due to zircon
594 precipitation (Barnes *et al.*, 2019, Harrison *et al.*, 2007, Lee & Bachmann, 2014). If part of this
595 Zr-rich interstitial melt is extracted, the remaining mush or magma will be impoverished in Zr,
596 while retaining some of the early-formed high-T zircons. Any remaining interstitial melt
597 continues to crystallize zircon as the magma continues to cool. Thus, despite relatively low final
598 Zr content, this rock will have early-formed hot zircons that mark the true, high-saturation
599 temperature of the original magma (see Barnes *et al.*, 2019). This alternative is problematic for
600 the Dabu rocks because to reach zircon saturation at ~830-840 ^{o}C (the upper temperatures
601 obtained by Ti-in-zircon thermometry for our samples), the dioritic melt would need to have had
602 an unrealistically high Zr content of >300 ppm. Therefore, while this process may have
603 contributed to decreasing the Zr content of the evolving magma, and therefore the inferred
604 zircon saturation temperature, it is unlikely to be the main reason for the high Ti-values of some
605 zircons.

606 On balance, it is likely that the trace element trends in Fig. 9 and the Ti-content of diorite
607 zircons reflect zircon alteration during metamictization, where high contents of trace elements
608 are hosted either in pore space in amorphous remnants inside the grains or in inclusions resulting
609 from recrystallization of the amorphous, damaged zones (Geisler *et al.*, 2007). Consequently, the
610 Ti content in the diorite zircons is not a reliable measure of crystallization temperature.

611 **Preservation of euhedral zircon xenocrysts**

612 Euhedral zircon xenocrysts from the tonalite preserved in two diorite samples (18DB01-4 and
613 18BD01-2) show negligible dissolution. This is inferred from the similarity between CL images
614 of xenocrysts and tonalite zircons: they are euhedral with well-developed oscillatory zoning,

615 lacking obvious truncation of the oscillatory zoning in the outer part of the zircons. It is possible
616 that a thin rim may have been dissolved or grown during final crystallization of the diorite, but
617 they have not been recognized. In this section, we explore how these euhedral xenocrysts may
618 have been preserved during the melting of the tonalite and mixing with the diorite, two steps
619 where they could have been resorbed.

620 We envisage three possible processes that would prevent significant zircon resorption during
621 melting of tonalite: small melt fraction during anatexis, zircon grains protected as inclusions in
622 biotite, or rapid melting and transfer to the diorite with little time for resorption. All alternatives
623 remain open. Once transferred to the dioritic magma, zircon xenocrysts would be partly or
624 completely resorbed if the diorite was undersaturated. The fact that they are well preserved, and
625 that corroded oval zircons or zircon cores have not been found, can be interpreted in several
626 ways (see discussion in Barnes *et al.*, 2019, Miller *et al.*, 2007):

627 1. A zircon-undersaturated diorite magma crystallized rapidly after receiving the
628 xenocrysts preventing their dissolution. While we cannot entirely dismiss this possibility,
629 we note that: the diorite is fine-grained but not aphanitic or glassy, and lacks chilled
630 margins against the host rock; granitic magma mixed with the mafic magma, suggesting
631 that there was enough time for interaction and widespread transfer of zircons; and the
632 diorite magma produced zircon autocrysts up to 0.4 mm long with rational crystal faces
633 after it became zircon-saturated at low T. Combined, these features suggest that if the
634 diorite magma was undersaturated, there would have been enough time for the xenocrysts

635 to be partly consumed before the magma becoming saturated and crystallizing its own
636 zircon autocrysts.
637 2. Zircons could have been transferred as inclusions in residual biotite from the
638 tonalite in the granitic melt (e.g. Clemens, 2003). However, we found no pleochroic haloes
639 in biotite in the diorite (Fig. 5) and biotite would have been unstable in the dioritic magma
640 at T>810 ^{o}C (for the diorite with 3 wt.% H_2O), or > 750 ^{o}C (for 6 wt.% H_2O) (Fig. 14a). In
641 this case, biotite would have reacted out and zircons exposed to the melt. Thus, armouring
642 would have been possible only if biotite transfer occurred at relatively low temperatures,
643 for which the diorite would have been a mush with <40% melt (Fig. 14b). While we cannot
644 discount this possibility, we do not find support for it.
645 3. If we reject the results from Ti-in-zircon thermometry considering that it could
646 have been affected by alteration, and consider instead that the zircon saturation
647 temperatures in Fig. 14 approach the true value, then the Dabu diorite would have reached
648 zircon saturation between 700 to 750 ˚C. At these conditions, the diorite would have been a
649 crystalline mush with only between ~23% and ~ 26% interstitial melt. In this case, the
650 extensive magma mixing observed within the dyke would require either pervasive flow of
651 the granitic melt through the mush, or liquefaction of the mushy diorite possibly caused by
652 the addition of melt derived from tonalite anatexis.

653 Bringing together the field evidence, the data and the considerations regarding zircon saturation
654 temperature (point 3 above), we propose the following sequence of events (Fig. 17): the dykes
655 were paths of H_2O-rich dioritic magmas that released heat and H_2O to the surroundings as the
656 magma became a crystalline mush. This triggered water-fluxed melting of the tonalite that
657 released zircon grains into an anatectic granitic melt. This melt back-veined and mixed with the
658 diorite transferring tonalite zircons to the dioritic magma, where they remained stable (or nearly
659 so), explaining their well-preserved euhedral shapes and internal zonation. Preservation of the
660 xenocrysts could have been either through armouring, for which we find no evidence, or through
661 transfer to a zircon-saturated dioritic medium. Even assuming large uncertainties in the Zr
662 content of the original melt caused by melt gain or loss during crystallization, zircon saturation
663 temperature would have been reached when the diorite was a crystalline mush. Therefore,
664 zircons were likely transferred to a dioritic mush through mixing. How did this occur? Mushes
665 are permeable solids, open to invasion of foreign magmas (Xu *et al.*, 2021) and prone to
666 liquefaction (Weinberg *et al.*, 2021). The granitic magma may have exploited permeable porous
667 pathways through the mush leading to hybridization and influx of zircon xenocrysts into the
668 matrix of the mush. This same ingress of granitic magma may have caused liquefaction and
669 remobilization of the mush favouring further mixing. Both these processes could give rise to the
670 variety of mingling features in Fig. 2c,d, including the irregular, infolded felsic dykes commonly

671 with gradational contacts with the mafic rocks, and blocks of better-preserved diorites in a
672 hybrid rock. A detailed textural investigation of the different steps in the hybridization process
673 in Fig. 2, with particular focus on disequilibrium textures and mineral zonation, might better
674 reveal the nature of these processes. Determining the existence of narrow, younger rims around
675 the xenocrysts, and with that better visualizing the shape of the xenocrystic grains, might help
676 support this interpretation.

677 CONCLUSIONS

678 The intrusion of the Dabu diorite dyke swarm at 46-47 Ma is part of the waning stages of the
679 syn-collisional magmatic flare-up of the Gangdese belt. The outcrops in Dabu record how these
680 dykes assimilated the 77-79 Ma host tonalite by remelting it and then mixing with the newly
681 formed melt. The tonalite melted at low temperatures fluxed by water likely released with heat
682 by the dykes. The transfer of tonalite zircons to and their preservation in the diorite dykes
683 provides an opportunity to explore the conditions of magma hybridization and the limits of
684 zircon-based thermometry. Given the importance of dykes as feeders of large magma bodies,
685 and the high H_2O contents and temperatures prevalent in active magmatic arcs, the Dabu dykes
686 could represent a common process of hybridization in magmatic arcs, akin to the mixing-
687 assimilation-storage-homogenization, MASH, hypothesis (Hildreth & Moorbath, 1988).

688 We found that the Ti-in-zircon temperature estimations for the tonalite matched well the range
689 defined by zircon saturation temperature predicted by modelling of crystallization/melting of the
690 tonalite. However, the same is not true for dioritic zircon autocrysts. These yield Ti-in-zircon
691 temperatures ranging from below the solidus to >100 ^{o}C above the zircon saturation
692 temperatures. This discrepancy could be related either to loss of Zr during diorite crystallization
693 (Barnes *et al.*, 2019) or to alteration and recrystallization of the zircons (Geisler *et al.*, 2007),
694 indicated by quenched CL and high Ti contents, as well as U, Th, Ca, Fe, Y, REE (or low

LREE-I; Fig. 8). Either way, the results show how even through exclusion of zircons with obvious indicators of alteration, they may still have unreliable Ti values, defining unexpected trends against other trace elements (Fig. 16).

Interestingly, but not surprisingly, the tonalite with ~140 ppm Zr has a zircon saturation temperature close to 100 ^{o}C higher than the diorite with half the amount of Zr, indicating yet again that this temperature does not constrain the temperature of magma formation. However, for the Dabu rocks, zircon saturation temperature is useful in constraining the crystallinity of the diorite intrusion at the time of hybridization. This is because a striking feature of these rocks is that the zircon xenocrysts from the tonalite record little resorption, requiring that the xenocrysts be either armoured in biotite during mixing, or that they be exposed to a low-temperature granitic melt first, and then transferred to a zircon-saturated diorite. The absence of pleochroic haloes in biotite in the diorite and the instability of biotite in hot dioritic magmas suggest that armouring is unlikely. The low-temperature zircon saturation of ~715 ^{o}C ensures that the diorite would have been a high crystallinity mush with only ~25 wt.% melt at the time of zircon saturation. Even if the Zr content were doubled or trebled, zircon saturation in the diorite would still have occurred in a mush. Thus, we conclude that hybridization occurred in a zircon saturated mush through melt leak-off from invading granitic veins into the pore-space of the mush, possibly accompanied by liquefaction (Weinberg *et al.*, 2021). We argue that pore-invasion combined with the liquefaction of mushes is a powerful mixing process. Because of its stealthy nature, this process of magma mixing in dykes could be important during the build-up of arcs feeding large magma reservoirs with hybrid magmas.

The Dabu dyke swarm represents one end-member of zircon behavior during hybridization where xenocrysts are preserved with minimal resorption. This behavior helped us constrain the nature and conditions of zircon transfer and magma hybridization. However, the general rarity of zircon xenocrysts in magmatic rocks of the Gangdese arc (e.g. Zhu *et al.*, 2015) suggests that

complete zircon resorption could be common, leaving few tools to recognize the remelting of older arc rocks and magma hybridization. This is especially true when the arc has a narrow range of radioactive isotope ratios. Thus, assimilation through remelting of older arc rocks, followed by hybridization and homogenization (MASH, Hildreth & Moorbath, 1988) could be widespread with little evidence preserved. In such cases, disentangling magma evolution and the nature of magma hybridization require detailed field documentation accompanied by investigation of fine chemical and isotopic zonation of a range of accessories and rock-forming minerals (e.g. Barnes *et al.*, 2021, Chambers *et al.*, 2020).

FUNDING

This research was financially co-supported by the National Natural Science Foundation of China (42121002 and 91755207), the Second Tibetan Plateau Scientific Expedition and Research Program (STEP) (2019QZKK0702), and the 111 project (B18048).

SUPPLEMENTARY DATA

Supplementary data are available at Journal of Petrology online.

Data Availability

The data underlying this article are available in the article and in its online supplementary material.

ACKNOWLEDGEMENTS

We thank Vali Memeti, Calvin Miller and Bill Collins for careful and insightful reviews that much improved the original manuscript.

REFERENCES

Andersen, T. (2002). Correction of common lead in U–Pb analyses that do not report 204Pb. *Chemical Geology* **192**, 59-79.

743 Barnes, C. G., Werts, K., Memeti, V. & Ardill, K. (2019). Most Granitoid Rocks are Cumulates:
744 Deductions from Hornblende Compositions and Zircon Saturation. *Journal of Petrology* **60**,
745 2227-2240.

746 Barnes, C. G., Werts, K., Memeti, V., Paterson, S. R. & Bremer, R. (2021). A tale of five enclaves:
747 Mineral perspectives on origins of mafic enclaves in the Tuolumne Intrusive Complex.
748 *Geosphere* **17**, 352-374.

749 Bell, E. A., Boehnke, P. & Harrison, T. M. (2016). Recovering the primary geochemistry of Jack
750 Hills zircons through quantitative estimates of chemical alteration. *Geochimica et*
751 *Cosmochimica Acta* **191**, 187-202.

752 Blichert-Toft, J. (2008). The Hf isotopic composition of zircon reference material 91500.
753 *Chemical Geology* **253**, 252-257.

754 Boehnke, P., Watson, E. B., Trail, D., Harrison, T. M. & Schmitt, A. K. (2013). Zircon saturation
755 re-revisited. *Chemical Geology* **351**, 324-334.

756 Bouvier, A., Vervoort, J. D. & Patchett, P. J. (2008). The Lu–Hf and Sm–Nd isotopic composition
757 of CHUR: Constraints from unequilibrated chondrites and implications for the bulk composition
758 of terrestrial planets. *Earth and Planetary Science Letters* **273**, 48-57.

759 Bruand, E., Fowler, M., Storey, C., Laurent, O., Antoine, C., Guitreau, M., Heilimo, E. & Nebel,
760 O. (2020). Accessory mineral constraints on crustal evolution: elemental fingerprints for magma
761 discrimination. *Geochemical Perspectives Letters* **13**, 7-12.

762 Chambers, M., Memeti, V., Eddy, M. P. & Schoene, B. (2020). Half a million years of magmatic
763 history recorded in a K-feldspar megacryst of the Tuolumne Intrusive Complex, California,
764 USA. *Geology* **48**, 400-404.

765 Chu, M.-F., Chung, S.-L., O'Reilly, S. Y., Pearson, N. J., Wu, F.-Y., Li, X.-H., Liu, D., Ji, J., Chu,
766 C.-H. & Lee, H.-Y. (2011). India's hidden inputs to Tibetan orogeny revealed by Hf isotopes of
767 Transhimalayan zircons and host rocks. *Earth and Planetary Science Letters* **307**, 479-486.

768 Claiborne, L. L., Miller, C. F., Gualda, G. A. R., Carley, T. L., Covey, A. K., Wooden, J. L. &
769 Fleming, M. A. (2018). Zircon as Magma Monitor. *Microstructural Geochronology*, 1-33.

770 Claiborne, L. L., Miller, C. F., Walker, B. A., Wooden, J. L., Mazdab, F. K. & Bea, F. (2006).
771 Tracking magmatic processes through Zr/Hf ratios in rocks and Hf and Ti zoning in zircons: An
772 example from the Spirit Mountain batholith, Nevada. *Mineralogical Magazine* **70**, 517-543.

773 Claiborne, L. L., Miller, C. F. & Wooden, J. L. (2010). Trace element composition of igneous
774 zircon: a thermal and compositional record of the accumulation and evolution of a large silicic
775 batholith, Spirit Mountain, Nevada. *Contributions to Mineralogy and Petrology* **160**, 511-531.

776 Clemens, J. D. (2003). S-type granitic magmas—petrogenetic issues, models and evidence. *Earth-*
777 *Science Reviews* **61**, 1-18.

778 Collins, W. J., Huang, H.-Q. & Jiang, X. (2016). Water-fluxed crustal melting produces
779 Cordilleran batholiths. *Geology* **44**, 143-146.

780 Collins, W. J., Murphy, J. B., Johnson, T. E. & Huang, H.-Q. (2020). Critical role of water in the
781 formation of continental crust. *Nature Geoscience* **13**, 331-338.

782 Connolly, J. A. D. (2005). Computation of phase equilibria by linear programming: A tool for
783 geodynamic modeling and its application to subduction zone decarbonation. *Earth and*
784 *Planetary Science Letters* **236**, 524-541.

785 Connolly, J. A. D. & Petrini, K. (2002). An automated strategy for calculation of phase diagram
786 sections and retrieval of rock properties as a function of physical conditions. *Journal of*
787 *Metamorphic Geology* **20**, 697-708.

788 Ferry, J. M. & Watson, E. B. (2007). New thermodynamic models and revised calibrations for the
789 Ti-in-zircon and Zr-in-rutile thermometers. *Contributions to Mineralogy and Petrology* **154**,
790 429-437.
791 Frost, B. R., Barnes, C. G., Collins, W. J., Arculus, R. J., Ellis, D. J. & Frost, C. D. (2001). A
792 geochemical classification for granitic rocks. *Journal of Petrology* **42**, 2033-2048.
793 Fu, B., Page, F. Z., Cavosie, A. J., Fournelle, J., Kita, N. T., Lackey, J. S., Wilde, S. A. & Valley,
794 J. W. (2008). Ti-in-zircon thermometry: applications and limitations. *Contributions to*
795 *Mineralogy and Petrology* **156**, 197-215.
796 Gagnevin, D., Daly, J. S. & Kronz, A. (2010). Zircon texture and chemical composition as a guide
797 to magmatic processes and mixing in a granitic environment and coeval volcanic system.
798 *Contributions to Mineralogy and Petrology* **159**, 579-596.
799 Geisler, T., Schaltegger, U. & Tomaschek, F. (2007). Re-equilibration of zircon in aqueous fluids
800 and melts. *Elements* **3**, 43-50.
801 Griffin, W. L., Pearson, N. J., Belousova, E., Jackson, S. E., van Achterbergh, E., O'Reilly, S. Y.
802 & Shee, S. R. (2000). The Hf isotope composition of cratonic mantle: LAM-MC-ICPMS
803 analysis of zircon megacrysts in kimberlites. *Geochimica et Cosmochimica Acta* **64**, 133-147.
804 Griffin, W. L., Wang, X., Jackson, S. E., Pearson, N. J., O'Reilly, S. Y., Xu, X. & Zhou, X. (2002).
805 Zircon chemistry and magma mixing, SE China: In-situ analysis of Hf isotopes, Tonglu and
806 Pingtan igneous complexes. *Lithos* **61**, 237-269.
807 Harrison, T. M., Watson, E. B. & Aikman, A. B. (2007). Temperature spectra of zircon
808 crystallization in plutonic rocks. *Geology* **35**, 635-638.
809 Hildreth, W. & Moorbath, S. (1988). Crustal contributions to arc magmatism in the Andes of
810 Central Chile. *Contributions to Mineralogy and Petrology* **98**, 455-489.
811 Holland, T. J. B., Green, E. C. R. & Powell, R. (2018). Melting of Peridotites through to Granites:
812 A Simple Thermodynamic Model in the System KNCFMASHTOCr. *Journal of Petrology* **59**,
813 881-900.
814 Hoskin, P. W. O. (2005). Trace-element composition of hydrothermal zircon and the alteration of
815 Hadean zircon from the Jack Hills, Australia. *Geochimica et Cosmochimica Acta* **69**, 637-648.
816 Hoskin, P. W. O. & Schaltegger, U. (2003). The Composition of Zircon and Igneous and
817 Metamorphic Petrogenesis. *Reviews in Mineralogy and Geochemistry* **53**, 27-62.
818 Jagoutz, O. & Klein, B. (2018). On the importance of crystallization-differentiation for the
819 generation of SiO₂-rich melts and the compositional build-up of arc (and
820 continental) crust. *American Journal of Science* **318**, 29-63.
821 Ji, W.-Q., Wu, F.-Y., Chung, S.-L., Li, J.-X. & Liu, C.-Z. (2009). Zircon U–Pb geochronology and
822 Hf isotopic constraints on petrogenesis of the Gangdese batholith, southern Tibet. *Chemical*
823 *Geology* **262**, 229-245.
824 Kapp, P. & DeCelles, P. G. (2019). Mesozoic–Cenozoic geological evolution of the Himalayan-
825 Tibetan orogen and working tectonic hypotheses. *American Journal of Science* **319**, 159-254.
826 Kemp, A. I. S., Hawkesworth, C. J., Foster, G. L., Paterson, B. A., Woodhead, J. D., Hergt, J. M.,
827 Gray, C. M. & Whitehouse, M. J. (2007). Magmatic and Crustal Differentiation History of
828 Granitic Rocks from Hf-O Isotopes in Zircon. *Science* **315**, 980-983.
829 Kirkland, C. L., Yakymchuk, C., Olierook, H. K. H., Hartnady, M. I. H., Gardiner, N. J., Moyen,
830 J.-F., Hugh Smithies, R., Szilas, K. & Johnson, T. E. (2021). Theoretical versus empirical
831 secular change in zircon composition. *Earth and Planetary Science Letters* **554**, 116660.
832 Laurent, O. (2012). Les changements géodynamiques à la transition Archéen-Protérozoïque : étude
833 des granitoïdes de la marge Nord du craton du Kaapvaal (Afrique du Sud). PhD thesis
834 Université Blaise Pascal, Clermont-Ferrand.

Lee, C.-T. A. & Bachmann, O. (2014). How important is the role of crystal fractionation in making intermediate magmas? Insights from Zr and P systematics. *Earth and Planetary Science Letters* **393**, 266-274.

Liu, Y., Hu, Z., Gao, S., Günther, D., Xu, J., Gao, C. & Chen, H. (2008). In situ analysis of major and trace elements of anhydrous minerals by LA-ICP-MS without applying an internal standard. *Chemical Geology* **257**, 34-43.

Liu, Y., Hu, Z., Zong, K., Gao, C., Gao, S., Xu, J. & Chen, H. (2010). Reappraisement and refinement of zircon U-Pb isotope and trace element analyses by LA-ICP-MS. *Chinese Science Bulletin* **55**, 1535-1546.

Ludwig, K. R. (2003). *User's manual for Isoplot 3.00: a geochronological toolkit for Microsoft Excel*. Berkeley.

Ma, L., Wang, Q., Li, Z.-X., Wyman, D. A., Jiang, Z.-Q., Yang, J.-H., Gou, G.-N. & Guo, H.-F. (2013). Early Late Cretaceous (ca. 93Ma) norites and hornblendites in the Milin area, eastern Gangdese: Lithosphere–asthenosphere interaction during slab roll-back and an insight into early Late Cretaceous (ca. 100–80Ma) magmatic "flare-up" in southern Lhasa (Tibet). *Lithos* **172-173**, 17-30.

Miller, C. F., McDowell, S. M. & Mapes, R. W. (2003). Hot and cold granites? Implications of zircon saturation temperatures and preservation of inheritance. *Geology* **31**, 529-532.

Miller, J. S., Matzel, J. E. P., Miller, C. F., Burgess, S. D. & Miller, R. B. (2007). Zircon growth and recycling during the assembly of large, composite arc plutons. *Journal of Volcanology and Geothermal Research* **167**, 282-299.

Morel, M. L. A., Nebel, O., Nebel-Jacobsen, Y. J., Miller, J. S. & Vroon, P. Z. (2008). Hafnium isotope characterization of the GJ-1 zircon reference material by solution and laser-ablation MC-ICPMS. *Chemical Geology* **255**, 231-235.

Moyen, J.-F., Janoušek, V., Laurent, O., Bachmann, O., Jacob, J.-B., Farina, F., Fiannacca, P. & Villaros, A. (2021). Crustal melting vs. fractionation of basaltic magmas: Part 1, The bipolar disorder of granite petrogenetic models. *Lithos*, 106291.

Müntener, O. & Ulmer, P. (2018). Arc crust formation and differentiation constrained by experimental petrology. *American Journal of Science* **318**, 64-89.

Paton, C., Hellstrom, J., Paul, B., Woodhead, J. & Hergt, J. (2011). Iolite: Freeware for the visualisation and processing of mass spectrometric data. *Journal of Analytical Atomic Spectrometry* **26**, 2508-2518.

Reubi, O. & Blundy, J. (2009). A dearth of intermediate melts at subduction zone volcanoes and the petrogenesis of arc andesites. *Nature* **461**, 1269-1273.

Rubatto, D. & Hermann, J. (2007). Experimental zircon/melt and zircon/garnet trace element partitioning and implications for the geochronology of crustal rocks. *Chemical Geology* **241**, 38-61.

Schiller, D. & Finger, F. (2019). Application of Ti-in-zircon thermometry to granite studies: problems and possible solutions. *Contributions to Mineralogy and Petrology* **174**, 51.

Shand, S. J. (1943). *Eruptive Rocks: Their Genesis, Composition, Classification, and Their Relation to Ore-Deposits with a Chapter on Meteorite*. New York: John Wiley & Sons.

Siégel, C., Bryan, S. E., Allen, C. M. & Gust, D. A. (2018). Use and abuse of zircon-based thermometers: A critical review and a recommended approach to identify antecrystic zircons. *Earth-Science Reviews* **176**, 87-116.

Sláma, J., Košler, J., Condon, D. J., Crowley, J. L., Gerdes, A., Hanchar, J. M., Horstwood, M. S. A., Morris, G. A., Nasdala, L., Norberg, N., Schaltegger, U., Schoene, B., Tubrett, M. N. & Whitehouse, M. J. (2008). Plešovice zircon — A new natural reference material for U–Pb and Hf isotopic microanalysis. *Chemical Geology* **249**, 1-35.

Söderlund, U., Patchett, P. J., Vervoort, J. D. & Isachsen, C. E. (2004). The 176Lu decay constant determined by Lu–Hf and U–Pb isotope systematics of Precambrian mafic intrusions. *Earth and Planetary Science Letters* **219**, 311-324.

Sun, S.-s. & McDonough, W. F. (1989). Chemical and isotopic systematics of oceanic basalts: implications for mantle composition and processes. *Geological Society, London, Special Publications* **42**, 313-345.

Symington, N. J., Weinberg, R. F., Hasalová, P., Wolfram, L. C., Raveggi, M. & Armstrong, R. A. (2014). Multiple intrusions and remelting-remobilization events in a magmatic arc: The St. Peter Suite, South Australia. *Bulletin of the Geological Society of America* **126**, 1200-1218.

Troch, J., Ellis, B. S., Schmitt, A. K., Bouvier, A.-S. & Bachmann, O. (2018). The dark side of zircon: textural, age, oxygen isotopic and trace element evidence of fluid saturation in the subvolcanic reservoir of the Island Park-Mount Jackson Rhyolite, Yellowstone (USA). *Contributions to Mineralogy and Petrology* **173**, 54.

Wang, R., Richards, J. P., Hou, Z.-q., An, F. & Creaser, R. A. (2015). Zircon U–Pb age and Sr–Nd–Hf–O isotope geochemistry of the Paleocene–Eocene igneous rocks in western Gangdese: Evidence for the timing of Neo-Tethyan slab breakoff. *Lithos* **224-225**, 179-194.

Wang, R., Weinberg, R. F., Collins, W. J., Richards, J. P. & Zhu, D.-c. (2018). Origin of postcollisional magmas and formation of porphyry Cu deposits in southern Tibet. *Earth-Science Reviews* **181**, 122-143.

Watson, E. B. & Harrison, T. M. (1983). Zircon saturation revisited: temperature and composition effects in a variety of crustal magma types. *Earth and Planetary Science Letters* **64**, 295-304.

Watson, E. B., Wark, D. A. & Thomas, J. B. (2006). Crystallization thermometers for zircon and rutile. *Contributions to Mineralogy and Petrology* **151**, 413.

Weinberg, R. F. & Dunlap, W. J. (2000a). Growth and deformation of the Ladakh batholith, northwest Himalayas: Implications for timing of continental collision and origin of calc-alkaline batholiths. *Journal of Geology* **108**, 303-320.

Weinberg, R. F. & Dunlap, W. J. (2000b). Growth and Deformation of the Ladakh Batholith, Northwest Himalayas: Implications for Timing of Continental Collision and Origin of Calc-Alkaline Batholiths. *Journal of Geology* **108**, 303-320.

Weinberg, R. F., Vernon, R. & Schmelling, H. (2021). Granitic mushes: their role in magma mixing and assimilation of solids with special focus on enclaves. *Earth-Science Reviews* **220**, 103665.

White, L. T., Ahmad, T., Ireland, T. R., Lister, G. S. & Forster, M. A. (2011). Deconvolving episodic age spectra from zircons of the Ladakh Batholith, northwest Indian Himalaya. *Chemical Geology* **289**, 179-196.

Xu, W., Zhu, D.-C., Wang, Q., Weinberg, R. F., Wang, R., Li, S.-M., Zhang, L.-L. & Zhao, Z.-D. (2021). Cumulate mush hybridization by melt invasion: Evidence from compositionally-diverse amphiboles in ultramafic-mafic arc cumulates within the eastern Gangdese Batholith, southern Tibet. *Journal of Petrology* **61**, ega073.

Yin, A. & Harrison, T. M. (2000). Geologic evolution of the Himalayan-Tibetan orogen. *Annual Review of Earth and Planetary Sciences*, 211-280.

Zhang, L.-L., Zhu, D.-C., Wang, Q., Zhao, Z.-D., Liu, D. & Xie, J.-C. (2019). Late Cretaceous volcanic rocks in the Sangri area, southern Lhasa Terrane, Tibet: Evidence for oceanic ridge subduction. *Lithos* **326-327**, 144-157.

Zhang, Z., Ding, H., Palin, R. M., Dong, X., Tian, Z. & Chen, Y. (2020). The lower crust of the Gangdese magmatic arc, southern Tibet, implication for the growth of continental crust. *Gondwana Research* **77**, 136-146.

930 Zhang, Z., Zhao, G., Santosh, M., Wang, J., Dong, X. & Shen, K. (2010). Late Cretaceous
931 charnockite with adakitic affinities from the Gangdese batholith, southeastern Tibet: Evidence
932 for Neo-Tethyan mid-ocean ridge subduction? *Gondwana Research* **17**, 615-631.
933 Zhu, D.-C., Wang, Q., Chung, S.-L., Cawood, P. A. & Zhao, Z.-D. (2019). Gangdese magmatism
934 in southern Tibet and India–Asia convergence since 120 Ma. *Geological Society, London,*
935 *Special Publications* **483**, 583-604.
936 Zhu, D.-C., Wang, Q., Weinberg, R. F., Cawood, P. A., Chung, S.-L., Zheng, Y.-F., Zhao, Z.,
937 Hou, Z.-Q. & Mo, X.-X. (2022). Interplay between oceanic subduction and continental collision
938 in building continental crust. *Nature Communications* **13**, 7141.
939 Zhu, D.-C., Wang, Q., Zhao, Z.-D., Chung, S.-L., Cawood, P. A., Niu, Y., Liu, S.-A., Wu, F.-Y. &
940 Mo, X.-X. (2015). Magmatic record of India-Asia collision. *Scientific Reports* **5**, 14289.
941 Zhu, D.-C., Zhao, Z.-D., Niu, Y., Mo, X.-X., Chung, S.-L., Hou, Z.-Q., Wang, L.-Q. & Wu, F.-Y.
942 (2011). The Lhasa Terrane: Record of a microcontinent and its histories of drift and growth.
943 *Earth and Planetary Science Letters* **301**, 241-255.
944

945 **Figure Captions**

946 Fig. 1. a) Geological map of the Gangdese Batholith linking to the Ladakh Batholith in the west.
947 Small rectangle in the east shows the location of (b). Inset shows the location of (a). b)
948 Geological map of the area surrounding the village of Dabu and the dykes investigated here.
949 BNSZ refers to the Bangong-Nujiang Suture Zone, SNMZ to the Shiquanhe–Nam Tso Mélange
950 Zone, LMF to Luobadui-Milashan Fault, IYZSZ to the Indus-Yarlung Tsangpo Suture Zone,
951 and MBT refers to the Main Boundary Thrust.

952 Fig. 2. Field relationships. a) Diorite dykes cutting through tonalite close to Dabu village. All
953 samples and photographs are from this location. Small black ellipse on lower left indicates a
954 small van for scale. Rectangle on right-hand side marks the position of (b). b) Tip of dykes with
955 variable width and orientation. Vertical scale is ~3m. (c) irregular boundary between dyke and
956 tonalite with back-veining of a finer granitic rock. d) Irregularities at the contact at cm-scale. e)
957 and f) Heterogeneous diorite with irregular veins with sharp to diffuse margins linked to
958 irregular patches with gradational contact with the diorite. These are interpreted to record the
959 nature of mingling and mixing of between granitic and dioritic magmas.

960 Fig. 3. Major element features of the studied samples (Frost *et al.*, 2001). a) FeO/(FeO+MgO) vs
961 SiO2 showing the boundary between ferroan and magnesian plutonic rocks; b) SiO2–MALI
962 (wt.%) binary diagram (MALI = Modified alkali-lime index, Na_2O+K_2O-CaO) from Frost et al.
963 (2001); (c) ASI vs. A/NK diagram [atomic Al/Ca+Na+K vs. Al/Na+K] (Shand, 1943). Tonalites
964 and diorites are magnesian, calc-alkalic and metaluminous to weakly peraluminous.

965 Fig. 4. MORB-normalized (Sun & McDonough, 1989) trace element patterns for the studied
966 samples.

967 Fig. 5. Photomicrographs of diorite samples. a) Sample 18DB01-2 showing euhedral to
968 subhedral biotite in brown tones and hornblende in green tones. Notice apatite needles in
969 plagioclase dominated areas (transparent) (ppl); b) sample 8DB01-2 showing biotite in an
970 equant matrix of twinned plagioclase. Note labelled epidote inclusion in biotite (xpl); c) sample
971 17DB01-2 (ppl); d) sample 18DB01-4 showing anhedral hornblende and subhedral biotite
972 surrounding aggregates of plagioclase (transparent) (ppl). Apatite and epidote grains are
973 indicated. Note absence of pleochroic haloes in biotite in all photomicrographs.

974 Fig. 6. Zircon CL images. Diorite samples 17DB01-2 (a) and 18DB01-2 (b). Zircons have
975 roughly rectangular shapes with two parallel rational faces and two irregular sides. They are
976 generally dark, but some are grey or bright, with either no zoning, irregular zoning or wide

977 bands. The two samples have contrasting zircon sizes. c) Tonalite sample 18DB01-3 showing
978 representative grains similar to the other two tonalite samples. Zircons are euhedral, bright with
979 well-developed, continuous oscillatory zoning. Some rare grains show a quenched region
980 overprinting the early-formed zoning (left-side of bottom grain). d) Diorite sample 18DB01-4
981 with two distinct zircon morphological groups: a small group of euhedral zircons labelled
982 xenocrysts, similar to those from the tonalite in (c), and a larger group similar to those from the
983 diorites in (a) and (b). The xenocrysts have ages that coincide with those of the tonalite samples.
984 Green, red and black dashed circles indicate position of analytical spot and colour indicates
985 origin of the zircon: diorite, tonalite and xenocryst in diorite, respectively. Numbers indicate U-
986 Pb age obtained. The scale in (a) applies to all images.

987 Fig. 7. a) REE plot normalized to chondrite (Sun & McDonough, 1989). Zircons from the
988 tonalitic host define similar patterns to the xenocrysts in the diorite sample 18DB01-4, both
989 dated at between 70 and 80 Ma (see Fig. 11d). Diorite zircon autocrysts have higher values than
990 the tonalite zircons and show a wide variation in LREE values (six orders of magnitude for La)
991 reflecting alteration effects (e.g. Bell *et al.*, 2016). b) Yb/Dy vs Eu/Eu* showing trace element
992 similarity between the xenocryst zircons in diorite and tonalite autocrysts.

993 Fig. 8. Zircon trace element versus the Light Rare Earth Element Index [LREE-I = (Dy/Nd +
994 Dy/Sm)] (a proxy for zircon alteration Bell *et al.*, 2016) and U content. Diorite zircon analyses
995 are divided into two groups based on CL: types 1-2 clean grey sections of grains and types 3-4
996 regions dominated by metamictization and CL quenching; see Supplementary Data Electronic
997 Appendix 2). There is considerable overlap between the two groups but types 3-4 have
998 systematically lower LREE-1 and higher contents of all trace elements. In (a) and (b) Fe and Ti
999 define negative trends with LREE-1 (in these figures, types 3-4 symbols were placed in front of
1000 types 1-2 for better visualization of the link between zircons deemed altered and LREE-I values.
1001 Types 3-4 zircon analyses concentrate, as expected, in the lower end of LREE-1, indicative of
1002 alteration, but reach values of 100, considerably higher than the cutoff value of 30 for alteration
1003 of Bell et al. (2016). Up to 100, types 3-4 overlap with types 1-2, and these can have very high
1004 contents of Ti. In (c) to (h), Fe, Ca, Th, Y reach values close to 10,000 ppm or 1 wt.%, defining
1005 positive trends with U, which reaches up to 9000 ppm. Titanium also defines a positive trend
1006 with U, with numerous analyses above 30 ppm, some reaching a few 100 ppm. The trend
1007 defined by Hf and Ti in diorite zircons are the opposite to those found for granitic rocks by
1008 Claiborne et al. (2010) shown by the grey fields, and similar to the high-U zircons in Fig. 6 in
1009 Troch et al. (2018). In (c) to (h), types 3-4 zircon symbols were placed behind types 1-2. For

tonalite zircons, the trends are similar to those in Claiborne et al. (2010). Tonalite zircons and xenocrysts in diorite sample 18DB01-4 are not differentiated and overlap in the plots. All plots are log-log scale.

Fig. 9. (a-d) Binary plots of typically incompatible elements versus Ti in zircon. For tonalite samples Hf behaves incompatibly defining negative, but all other elements define a curved shape changing from a positive (compatible) to a negative (incompatible) trend as Ti increases. This is not the case for the diorite sample for which U, Th, and Yb, define only positive or compatible trends with Ti, and only Hf defines a negative (incompatible) trend. The compatible trends are surprising and contrast with the incompatible trends found by Claiborne et al (2010) indicated by grey fields. Ti-values higher than 40 ppm were not plotted as they correspond to unrealistically high T and therefore probably correspond to altered zircons. Grey empty symbols indicate analyses with anomalous peaks or plateaus of Fe and Ca, key indicators of metamictization and zircon re-equilibration (see section 9.2 for discussion). All plots are log-log scale and symbols are as in legend for Fig. 8.

Fig. 10. Concordia diagrams for zircon analyses from diorite samples. a-c) Diorite dyke samples 17DB01-2, 18DB01-2 and 18DB01-4 with ages centred around 46 to 47 Ma. Samples 18DB01-2 and 18DB01-4 also contained 70-80 Ma xenocrysts shown in Fig. 11. d) Comparison between ages of zircon analyses from diorite sample 18DB01-4 as a function of CL type shows no systematic shift between CL types 1-2, and the quenched CL types 3-4 despite the anomalously high values of Th+U and other trace elements in the latter (Fig. 8). All ellipses in (a-c) and bars in (d) mark the 2σ confidence level. A number of analyses have been excluded: 2 of 74 analyses for 17DB01-2 (1 with large error, 1 with fluctuating age signals), 18 out of 75 for 18DB01-2 (16 discordant and 2 outliers), 25 out of 111 for 18DB01-4 (23 discordant, 1 outlier and 1 with large error). A small number of outlier dates were removed from the calculation of the mean age by Isoplot: 2 out of 72 for sample 17DB01-2, 2 out of 57 for sample 18DB01-2, 4 out of 86 for sample 18DB01-4. In (d), analyses in light grey at the high-end of values, have been dates removed from the calculation of the mean age.

Fig. 11. Concordia diagrams for zircon analyses from tonalite samples and xenocrysts in diorite samples. a-c) Tonalite samples 17DB01-1, 18DB01-1, 18DB01-3 showing ages centred between 77 and 79 Ma and lacking older xenocrysts. d) and e) Xenocrysts from diorite dyke sample 18DB01-4 and 18DB01-2. The spread of dates in (d) and (e) imply that the mean ages are not meaningful with MSWD>10. All ellipses mark the 2σ confidence level. A small number of analyses have been excluded from the diagrams: 1 of 18 analyses for sample 17DB01-1 (>10%

discordant), 5 of 68 for 18DB01-1 (2 discordant and 3 outlier), and 3 of 19 for 18DB01-4 (2 with very large errors and 1 outlier). A small number of outliers were removed from the calculation of the mean age by Isoplot: 4 out of 63 for sample 18DB01-1, and 2 out of 18 for sample 18DB01-3.

Fig. 12. $^{206}Pb/^{238}U$ ages for zircons from diorites show no systematic trend with Th+U content. Symbols as in legend for Fig. 8 where empty symbols are types 3-4.

Fig. 13. $\varepsilon_{Hf(t)}$ values for all six samples plotted against zircon U-Pb age. The ~77-79 Ma tonalite zircons have $\varepsilon_{Hf(t)}$ centred around +9 ± 1, whereas the ~46-47 Ma diorite analyses are more spread between +6 and +11. N=344 analyses, with 78 from tonalite zircons and 266 from diorite.

Fig. 14. Model of crystallization for a diorite melt with 73 ppm Zr and a tonalite melt with 144 ppm Zr. H_2O contents for the diorite of 3 wt.% H_2O (left column), and 6 wt.% H_2O (middle column) are shown. Tonalite melt contains 2 wt.% H_2O. Low H_2O content was assumed in order to investigate its remelting by H_2O derived from the diorite intrusion. a) Minerals and melt/H_2O proportions. Diorite solidus T (T_{sol}) is 677 °C, and 650 °C for the tonalite. The two diorite models show nearly 70 °C difference water saturation T. Sphene, spinel and ilmenite form in diorite and tonalite not shown because of low proportions. b) Melt fraction. For all three cases the last ~20% crystallizes within 10 °C of the solidus. c) Zr content in melt. Values increase until the curve intersects the zircon saturation curves calculated using M-values in (d) and calibrations in Boehnke et al. (2013) and Watson and Harrison (1983). Zircon saturation for the diorites is reached at 714 and 711 °C, for 3 and 6 wt.% H_2O, respectively, where ~23% melt (for 3% H_2O) or ~ 26% melt (for 6% H_2O) remain. Tonalite reaches ~ 20% melt at ~650 °C solidus, where ~ 90% of the zircons are stable. d) M-value of residual melt used to determine the zircon saturation curve in (c). M-value for diorites steadily decrease to reach a value of 1.4 close to the solidus. For the tonalite M first decreases from a value of 1.45 at the liquidus (not shown) and then increases to ~1.4 at the solidus, due to stabilization of Bt and Qtz. e) $a(SiO_2)$ and $a(TiO_2)$. f) Ti-in-zircon calculated using curves in (e) (solid lines) or assuming a fixed value of $a(SiO_2)=1$ and $a(TiO_2)=0.7$ (dashed lines; similar to Claiborne et al. (2010)). The differences between the two curves are small. Calculations use Ferry and Watson (2007). g) Zr content in melt, non-zircon phases and zircon as a function of temperature (note different scale in x-axis). Zircons are saturated close to the solidus for diorite. Diorite composition is similar to the basalt modelled by

Lee and Bachmann (2014) (their Fig. 2b), but despite higher Zr in our starting composition, melt never reaches the > 300 ppm Zr in their model, peaking instead at ~ 150 ppm, due to significant intake of Zr in non-zircon minerals excluded in their model.

Fig. 15. Comparison of signal outputs from zircon analyses for sample 18DB01-4: a) spot 1-04 in a type 1 zircon, and b) spot 2-41 in a type 2 zircon. Data from (b) was excluded from consideration because of anomalous plateaus of Fe, Ca, Ti, and a sudden drop in Th, U counts.

Fig. 16. Zircon chemistry modelling. a) Modelled zircon Th vs Ti composition for the diorite and tonalite (thick black lines) compared with data for zircons from diorite dykes, xenocrystic zircons in diorite and tonalite host rock zircons; b) same for Nd vs Ti. Analysed zircon grains are colour coded according to "reliability": if the zircon analysis has anomalous Fe or Ca signal it is deemed unreliable, if it has anomalous peaks or plateaus of Y, Th, Ti or HREE it is deemed dubious, otherwise it is classified as magmatic. Models are calculated as discussed in the text and uses Boehnke et al.'s (2013) model for saturation, but the results are very similar using Watson & Harrison (1983). For comparison (a) shows the approximate slope of the trend (thick grey arrow) defined by the data for granitic rocks in Claiborne et al. (2006), which is similar to the modelled slope for the tonalite (thick dashed line). The yellow band in (b) defines the field generated by mixing a zircon composition with 3 ppm Ti and 1 ppm Nd, with titanite with 24.4 % Ti and between 1000 and 10000 ppm Nd (Bruand *et al.*, 2020). The band indicates that mixing with titanite is unlikely to explain the trend because it causes a stronger enrichment in Ti compared to Nd.

Fig. 17. Assimilation of host rock through anatexis, back-veining and mixing with zircon transfer. a) Original dioritic magma intrusion at temperatures above zircon saturation. As magma flows and cools, it heats-up the surrounding and releases H_2O. b) The tonalite melts at relatively low temperatures lacking anhydrous peritectic minerals. Granitic dykelets derived from tonalite anatexis back-veins the diorite that is now a cool zircon-saturated mush. The mush deforms in a ductile fashion and granitic melt flow through the pore space of the mush (inset) transferring tonalite zircons and hybridizing the diorite. Zircon xenocrysts are preserved in the zircon-saturated diorite. Size of zircons is exaggerated.

Using zircons to disentangle back-veining and hybridization of diorite dykes : an example from the Gangdese Arc, Tibet

Roberto F. Weinberg[1*], Jean-François Moyen[2], Jian-Kang Yi[3], Di-Cheng Zhu[3], Oliver Nebel[1], Shaorong Chen[3], Qiang Wang[3]

[1]School of Earth, Atmosphere and Environment, Monash University, Clayton, VIC, 3800, Australia.

[2] Université de Lyon, Laboratoire Magmas et Volcans, UJM-UCA-CNRS-IRD, 23 rue Dr. Paul Michelon, 42023 Saint Etienne, France

[3] State Key Laboratory of Geological Processes and Mineral Resources, China University of Geosciences, Beijing 100083, China

*Corresponding author Telephone: +61 3 9905 4902. Fax: +61 3 9905 4903. E-mail: Roberto.weinberg@monash.edu

ABSTRACT

Thermo-chemical modelling and chemical data suggest that the genesis of arc melts commonly involves re-melting of older intrusions, triggered by the injection of mantle-derived melts, followed by magma mixing. Remelting and mixing may lead to complex zircon populations, which can be used to gain insights into the conditions of mixing. This paper investigates a case where such processes can be studied through the compositional and thermal record provided by zircons preserved in a diorite dyke swarm that remelted host rock tonalites in the Gangdese Batholith in Tibet. Autocrystic zircons from the diorite yield consistent ages of 46-47 Ma even though they can be altered, ~~with~~ having highly enriched ~~in~~ trace elements, reaching ~1 wt% in Fe, Ca, Y, U, Th, and anomalously high values of LREE and Ti. Granitic magmas derived from the tonalite, back-veined the dykes and mixed with the dioritic mush, transferring small quantities of 77-79 Ma zircon xenocrysts. The xenocrysts are euhedral with little evidence for resorption, indicating they were apparently stable during the process of tonalite anatexis and transfer to the diorite magma. This requires that: (i) tonalite melting occurred at low temperatures with minimal zircon dissolution, and (ii) the diorite either cooled rapidly before significant resorption of the grains or was already saturated in zircon when mixing occurred. Zircon saturation temperatures of the diorite are relatively low, indicating that xenocrystic zircons were transferred to a highly crystalline dioritic mush. This requires either liquefaction by injection of the back-veining felsic magma to allow for mixing or pervasive throughflow of the diorite mush by the felsic magma leaving behind zircon xenocrysts. The findings suggest that the dykes triggered low-T, water-fluxed melting of the host tonalite, and that these anatectic melts invaded the diorite mush initially through the interstices leading to mixing and this may have caused the breakdown of the crystalline framework leading to liquefaction and renewed magma flow. Dyking and assimilation of wall-rock through back-veining as recorded in these rocks could be common in transcrustal arcs. However, this process could be hidden due to a

combination of the similarity in the isotopic and chemical nature of arc rocks, and resorption of zircon xenocrysts during mixing. This process may explain some complex chemistry of arc magmatic rocks and their minerals that are not easily explained by endmember models, such as pure re-melting of older arc rocks or fractional crystallization of mantle-derived melts.

Key words: geothermometry; magma hybridization: magma mingling; zircon; zircon saturation temperature

INTRODUCTION

The origin of granitic magmas in arcs is at the center of a long-standing debate focused on whether they are derived from the fractionation of basaltic magmas (Jagoutz & Klein, 2018, Müntener & Ulmer, 2018), or the remelting of older arc intrusions (Collins *et al.*, 2020, Moyen *et al.*, 2021, Symington *et al.*, 2014, Weinberg & Dunlap, 2000b) or magma mixing (Reubi & Blundy, 2009). In this regard, evidence for zircon recycling through the system as xenocrysts and antecrysts, combined with Ti-in-zircon thermometry and zircon saturation temperatures, can be used to explore and constrain the processes controlling arc magma evolution, such as whether mixing or assimilation processes were involved and when and how they occurred. The term xenocryst refers here to zircon incorporated from the surrounding host rocks during magma transit and emplacement, whereas the term antecrysts refers to zircon formed in an earlier pulse of magma and that was transferred to the current host. The term autocryst refers to zircon crystallized from the host magma (Miller *et al.*, 2007).

Zircon has a number of properties that makes it useful in constraining magmatic processes. It is an excellent marker of the time of magma crystallization, and its trace elements indicate contemporaneous crystallization or dissolution of other minerals (Rubatto & Hermann, 2007). Its Hf isotopic composition is a sensitive indicator of melt sources and mixing between magmas from different sources (Kemp *et al.*, 2007), and in the case of xenocrystic zircon, Hf isotopic

ratio can be used to determine its source. Further to that, Ti-in-zircon thermometry (Watson *et al.*, 2006), in combination with zircon saturation temperatures of magma (Boehnke *et al.*, 2013, Watson & Harrison, 1983), constrain magma crystallization histories (Schiller & Finger, 2019) and the conditions prevalent during fractionation and mixing (Barnes *et al.*, 2019, Harrison *et al.*, 2007, Miller *et al.*, 2003, Miller *et al.*, 2007, Siégel *et al.*, 2018). These data can then be linked to modeling of the chemical evolution of melt and crystals during crystallization to define zircon saturation temperature and the expected Ti-content of zircons (Barnes *et al.*, 2019, Lee & Bachmann, 2014).

There is often a mismatch between temperatures derived from Ti-in-zircon and from zircon saturation. In samples with many zircon xenocrysts, this mismatch can be caused by the added Zr. In samples with few or no xenocrysts, the mismatch can be caused either by fractional crystallization that changes the Zr content and composition of the interstitial melt, or by changes in the total Zr content through accumulation of zircons and other minerals, or through loss of Zr-rich interstitial melt (Barnes *et al.*, 2019). Zircon saturation temperatures unaccompanied by modeling of fractional crystallization ~~has~~ have been used to suggest that arc granites typically record relatively low zircon saturation temperatures, and to postulate that granitic arc magmas are typically cold (<800 ^{o}C), derived from water-fluxed re-melting of older arc rocks (Collins *et al.*, 2016, Collins *et al.*, 2020). However, zircon saturation temperature is strongly dependent on the initial Zr content of the magma and the evolution of the residual melt composition during crystallization (Miller *et al.*, 2003).

In this paper, we explore the nature of zircon autocrysts in diorite dykes and the fate of zircon xenocrysts transferred from the host rock as a result of anatexis of the host rock, back-veining and mixing, in an outcrop in the Gangdese Batholith in Tibet (Zhu *et al.*, 2015). We use zircon U-Pb ages and grain morphology, combined with zircon saturation temperatures and Ti-in-zircon thermometry to constrain the thermal conditions and magma crystallinity during mixing.

The discussion is underpinned by compositional modelling of a crystallizing melt and the trace element composition of zircons in the evolving melt.

The paper starts with a brief description of the Gangdese Batholith and field relationships between the diorite dykes and host rocks investigated here, including the back-veining and hybridization of the dykes caused by melting of the host. The methodology is then described, followed by characterization of the tonalite and diorite samples and their zircons, including U-Pb dating, Hf-isotope and trace element composition. Whole-rock chemistry is used as the basis for modeling diorite magma crystallization and determining zircon saturation temperatures, as well as to model tonalite melting occurring as the diorite cooled. Modelled zircon saturation temperatures and zircon trace element compositions are also derived from these models and form the basis for discussion of the timing of magma mixing and xenocryst transfer, and the validity of Ti-in-zircon thermometry for these zircons. Results show how these approaches combined can be used to cast light on both the physical details of hybridization, and to exemplify some of the pitfalls associated with interpreting the data.

GANGDESE BATHOLITH AND DABU GEOLOGY

The Gangdese Batholith (Fig. 1) and its western continuation in NW India and Pakistan, the Ladakh and Kohistan Batholiths, is a 2500 km-long calc-alkaline magmatic arc that extends across the southern Tibetan Plateau. It is an Andean-type continental arc formed as a result of oceanic subduction of the Neo-Tethys oceanic lithosphere under the Lhasa Terrane at the Asian continental margin until collision with India at 55 ± 5 Ma shut down the arc (Ji *et al.*, 2009, Yin & Harrison, 2000, Zhu *et al.*, 2019). Magmatism started at ~210 Ma and continued intermittently until collision ended typical subduction-related magmatism and initiated post-collisional magmatism. Subduction-related magmatism is marked by two intense pulses of magmatic activity, one at 90 ± 5 Ma and the other at 55-50 Ma (Zhu *et al.*, 2019). The 90 ± 5

Ma event is linked with ridge subduction (Zhang *et al.*, 2010) or slab rollback (Ma *et al.*, 2013) of the Neo-Tethyan oceanic lithosphere, whereas the 55-50 Ma event is attributed to collision followed by slab breakoff (Zhu *et al.*, 2019) or lithosphere removal (Kapp & DeCelles, 2019). The dykes investigated here belong to the syn-collisional event, which was the most intensive magmatic pulse in the Gangdese belt (Zhu *et al.*, 2019), and includes the voluminous Linzizong volcanic successions (Zhu *et al.*, 2015). Oligocene-Miocene post-collisional magmatism was dominated by silicic rocks resulting from the remelting of arc magmatic rocks and their hybridization with metasomatized lithospheric mantle-derived ultrapotassic melts (e.g. Wang *et al.*, 2018).

Magmatic rocks from the 90 ± 5 Ma events show coherent "depleted mantle-like" zircon $\varepsilon_{Hf}(t)$ (+15 to +10) and positive whole-rock $\varepsilon_{Nd}(t)$ (around +3.0) with a few outliers (Ji *et al.*, 2009, Ma *et al.*, 2013, Zhang *et al.*, 2020, Zhu *et al.*, 2011) that may reflect varying degrees of incorporation of ancient crustal components from the Gangdese basement into the juvenile magmas. Rocks related to the 55 ± 5 Ma event are characterized by a wide range in zircon $\varepsilon_{Hf}(t)$ (between -6 and +15)(Zhu *et al.*, 2022) and whole-rock ε_{Nd} (mostly from +5.0 to −3.0). This more evolved isotopic signature has generally been attributed to the involvement of Indian continent-derived materials (Chu *et al.*, 2011, Wang *et al.*, 2015).

Rocks of the Gangdese arc only rarely have zircon xenocrysts (Zhu *et al.*, 2015). To our knowledge no xenocrysts have been reported in syn-collisional plutonic rocks in this arc and only a few have been reported for the Linzizong volcanic rocks (a few xenocrysts formed at ~90 Ma and older, Zhu *et al.*, 2015). This contrasts with rocks from the Ladakh Batholith, the western continuation of the Gangdese Batholith, which show migmatization and where zircons define a ca. 20 Ma age range (Weinberg & Dunlap, 2000a, White *et al.*, 2011) including recycling of 68 Ma zircons in a 49 Ma magma. Despite this exception, the general rarity of zircon xenocrysts could indicate that: a) remelting of older arc intrusions is a minor process

(Jagoutz & Klein, 2018), b) because zircons are rare in mafic arc rocks, few or no zircons are passed on to the felsic magmas they produce upon remelting, or c) zircon xenocrysts are resorbed during relatively high-temperature melting (Miller *et al.*, 2003).

This paper focuses on an outcrop of the Gangdese Batholith along the road from Zedong to Nyingchi (Fig. 1a) at N29.2625 º and E92.4119 º close to Dabu village. Here, a diorite dike swarm (Fig. 2a, b) intrudes a homogeneous leucocratic tonalite and is back-veined by magmas resulting from the melting of the tonalite host. The dykes are typically 1-3 m wide and are continuous for more than 100 m. In detail, the dyke contacts are irregular at the dm-cm scale, and back-veined (Fig. 2c, d) and dyke tips narrow considerably over a few metres. At the contact, the tonalite has a centimetric layer of more felsic and finer-grained granitic rock that is continuous with dykelets intruding the diorite (Fig. 2c). These dykelets are irregular and intrude and gradually vanish into a heterogeneous diorite (Fig. 2e, f). We have determined whole-rock chemistry and investigated zircons from three samples of diorite and three samples of tonalite host rock, all homogeneous at hand-specimen scale.

METHODOLOGY

Whole-rock geochemical analysis

Fresh rocks samples were crushed, hand-picked, and then powdered using an agate mill to a grain size < 200 mesh at the Yuneng Mineral Separation Service Company at Langfang, Hebei Province, China. Major element analyses of whole rock were conducted on Agilent 7700e ICP-MS at the Wuhan SampleSolution Analytical Technology Co., Ltd., Wuhan, China. The sample pre-treatment of whole rock major element analysis was made by melting method. The detailed sample-digesting procedure was as follows: (1) Sample powder (200 mesh) ~~were~~ was placed in an oven at 105 ℃ for drying of 12 hours; (2) ~1.0g dried sample was accurately weigh~~t~~ed and placed in the ceramic crucible and then heated in a muffle furnace at 1000℃ for 2 hours. After

cooling to 400℃, this sample was placed in the drying vessel and weighted again in order to calculate the loss-on-ignition (LOI); (3) 0.6 g sample powder was mixed with 6.0 g flux and 0.3 g oxidant (NH4NO3) in a Pt crucible, which was placed in the furnace at 1050℃ for 15 minutes. The flux is a mixture of lithium tetraborate, lithium metaborate and lithium fluoride (45:10:5). Then, this ~~melting~~ molten sample was quenched in air for 1 minute to produce flat discs on the fire brick for the XRF analyses.

Zsx Primus II wavelength dispersive X-ray fluorescence spectrometer (XRF) produced by RIGAKU, Japan, was used for the analysis of major elements in the whole rock, The X-ray tube is a 4.0Kw end window Rh target. The analytical ~~test~~ conditions ~~are~~ were voltage: 50kV, current: 60mA. All major element analysis lines are ~~kα~~Kα. The standard curve uses the national standard material of China, rock standard sample: GBW07101-14. The data were corrected by the theoretical α coefficient method. The relative standard deviation (RSD) is less than 2% and the average bias of the measurements was of -0.1% for SiO_2 and has its highest values of + 1.3% for MgO and -1.6% for P_2O_5.

Trace element analyses of whole rock were conducted on Agilent 7700e ICP-MS at the Wuhan SampleSolution Analytical Technology Co., Ltd., Wuhan, China. Four rock reference materials (AGV-2, BHVO-2, BCR-2, and RGM-2) were used to calibrate the contents of trace elements of analytical samples. The detailed sample-digesting procedure was as follows: (1) Sample powder (200 mesh) was placed in an oven at 105 ℃ for drying of 12 hours; (2) 50 mg sample powder was accurately weighed and placed in a Teflon bomb; (3) 1 ml HNO_3 and 1 ml HF were slowly added into the Teflon bomb; (4) Teflon bomb was put~~ted~~ in a stainless steel pressure jacket and heated to 190 ℃ in an oven for >24 hours; (5) after cooling, the Teflon bomb was opened and placed on a hotplate at 140 ℃ and evaporated to incipient dryness, and then 1 ml HNO_3~~3~~ was added and evaporated to dryness again; (6) 1 ml of HNO_3~~3~~, 1 ml of MQ water and 1 ml internal standard solution of 1ppm In were added, and the Teflon bomb was resealed and placed in the

oven at 190 ℃ for >12 hours; (7) the final solution was transferred to a polyethylene bottle and diluted to 100 g by the addition of 2% HNO_3.

LA-ICP-MS zircon U-Pb dating and trace element analysis

Zircons were separated using conventional and magnetic techniques at the Yuneng Mineral Separation Service Company at Langfang, Hebei Province, China. Cathodoluminescence (CL) images, obtained at the Institute of Geology, Chinese Academy of Geological Sciences (Beijing), were used to check the internal textures of single zircons and to select suitable positions for U-Pb dating and Hf isotope analysis. The zircon U–Pb isotope and trace element analyses were carried out using LA-ICP-MS at the Mineral Laser Microprobe Analysis Laboratory (Milma Lab), China University of Geosciences (Beijing). Detailed analytical procedure was described by Zhang et al. (2019) and provided in Supplementary Data Electronic Appendix 1 (all the Electronic Appendices may be downloaded from http://www.petrology.oupjournals.org/). A beam diameter of 35 μm was used for the first round of analyses, whereas for the second round 35 μm was only used for sample 17DB01-2 used and 25 μm for the remainder, which was also used for the third round. Zircon 91500 was used as an external standard for correcting U–Pb dating, and glass NIST 610 was used as an external standard for trace element calibration. Off-line analyses were performed using an Excel-based software ICPMSDataCal (Liu *et al.*, 2008, Liu *et al.*, 2010). Uncertainties in trace element measurements are between 5 and 10%. Common Pb correction was calculated using the program ComPbCorr#3.17 (Andersen, 2002). Concordia diagrams and mean calculations were made using ISOPLOT (v. 3.0) (Ludwig, 2003). Samples were analysed during three sessions, but they gave similar results (Supplementary Data Electronic Appendix 2) and so we present merged results.

Zircon Hf isotopic analysis

Zircon Hf isotopic analyses were conducted in the same domain of the grain as for U-Pb analyses, as defined by CL images. Analyses used a Neptune Plus MC–ICP–MS (~~Thermal~~ Thermo Fisher Scientific, Germany), coupled to a New Wave 193 excimer ArF laser–ablation system at the Milma Lab, China University of Geosciences (Beijing) with a beam size of 35 μm, laser pulse frequency of 8 Hz and energy density of 3.7 J/cm^2. Makeup gas of argon and carrier gas of helium with the addition of nitrogen mixed in a T–branch pipe prior to introduction into the MC–ICP–MS. In the experiment, L4 to H3 Faraday cups were used to collect ^{171}Yb, ^{173}Yb, ^{175}Lu, ^{176}Hf, ^{177}Hf, ^{178}Hf, ^{179}Hf, and ^{180}Hf, respectively with the integration time of 0.131 s. The carrier and makeup gas flows were optimized by a line scan (spot size of 35 μm and scan speed of 5 μm/s) ablating NIST SRM 610 to obtain maximum signal intensity for ^{232}Th, while minimizing ^{232}Th^{16}O/^{232}Th ratio. For each analysis, 50 s integration for gas blank and 50 s integration for signal collection were set up with a total of 800 cycles of raw data. Zircon 91500 (Blichert-Toft, 2008) was used as an external standard for correcting mass discrimination. Zircon standard Plešovice (Sláma *et al.*, 2008) and GJ-1 (Morel *et al.*, 2008) were analyzed as unknown sample that were inserted between zircon 91500 and the samples. Raw data was converted by Neptune Plus software and then processed using Iolite software (Paton *et al.*, 2011).

The initial ^{176}Hf/^{177}Hf ratios and $\varepsilon_{Hf}(t)$ values were calculated with ~~the~~ reference to the chondritic reservoir (CHUR) at the time of zircon growth from the magmas. The decay constant for ^{176}Lu of 1.867×10^{-11} year^{-1} (Söderlund *et al.*, 2004), the chondritic ^{176}Hf/^{177}Hf ratio of 0.282785 and ^{176}Lu/^{177}Hf ratio of 0.0336 (Bouvier *et al.*, 2008) were adopted. Depleted mantle model ages (T_{DM}) were calculated with reference to the depleted mantle at a present–day ^{176}Hf/^{177}Hf ratio of 0.28325, and ^{176}Lu/^{177}Hf = 0.0384 (Griffin *et al.*, 2000). The Hf isotope crustal model age (T_{DM}^{C}) was calculated by assuming that its parental magma was derived from

an average continental crust, with $^{176}Lu/^{177}Hf = 0.015$, that originated from the depleted mantle source (Griffin *et al.*, 2002).

SAMPLES: GEOCHEMISTRY AND PETROGRAPHY

Six samples were investigated: three diorites and three tonalites (see Supplementary Data Electronic Appendix 3 for photographs of the sampling location; coordinates N29.263 and E92.4112). All diorite samples are homogeneous dark grey, and tonalite samples are white to light grey. Whole-rock chemistry in Table 1 shows that the diorites are of intermediate composition ($53 < SiO_2 < 58$ wt.%) and the tonalites felsic ($SiO_2 = 68$-69 wt.%). The rocks have $K_2O/Na_2O < 1$, and both rock types are magnesian and calc-alkalic, based on Frost et al. (2001) descriptors ~~, both rock types are magnesian and calc-alkalic~~ (Fig. 3). The diorites are metaluminous, and the tonalites weakly peraluminous (ASI 1.00 to 1.05) (Fig. 3). Trace elements for both rock types are similar, with negative anomalies ~~in~~ of Nb ~~and Ta~~ and positive anomalies ~~in~~ of Pb and Sr in MORB-normalized diagrams (Fig. 4, Ta also defines a negative anomaly, not shown). HREE exhibit low values of 0.1 – 1 times MORB values, and are lower in the tonalites than in the diorites. All samples have Zr/Hf between 35.6 and 40.7, and La/Yb (not normalized) between 7 and 31 for the tonalite and 6 to 13 for the diorite. Although the two rock types were emplaced some 30 Myr apart (see section 7 below), they display very similar geochemical properties, consistent with their arc setting.

The diorite dykes are fine-grained and massive, and are composed of plagioclase (~70%-75%), biotite (~15%-20%), amphibole (~10%-15%) and quartz (~5%-10%). Plagioclase is zoned with lamellar twinning and the grains are ~~forming~~ subhedral to euhedral ~~grains~~, 100 to 400 μm long, some reaching 1 mm in length, tending towards subequant grains, with crystal faces in some places forming mosaics with 120° intersection between grains. Amphibole is twinned, anhedral to subhedral, with green to brown pleochroism and 50-1500 μm long (generally 100-200 μm). In

sample 18DB01-4, the longer Hbl grains include biotite grains. Biotite is subhedral to euhedral, with light-brown to dark-brown pleochroism, forming isolated grains with rectangular sections 100-1000 μm long (generally 300-400 μm), or forming aggregates with hornblende. The accessory minerals are apatite, zircon, epidote and opaque minerals, and sample 17DB01-2 has titanite. Diorite zircon grains have inclusions and cavities and typically appear in the felsic matrix rather than as inclusions in the mafic minerals, which lack pleochroic haloes. The nature of the zircon grains is described in the next subsection. Apatite forms needles reaching 300-400 μm, occasionally 600 μm, mostly in the felsic matrix, but can be found included in hornblende and biotite. Epidote grains can be either included in biotite as subhedral grains, possibly primary, or in the felsic matrix where it could be a result of alteration of plagioclase. The tonalite is medium grained (grain-size: 1 to 2 mm), lacking a foliation and is composed of plagioclase (~60%-70%), quartz (~20%-30%), biotite (~5%-8%), minor K-feldspar, and with apatite, zircon in among the felsic minerals, and Fe-Ti oxides as accessory phases. Samples 18DB01-3 and 18DB01-1 also have titanite. Plagioclase occurs mainly as subhedral to euhedral laths. Biotite is anhedral to subhedral and displays yellowish to dark-brown pleochroism.

ZIRCON CATHODOLUMINESCENCE

Zircons from the tonalite typically vary in size from 150 to 250 μm (ranging from 100 to 400 μm) and are bipyramidal prismatic with well-developed, fine oscillatory zoning (Fig. 6), or common sector zoning, with some internal truncation of early zonation. Zircons from the diorite vary in size from 100 to 400 μm and the majority of grains have roughly rectangular shapes defined by two parallel rationale faces, forming the longer sides of the rectangle, and two shorter, irregular sides. Some grains have a pyramidal ending. Samples 18DB01-4 and 18DB01-2 have a second morphological type of zircon comprising euhedral grains, with well-developed, fine prismatic oscillatory and sector zoning, similar to zircons from the tonalites (compare grains in Fig. 6c and xenocrysts in Fig. 6d). The latter are considered xenocrysts and comprise

7% of the population (11 grains out a total 162 in the mount for sample 18DB01-4). From this we estimate that they add only ~ 5 ppm Zr to the 74 ppm content of the whole rock for this sample. Sample 18DB01-2 has an even smaller proportion of these xenocrystic zircons. We neglect this added amount when considering zircon saturation temperatures below.

CL images of zircons from the diorite define three distinct zircon groups (excluding the xenocrysts in samples 18DB01-4 and 18DB01-2): a) clean and grey grains; b) grains with considerable clean, grey parts and with metamict domains with cauliflower-like pattern and partly quenched to black CL; and c) fully metamict grains with or without very thin grey rims (Fig. 6) that are either entirely or mostly quenched, preserving weak cauliflower-like patterns in very dark regions. Based on these distinctions, the spots were divided into 4 types depending on their position: Type 1 are from clean and grey areas in grains from group (a); Type 2 are spots from the clean, grey part of grains from group (b), and Type 3 are from the metamict part of the same grains; and Type 4 are spots from fully metamict, quenched grains of group (c). Types 3 and 4 are commonly associated with anomalous zircon trace element compositions as we will see in the next subsection.

ZIRCON GEOCHEMISTRY

Zircons from the tonalite host rock and xenocrysts from diorites have similar trace element composition, with U and Th contents below 2100 and 1800 ppm, respectively, similar REE patterns (Fig. 7, Supplementary Data Electronic Appendix 2), and Ti contents between 1 and 10 ppm (Supplementary Data Electronic Appendix 2). These values contrast starkly with the autocrysts from the diorite that show higher abundances of REE (Fig. 7) and anomalously high values of U-Th-Ca-Fe-Y, each with values approaching or surpassing 1 wt.% (Fig. 8) (for more zircons with high trace element contents see Gagnevin *et al.*, 2010). Their Ti contents are between 1 and >500 ppm (15 out 260 analyses yielded Ti > 30 ppm) (Fig. 8d).

Hafnium is an incompatible element during crystallization of felsic magmas (Claiborne *et al.*, 2010), with a bulk partition coefficient remaining below one even during zircon crystallization, despite zircon's high Hf uptake. Conversely, titanium, is a compatible element that enters mafic silicates and common accessories, such as Fe-Ti oxides and titanite. Thus, during magma crystallization, Hf increases while Ti decreases in the melt leading to the negative trend of Hf against Ti in Fig. 9. The same is not true for U, Th and Yb, which show unexpected positive trends against Ti, for diorite zircons, indicative of an apparently compatible behaviour of these elements during crystallization (Fig. 9), contrasting with the incompatible trends in Claiborne et al. (2010).

ZIRCON U-Pb AGES AND Hf ISOTOPES

The three tonalite and three diorite rock samples in Table 1were dated. The diorite samples yielded ages of 46-47 Ma and the tonalite samples yielded ages of 77-79 Ma and (Figs. 10 and 11). Given the close mean ages for the diorite samples and their relatively large spread, indicated by high MSWDs (>4), we consider that the dykes were essentially contemporaneous. Zircons with CL types 3 and 4 with quenched, metamictic CL features, tend to be richer in U, Th and other trace elements compared to types 1 and 2 (Fig. 8). In order to determine if types 3 and 4 have been affected by Pb-loss, U-Pb dates were compared with those for CL types 1 and 2 (Figs. 10d and 12). Results show no significant differences and dates vary from ~44 to 51 Ma independently of CL type. We have therefore considered all concordant U-Pb analyses.

Two tonalite samples have ages that overlap within error at ~79 Ma and have small MSWD (Fig. 11a,c). The third sample, however, has a slightly younger mean age at 77.2 ± 0.5 Ma and a high MSWD=4.8 (Fig. 11b). This sample has three times more analyses than the other two, suggesting that the tonalites may have a large true spread in dates. Two of the three diorite samples (Fig. 11d-e) have xenocrysts with the same range of dates and same trace element

chemistry as the tonalite zircons (Fig. 7) confirming the interpretation based on CL images (Fig. 6). Analyses with >10% discordancy as well as a small number of outliers were not considered here.

Hafnium isotopes for subpopulations of the dated zircons from all 6 samples were obtained. They are typical of those of the Gangdese arc yielding $\varepsilon_{Hf(t)}$ between +4 and +13 (*Fig. 13; Supplementary Data Electronic Appendix 2*). The values for the tonalites are similar to those of the diorite with the exception that the latter have a wider variation (+4 to +13 compared to +6 to +10). Xenocrysts of diorite sample 18DB01-4 plot together with the tonalite zircons.

CHEMICAL MODELLING OF MELT EVOLUTION AND ZIRCON CRYSTALLIZATION

Methods

The crystallization of zircons during cooling of magmas has been modelled using a procedure similar to the ones described by Schiller and Finger (2019) (see also Harrison *et al.*, 2007, Kirkland *et al.*, 2021). In a cooling closed system, magma crystallizes and the residual melt evolves chemically. Zr is initially incompatible and its content increases until zircon becomes saturated at which point it becomes compatible and starts decreasing in the melt upon further fractionation. Thus, zircon crystallizes out of this residual melt, whose composition evolves and differs from the composition of the bulk rock. In a closed-system, the melting process upon heating follows the opposite direction to the one described above.

In our models, we first calculate the closed-system evolution of the rock using phase equilibria, and in particular the amount and composition of the residual melt at a given temperature. Zr is partitioned between melt and solids using known partition coefficients, and the Zr content in the melt is compared with the zircon saturation value; any Zr above the saturation value at this point

355 is then used to form zircon. Other trace elements are then partitioned between liquid and all
356 solids, zircon included. The most important assumptions in this process are that the composition
357 of the diorite and tonalite correspond to melt compositions, and that this is a closed system
358 behaviour, i.e. we assume batch rather than fractional crystallization (or indeed batch melting, as
359 both are exactly similar in a closed system): neither melt nor crystals are removed from the
360 system, and the system properties are calculated independently for each point.

361 The details of the procedure are given in Supplementary Data Electronic Appendix 5. Phase
362 equilibrium is modelled using PerpleX version 6.9.0 (Connolly, 2005, Connolly & Petrini,
363 2002) and the minerals and melt models by Holland et al. (2018), that allow incorporation of
364 Fe^{3+} and Ti, using one-dimensional T profiles at a fixed P of 5 kbar. Zircon saturation values are
365 based on the saturation model of Boehnke et al. (2013) and results for the model of Watson and
366 Harrison (1983) are also shown for comparison. These models include a dependence on the melt
367 composition expressed as the parameter M, the cation ratio (Na + K + 2Ca)/(Al x Si), which is
368 obtained from the phase equilibrium model. Partition coefficient values for trace elements vary
369 considerably in the literature. We use those compiled by Laurent (2012), using values for felsic
370 rocks (SiO_2 > 63 %), which are appropriate for both rock types since the residual melt, even in
371 the diorite, is almost always at these values. For Th, U, HFSE and REE, the zircon-melt
372 partition coefficients are modified using the temperature parametrization of Claiborne et al.
373 (2018). Temperature-dependent coefficients for other minerals are unavailable and have the
374 potential to modify our results. Finally, we calculated Ti contents in zircon as a function of
375 temperature using the model of Ferry and Watson (2007). As their equation relies on the activity
376 of Si and Ti, both were calculated from the phase equilibrium model (following Schiller &
377 Finger, 2019). PerpleX outputs chemical potentials that must be converted into activities.

378 Given the pressure dependence of ~5 ^{o}C/kb for the Ti-in-zircon thermometer determined by
379 Ferry and Watson (2007), our calculated temperatures could be overestimates for the lower

pressure used here (5 kb) compared to the 10 kb used in Ferry and Watson's calibration. All parameters are calculated along the 1D temperature profile used for phase equilibrium, simulating closed-system cooling (or heating) of the magma or the rock. After the phase equilibrium modelling, all steps are performed using a homemade R script (available from J-F Moyen on request).

Evolution of melt and zircon

Crystallization of a melt in a closed system is modelled using diorite sample 18DB01-4, the most mafic of the diorites with 54% SiO_2 and 73 ppm Zr. We carried out two calculations, with 3 and 6 % H_2O. A value close to the average of the tonalite samples was used with SiO_2 = 68.3 % and 140 ppm Zr (Table 1). A low H_2O content of 2 wt.% was assumed for modelling the tonalite in order to investigate its remelting triggered by limited quantities of H_2O delivered from the diorite intrusion.

In the model, the diorite crystallizes Amp-Pl-Cpx accompanied later by Bt that increases in proportion towards the end of the crystallization history, with quartz appearing close to the solidus temperature (T_{sol} =677 ^oC; Fig. 14a). Water saturation is reached at 687 ^oC, close to the solidus for the case with 3 wt.% H_2O, and at 754 ^oC for 6 wt.% H_2O, nearly 80 ^oC above the solidus. The tonalite crystallizes Pl+Opx at high temperature and at ~800 °C, Opx reacts to Bt. Kfs appears relatively late in the history and H_2O becomes saturated a few degrees above the solidus (T_{sol}= 650 ^oC). The evolution of the melt fraction for all calculations is depicted in Fig. 14b.

The Zr content in the melt increases with crystallization until the melt reaches zircon saturation (Fig. 14c). After this point the melt follows the zircon saturation curve controlled primarily by temperature and secondarily by melt composition, expressed by its M-value that evolves as

crystallization proceeds (Fig. 14d). The temperature of zircon saturation for the diorite with 73 ppm Zr in the melt at the start is 714 or 711 °C using Boehnke et al.'s (2013) calibration, and is only weakly sensitive to the H_2O content, corresponding to melt fractions of 23 to 26 %, respectively. The saturation temperature is ~ 30 - 40 °C higher when using the calibration of Watson and Harrison (1983) corresponding to melt fractions of 26 to 35 wt.%. For the case with 6 wt.% H_2O, zircon saturation is reached at temperatures lower than H_2O saturation. The tonalite initially with 140 ppm Zr and 2 wt.% H_2O reaches zircon saturation at 805 °C and 41% melt (Boehnke *et al.*, 2013), while H_2O becomes saturated a few degrees before the solidus at 650 °C. Thus, zircon saturation temperature of the tonalite is ~ 150 °C above the solidus and 100 °C higher than that of the diorite due to its lower M-values and higher Zr content (140 ppm vs 73 ppm).

For the diorite models, crystallization leads to a gradual decrease in the M value of the melt fraction from close to 2.2 at the liquidus, to a minimum of 1.4 at the solidus (Fig. 14d). The tonalite is different. M values vary only weakly, first decreasing from M=1.45 at the liquidus (not shown) to 1.32 at the start of crystallization of quartz and biotite at which point M increases gently reaching 1.40 at the solidus, similar to the residual melt in the diorite close to its solidus.

The $a(SiO_2)$ and $a(TiO_2)$ in Fig. 14e were used to calculate the expected value of Ti-in-zircon. Despite considerable variation in activities during crystallization, the calculated Ti-in-zircon curves are similar to those calculated using fixed value of $a(SiO_2)$ =1 and $a(TiO_2)$ =0.7 (compare continuous and dashed lines in Fig. 14f). Thus, these values are a good approximation of the behaviour of the metaluminous magmas (see discussion in Schiller & Finger, 2019).

Modelling results indicate that prior to zircon saturation in the dioritic magma, most Zr is hosted in the melt with some going initially into hornblende and biotite as magma cools. At zircon saturation, nearly half the Zr is hosted by these other minerals (Fig. 14g) but as the proportion of zircon increases, ~~they~~ these non-zircon minerals ~~lose Zr~~ record a decrease in the total Zr content that they host. At the solidus, a little over 20 ppm is hosted by non-zircon minerals, and the remaining ~50 ppm is hosted by zircon, corresponding to a (modal) proportion of just under 0.01 % zircon. During tonalite crystallization, few minerals take in Zr, so nearly all of the ~140 ppm is hosted in zircon, corresponding to about 0.03 modal % in the rock.

The decrease in Zr content hosted by non-zircon minerals is a result of the modeling calculations considering the whole-rock chemical composition and distributing the available elements according to the mineral proportions stable at the new temperature. This means that minerals and melt are in equilibrium at all times during cooling. After zircon becomes saturated, the Zr content in the melt decreases as temperature decreases so that the amount of Zr that goes into the non-zircon minerals decreases according to the partition coefficient, kept constant. In a real system, complete equilibrium at all times during cooling may not occur. In this case, some Zr may be trapped in early-formed minerals, in disequilibrium with the cooling melt. The net effect would be slightly less zircon being formed than in the calculations presented.

DISCUSSION

Ages and source of xenocrysts

Field evidence in Fig. 2 indicates that tonalite remelted at the contact with the diorite and back-veined the dykes, causing hybridization that is recorded by felsic dykelets and irregular diffuse leucocratic patches in the diorite. Melting of the tonalite is inferred to be at relatively low temperatures in the presence of aqueous fluids because of the leucocratic nature of the tonalites

with little biotite available and no anhydrous peritectic phase such as garnet or orthopyroxene associated with anatexis.

The 46-47 Ma age of the diorite dykes places them amongst the syn-collisional, compositionally diverse magmatic flare-up recorded in the southern Lhasa terrane centred around ~50±5 Ma (Zhu *et al.*, 2019). These rocks typically have a wide range of $\varepsilon_{Hf(t)}$ varying between -6 and +15 (Fig. 4 in Zhu *et al.*, 2022). The tonalite age of 77-79 Ma with $\varepsilon_{Hf(t)} = +9 \pm 1$ makes it part of the pre-collisional magmatism that had $\varepsilon_{Hf(t)}$ values between +4 and +15.

Two out of three diorite samples have older zircon xenocrysts (sample 18DB01-4 and 18DB01-2) that comprise ≤7% of the grains imaged for each diorite sample. These xenocrysts are likely derived from the tonalite host rock as they have the same distinctive euhedral prismatic shape and internal CL zonation (Fig. 6), similar $\varepsilon_{Hf(t)}$ values (Fig. 13), the same range of U-Pb dates from ~80 Ma to 69 Ma (Fig. 11) and similar trace element composition (Fig. 7).

Anomalous zircon composition

Figures 8 and 9 indicate that the diorite zircons have anomalous trace element composition. They have very high trace elements contents, such as U-Th-HREE-Y-Ti, and low values of LREE index (LREE-I, Bell *et al.*, 2016). The elements U, Th and Y define positive trends with Ti. Given that Ti is expected to decrease in zircon during cooling and melt fractionation, the trends suggest that these elements behave compatibly during crystallization, contrary to expectations (Claiborne *et al.*, 2010). Hf is incompatible in the melt defining a negative trend against Ti, as expected, but unexpectedly it also defines a negative trend against U due to its compatible behaviour. The high contents of trace elements indicate the that self-irradiated, damaged diorite zircons may have been altered as a result of reaction with melts or fluids

(Geisler *et al.*, 2007, Hoskin, 2005, Hoskin & Schaltegger, 2003). For example, the values of Ti in some analyses are above 30 ppm, reaching up to a few hundred ppm, and these are generally accompanied by high concentration of other trace elements (Fig. 8).

Metamict and quenched zircon types 3 and 4 (Fig. 6) tend to have high concentration of trace elements (Ca, Fe, REE, U and Th) in contrast to zircon types 1 and 2 (Fig. 8). Despite these differences, they all yield similar U-Pb dates with no systematic change that could be ascribed to Pb-loss (Figs. 10d and 12). In order to determine the extent of alteration, we investigated the relationships between CL types (Fig. 6) and trace element chemistry for each analytical spot, considering signal counts of each analysis during data acquisition using the ICPMSDataCal software. The main findings are that spots with anomalously high trace element abundances typically have one or more of these features:

a) high Th+U contents (>3000 ppm) commonly but not always located in zones of quenched CL. We note however, that there are quenched areas with low Th+U contents (<1000 ppm) indicating that quenching may be related to other factors;
b) anomalous values of LREE, expressed by low values of LREE-I (Fig. 8a,b);
c) anomalous signal plateaus of Fe in CL quenched areas, commonly accompanied by other anomalous signal plateaus for Ca, Ti, LREE, Th and Y (Fig. 15), probably a result of inclusions or domains affected by self-irradiation damage and reaction between zircon and fluid or melt (Geisler *et al.*, 2007);
d) located in zircon sectors characterized by CL types 3 and 4.

We found that taking any of these indicators separately is an insufficient predictor of the spot having a number of chemical anomalies. The strongest predictor of zircons having several such anomalies is having anomalous peaks or plateaus in the count curves, in particular for Fe and Ca. Therefore, we used anomalous peaks or plateaus of Fe and Ca as key indicators of

metamictization and re-equilibration (Geisler *et al.*, 2007) and exclude these analyses from consideration in Ti-in-zircon thermometry. While in most cases, analyses with anomalies of Fe and Ca generally have at least one other feature in the list above, there is a very small number of analyses that have no other indicator of alteration. These were also removed. We have checked the remainder of the data for Ti count anomalies, and found only four analyses with minor Ti anomalous peaks or plateaus. These lacked Fe or Ca anomaly and were therefore evaluated with the rest of the results in the next section.

Uranium, Th and HREE normally behave incompatibly during crystallization and are expected to define a negative trend when plotted against Ti contents (Claiborne *et al.*, 2010). However, these elements in diorite zircons behave compatibly defining a positive trend instead (Fig. 9). In order to further evaluate this behaviour, we have compared the observed data with modelled zircon composition. For both tonalite and diorite, zircon composition is scattered, and modelled composition evolution reproduces them poorly (Fig. 16). The analytical results define a positively correlated array, at high angle to the negative trend of the model calculations or the trend defined by the zircons of Claiborne et al. (2010) (grey field in Fig. 16). This means that the processes controlling zircon trace element intake in the diorite is unaccounted for by our calculations and used assumptions.

Ti-in-zircon thermometry

In this section, only zircons that passed the culling described above, deemed as potentially unaltered, were considered. As we have seen in section 8, converting Ti contents to temperatures requires assumptions regarding TiO_2 and SiO_2 activities. Figure 14f compares two results, one using "conventional" estimates of $a(SIO_2) = 1$ and $a(TiO_2) = 0.7$, and the other using the calculated activities at each point during crystallization (Fig. 14e). The difference between the two is small.

517 *Zircons from tonalites*

518 Analyses of 122 spots from the three tonalite samples and xenocrysts from the diorite, yielded a
519 range in Ti contents from 1.2 to 9.2 ppm (1.2 to 8.5 ppm for the xenocrysts), with a very similar
520 mean (3.3 ppm for the tonalites, 4.0 ppm for the xenocrysts). These values yield temperatures
521 (using ideal activities) from 577 to 786 ^{o}C. Uncertainties for Ti values between 1-2 ppm are
522 between 20-30%, decreasing to below 10% for values >5 ppm, with a detection limit of ~0.5
523 ppm. While the low-T end of the range likely reflects sub-solidus resetting, the high-T end is
524 lower than but comparable to the zircon saturation temperatures estimated at between 800 and
525 820 °C (depending on the model used, Fig. 14c).

526 *Zircons from diorites*

527 The Ti-in-zircon values of diorite autocrysts are less well-behaved. Zircons from
528 sample18DB01-4 have Ti contents between 1.4 and 17.7 ppm, which translates to temperatures
529 between 613 and 895 ˚C (using a(SiO_2) = 1, a(TiO_2) = 0.7), or 614 and 842 ˚C (using activities
530 from our model). Since our models also predict the onset of zircon crystallization at low
531 temperatures (710 - 750 ˚C depending on the model chosen, Fig. 14c), this is a significant
532 mismatch, and these "hot" zircons cannot be simply related to zircon saturation temperature
533 estimates.

534 Similarly, for sample 17DB01-2, Ti ranges between 1.3 and 16.3 ppm (equivalent to a
535 maximum T of 832 ˚C), with a mean of 7.9 ppm. Sample 18DB01-2 (with higher Zr =102 ppm
536 and hence a higher value of the zircon saturation temperature) has Ti contents between 1.5 and

537 23.3 ppm (equivalent to a maximum T of 915 ˚C), and a mean of 7.1 ppm. Thus, in all cases the
538 maximum Ti-in-zircon temperatures are more than 100 ºC above the estimated zircon saturation
539 temperature, when the diorite still had ~40-55% melt fraction depending on the H_2O content. In
540 all cases, the calculated temperatures for the lowest Ti grains are up to 50 ˚C below the solidus.
541 As our model relies on zircon saturation in melt, we cannot model subsolidus resetting of Ti
542 composition (discussed in Fu *et al.*, 2008).

543 *Modelling zircon crystallization*

544 While the tonalite zircons yield Ti-in-zircon temperatures that cover the expected range derived
545 from the calculations, the diorite zircons do not. For these, the maximum Ti-in-zircon
546 temperatures surpass substantially the modelled zircon saturation temperature in common with
547 findings elsewhere (Barnes *et al.*, 2019, Claiborne *et al.*, 2006, Harrison *et al.*, 2007).

548 There are two ways of calculating the zircon saturation temperatures. One approach uses the
549 whole-rock composition as an estimate of the magma composition. It assumes that zircon would
550 crystallize from a liquid whose composition equates that of the rock, for which a high M value
551 results in unrealistically high Zr solubility and low saturation temperatures (see Harrison *et al.*,
552 2007). In this case, diorite sample 18DB01-4, with M=2.4, would yield a saturation temperature
553 of 575 ˚C, which should preclude it from crystallizing zircon. This mismatch with reality is

554 because the approach does not include the evolution of the residual melt with crystallization,
555 which would cause the Zr content to increase and the melt composition to evolve to lower M
556 values, with lower Zr solubility.

557 The second approach, the one taken here, considers the evolving composition of the melt during
558 crystallization and determines when zircon crystallizes from this residual liquid, whose
559 composition departs from the bulk composition, becoming enriched in Zr and increasingly more
560 felsic (lower M) (Harrison *et al.*, 2007, Lee & Bachmann, 2014). This approach leads to higher
561 and more realistic zircon saturation temperatures than the first approach (Harrison *et al.*, 2007).
562 Here, using this approach and including Zr uptake by other minerals such as Hbl, Bt and Pl, we
563 found zircon saturation occurs just above 700 °C for the diorite models, some 100 °C lower than
564 the maximum values derived from Ti-in-zircon, as seen in the previous subsection. This
565 discrepancy implies that some other processes must be at play.

566 *Significance of high-Ti zircons*

567 A population of zircons from the diorites show Ti contents > 7 ppm, corresponding to > ~730
568 °C, higher than the zircon saturation temperature derived from our models. These same diorite
569 zircons have high contents of U, Th, HREE that define apparently compatible trends (Figs. 9
570 and 16). Several explanations, not necessarily mutually exclusive, could account for these
571 observations:

572 a) High-T zircons are xenocrysts or antecrysts. This is unlikely because the high-T zircons have
573 the same internal texture, $\varepsilon_{Hf(t)}$ and U-Pb ages as low-T grains.

574 b) Presence of inclusions or "non-formula" impurities in zircons. The diorite zircons do have
575 inclusions and cavities and are also partly metamictic with quenched CL images. The high-Ti
576 values, coupled with high Th and REE values, could be due to inclusions of Ti-rich phases, such
577 as titanite or allanite, where the trends with Ti would represent mixing lines. We have excluded
578 analyses with anomalous peaks or plateaus of trace elements in the count curves (section 9.2),
579 and modelling results show that inclusions of titanite would cause a much more rapid increase in
580 Ti contents compared to Nd (Fig. 16a). However, it is possible that metamictization and reaction
581 with fluids and subsequent recrystallization (Geisler *et al.*, 2007) gave rise to micrometer-scale
582 inclusions of assorted Ti-U-Th-REE rich minerals in the zircon matrix. Alternatively, self-
583 irradiation damage gave rise to pore space that hosts "non-formula" impurities (Geisler *et al.*,
584 2007). At present, either alternative is valid and we conclude that despite exclusion of
585 anomalous analyses, the Ti contents of the remaining zircons may also have been affected,
586 explaining the high-Ti contents and positive trend between Ti and U-Th-Yb (Fig. 9). If this is
587 the case, the Ti-in-zircon values of the diorite zircons do not reflect temperature of
588 crystallization (Fu *et al.*, 2008).

589 c) Loss of Zr during diorite crystallization (Barnes *et al.*, 2019). In this case, the original melt
590 had higher Zr content than the bulk rock has now, because some of the high-Zr melt was
591 extracted leaving behind a poorer cumulate. If the diorite melt had initially higher Zr than the
592 final rock, it would have reached zircon saturation at higher temperatures than the ones

593 calculated in Fig. 14. The interstitial melt of a crystallizing dioritic magma becomes increasingly
594 enriched in Zr until zircon saturation, at which point the melt starts to lose Zr due to zircon
595 precipitation (Barnes *et al.*, 2019, Harrison *et al.*, 2007, Lee & Bachmann, 2014). If part of this
596 Zr-rich interstitial melt is extracted, the remaining mush or magma will be impoverished in Zr,
597 while retaining some of the early-formed high-T zircons. Any remaining interstitial melt
598 continues to crystallize zircon as the magma continues to cool. Thus, despite relatively low final
599 Zr content, this rock will have early-formed hot zircons that mark the true, high-saturation
600 temperature of the original magma (see Barnes *et al.*, 2019). This alternative is problematic for
601 the Dabu rocks because to reach zircon saturation at ~830-840 ^{o}C (the upper temperatures
602 obtained by Ti-in-zircon thermometry for our samples), the dioritic melt would need to have had
603 an unrealistically high Zr content of >300 ppm. Therefore, while this process may have
604 contributed to decreasing the Zr content of the evolving magma, and therefore the inferred
605 zircon saturation temperature, it is unlikely to be the main reason for the high Ti-values of some
606 zircons.

607 On balance, it is likely that the trace element trends in Fig. 9 and the Ti-content of diorite
608 zircons reflect zircon alteration during metamictization, where high contents of trace elements
609 are hosted either in pore space in amorphous remnants inside the grains or in inclusions resulting
610 from recrystallization of the amorphous, damaged zones (Geisler *et al.*, 2007). Consequently, the
611 Ti content in the diorite zircons is not a reliable measure of crystallization temperature.

612 **Preservation of euhedral zircon xenocrysts**

613 Euhedral zircon xenocrysts from the tonalite preserved in two diorite samples (18DB01-4 and
614 18BD01-2) show negligible dissolution. This is inferred from the similarity between CL images
615 of xenocrysts and tonalite zircons: they are euhedral with well-developed oscillatory zoning,

lacking obvious truncation of the oscillatory zoning in the outer part of the zircons. It is possible that a thin rim may have been dissolved or grown during final crystallization of the diorite, but they have not been recognized. In this section, we explore how these euhedral xenocrysts may have been preserved during the melting of the tonalite and mixing with the diorite, two steps where they could have been resorbed.

We envisage three possible processes that would prevent significant zircon resorption during melting of tonalite: small melt fraction during anatexis, zircon grains protected as inclusions in biotite, or rapid melting and transfer to the diorite with little time for resorption. All alternatives remain open. Once transferred to the dioritic magma, zircon xenocrysts would be partly or completely resorbed if the diorite was undersaturated. The fact that they are well preserved, and that corroded oval zircons or zircon cores have not been found, can be interpreted in several ways (see discussion in Barnes *et al.*, 2019, Miller *et al.*, 2007):

1. A zircon--undersaturated diorite magma crystallized rapidly after receiving the xenocrysts preventing their dissolution. While we cannot entirely dismiss this possibility, we note that: the diorite is fine-grained but not aphanitic or glassy, and lacks chilled margins against the host rock; granitic magma mixed with the mafic magma, suggesting that there was enough time for interaction and widespread transfer of zircons; and the diorite magma produced zircon autocrysts up to 0.4 mm long with rational crystal faces after it became zircon-saturated at low T. Combined, these features suggest that if the diorite magma was undersaturated, there would have been enough time for the xenocrysts

636 to be partly consumed before the magma becoming saturated and crystallizing its own
637 zircon autocrysts.
638 2. Zircons could have been transferred as inclusions in residual biotite from the
639 tonalite in the granitic melt (e.g. Clemens, 2003). However, we found no pleochroic haloes
640 in biotite in the diorite (Fig. 5) and biotite would have been unstable in the dioritic magma
641 at T>810 °C (for the diorite with 3 wt.% H_2O), or > 750 °C (for 6 wt.% H_2O) (Fig. 14a).
642 In this case, biotite would have reacted out and zircons exposed to the melt. Thus,
643 armouring would have been possible only if biotite transfer occurred at relatively low
644 temperatures, for which the diorite would have been a mush with <40% melt (Fig. 14b).
645 While we cannot discount this possibility, we do not find support for it.
646 3. If we reject the results from Ti-in-zircon thermometry considering that it could
647 have been affected by alteration, and consider instead that the zircon saturation
648 temperatures in Fig. 14 approach the true value, then the Dabu diorite would have reached
649 zircon saturation between 700 to 750 ˚C. At these conditions, the diorite would have been a
650 crystalline mush with only between ~23% and ~ 26% interstitial melt. In this case, the
651 extensive magma mixing observed within the dyke would require either pervasive flow of
652 the granitic melt through the mush, or liquefaction of the mushy diorite possibly caused by
653 the addition of melt derived from tonalite anatexis.

Bringing together the field evidence, the data and the considerations regarding zircon saturation temperature (point 3 above), we propose the following sequence of events (Fig. 17): the dykes were paths of H_2O-rich dioritic magmas that released heat and H_2O to the surroundings as the magma became a crystalline mush. This triggered water-fluxed melting of the tonalite that released zircon grains into an anatectic granitic melt. This melt back-veined and mixed with the diorite transferring tonalite zircons to the dioritic magma, where they remained stable (or nearly so), explaining their well-preserved euhedral shapes and internal zonation. Preservation of the xenocrysts could have been either through armouring, for which we find no evidence, or through transfer to a zircon-saturated dioritic medium. Even assuming large uncertainties in the Zr content of the original melt caused by melt gain or loss during crystallization, zircon saturation temperature would have been reached when the diorite was a crystalline mush. Therefore, zircons were likely transferred to a dioritic mush through mixing. How did this occur? Mushes are permeable solids, open to invasion of foreign magmas (Xu *et al.*, 2021) and prone to liquefaction (Weinberg *et al.*, 2021). The granitic magma may have exploited permeable porous pathways through the mush leading to hybridization and influx of zircon xenocrysts into the matrix of the mush. This same ingress of granitic magma may have caused liquefaction and remobilization of the mush favouring further mixing. Both these processes could give rise to the variety of mingling features in Fig. 2c,d, including the irregular, infolded felsic dykes commonly

672 with gradational contacts with the mafic rocks, and blocks of better-preserved diorites in a
673 hybrid rock. A detailed textural investigation of the different steps in the hybridization process
674 in Fig. 2, with particular focus on disequilibrium textures and mineral zonation, might better
675 reveal the nature of these processes. Determining the existence of narrow, younger rims around
676 the xenocrysts, and with that better visualizing the shape of the xenocrystic grains, might help
677 support this interpretation.

678 CONCLUSIONS

679 The intrusion of the Dabu diorite dyke swarm at 46-47 Ma is part of the waning stages of the
680 syn-collisional magmatic flare-up of the Gangdese belt. The outcrops in Dabu record how these
681 dykes assimilated the 77-79 Ma host tonalite by remelting it and then mixing with the newly
682 formed melt. The tonalite melted at low temperatures fluxed by water likely released with heat
683 by the dykes. The transfer of tonalite zircons to and their preservation in the diorite dykes
684 provides an opportunity to explore the conditions of magma hybridization and the limits of
685 zircon-based thermometry. Given the importance of dykes as feeders of large magma bodies,
686 and the high H_2O contents and temperatures prevalent in active magmatic arcs, the Dabu dykes
687 could represent a common process of hybridization in magmatic arcs, akin to the mixing-
688 assimilation-storage-homogenization, MASH, hypothesis (Hildreth & Moorbath, 1988).

689 We found that the Ti-in-zircon temperature estimations for the tonalite matched well the range
690 defined by zircon saturation temperature predicted by modelling of crystallization/melting of the
691 tonalite. However, the same is not true for dioritic zircon autocrysts. These yield Ti-in-zircon
692 temperatures ranging from below the solidus to >100 ^{o}C above the zircon saturation
693 temperatures. This discrepancy could be related either to loss of Zr during diorite crystallization
694 (Barnes *et al.*, 2019) or to alteration and recrystallization of the zircons (Geisler *et al.*, 2007),
695 indicated by quenched CL and high Ti contents, as well as U, Th, Ca, Fe, Y, REE (or low

LREE-I; Fig. 8). Either way, the results show how even through exclusion of zircons with obvious indicators of alteration, they may still have unreliable Ti values, defining unexpected trends against other trace elements (Fig. 16).

Interestingly, but not surprisingly, the tonalite with ~140 ppm Zr has a zircon saturation temperature close to 100 °C higher than the diorite with half the amount of Zr, indicating yet again that this temperature does not constrain the temperature of magma formation. However, for the Dabu rocks, zircon saturation temperature is useful in constraining the crystallinity of the diorite intrusion at the time of hybridization. This is because a striking feature of these rocks is that the zircon xenocrysts from the tonalite record little resorption, requiring that the xenocrysts be either armoured in biotite during mixing, or that they be exposed to a low-temperature granitic melt first, and then transferred to a zircon-saturated diorite. The absence of pleochroic haloes in biotite in the diorite and the instability of biotite in hot dioritic magmas suggest that armouring is unlikely. The low-temperature zircon saturation of ~715 °C ensures that the diorite would have been a high crystallinity mush with only ~25 wt.% melt at the time of zircon saturation. Even if the Zr content were doubled or trebled, zircon saturation in the diorite would still have occurred in a mush. Thus, we conclude that hybridization occurred in a zircon saturated mush through melt leak-off from invading granitic veins into the pore-space of the mush, possibly accompanied by liquefaction (Weinberg *et al.*, 2021). We argue that pore-invasion combined with the liquefaction of mushes is a powerful mixing process. Because of its stealthy nature, this process of magma mixing in dykes could be important during the build-up of arcs feeding large magma reservoirs with hybrid magmas.

The Dabu dyke swarm represents one end-member of zircon behavior during hybridization where xenocrysts are preserved with minimal resorption. This behavior helped us constrain the nature and conditions of zircon transfer and magma hybridization. However, the general rarity of zircon xenocrysts in magmatic rocks of the Gangdese arc (e.g. Zhu *et al.*, 2015) suggests that

721 complete zircon resorption could be common, leaving few tools to recognize the remelting of
722 older arc rocks and magma hybridization. This is especially true when the arc has a narrow
723 range of radioactive isotope ratios. Thus, assimilation through remelting of older arc rocks,
724 followed by hybridization and homogenization (MASH, Hildreth & Moorbath, 1988) could be
725 widespread with little evidence preserved. In such cases, disentangling magma evolution and the
726 nature of magma hybridization require detailed field documentation accompanied by
727 investigation of fine chemical and isotopic zonation of a range of accessories and rock-forming
728 minerals (e.g. Barnes *et al.*, 2021, Chambers *et al.*, 2020).

729 ## FUNDING

730 This research was financially co-supported by the National Natural Science Foundation of China
731 (42121002 and 91755207), the Second Tibetan Plateau Scientific Expedition and Research
732 Program (STEP) (2019QZKK0702), and the 111 project (B18048).

733 ## SUPPLEMENTARY DATA

734 Supplementary data are available at Journal of Petrology online.

735 **Data Availability**

736 The data underlying this article are available in the article and in its online supplementary
737 material.

738 ## ACKNOWLEDGEMENTS

739 We thank Vali Memeti, Calvin Miller and Bill Collins for careful and insightful reviews that
740 much improved the original manuscript.

741 ## REFERENCES

742 Andersen, T. (2002). Correction of common lead in U–Pb analyses that do not report 204Pb.
743 *Chemical Geology* **192**, 59-79.

744 Barnes, C. G., Werts, K., Memeti, V. & Ardill, K. (2019). Most Granitoid Rocks are Cumulates:
745 Deductions from Hornblende Compositions and Zircon Saturation. *Journal of Petrology* **60**,
746 2227-2240.

747 Barnes, C. G., Werts, K., Memeti, V., Paterson, S. R. & Bremer, R. (2021). A tale of five enclaves:
748 Mineral perspectives on origins of mafic enclaves in the Tuolumne Intrusive Complex.
749 *Geosphere* **17**, 352-374.

750 Bell, E. A., Boehnke, P. & Harrison, T. M. (2016). Recovering the primary geochemistry of Jack
751 Hills zircons through quantitative estimates of chemical alteration. *Geochimica et*
752 *Cosmochimica Acta* **191**, 187-202.

753 Blichert-Toft, J. (2008). The Hf isotopic composition of zircon reference material 91500.
754 *Chemical Geology* **253**, 252-257.

755 Boehnke, P., Watson, E. B., Trail, D., Harrison, T. M. & Schmitt, A. K. (2013). Zircon saturation
756 re-revisited. *Chemical Geology* **351**, 324-334.

757 Bouvier, A., Vervoort, J. D. & Patchett, P. J. (2008). The Lu–Hf and Sm–Nd isotopic composition
758 of CHUR: Constraints from unequilibrated chondrites and implications for the bulk composition
759 of terrestrial planets. *Earth and Planetary Science Letters* **273**, 48-57.

760 Bruand, E., Fowler, M., Storey, C., Laurent, O., Antoine, C., Guitreau, M., Heilimo, E. & Nebel,
761 O. (2020). Accessory mineral constraints on crustal evolution: elemental fingerprints for magma
762 discrimination. *Geochemical Perspectives Letters* **13**, 7-12.

763 Chambers, M., Memeti, V., Eddy, M. P. & Schoene, B. (2020). Half a million years of magmatic
764 history recorded in a K-feldspar megacryst of the Tuolumne Intrusive Complex, California,
765 USA. *Geology* **48**, 400-404.

766 Chu, M.-F., Chung, S.-L., O'Reilly, S. Y., Pearson, N. J., Wu, F.-Y., Li, X.-H., Liu, D., Ji, J., Chu,
767 C.-H. & Lee, H.-Y. (2011). India's hidden inputs to Tibetan orogeny revealed by Hf isotopes of
768 Transhimalayan zircons and host rocks. *Earth and Planetary Science Letters* **307**, 479-486.

769 Claiborne, L. L., Miller, C. F., Gualda, G. A. R., Carley, T. L., Covey, A. K., Wooden, J. L. &
770 Fleming, M. A. (2018). Zircon as Magma Monitor. *Microstructural Geochronology*, 1-33.

771 Claiborne, L. L., Miller, C. F., Walker, B. A., Wooden, J. L., Mazdab, F. K. & Bea, F. (2006).
772 Tracking magmatic processes through Zr/Hf ratios in rocks and Hf and Ti zoning in zircons: An
773 example from the Spirit Mountain batholith, Nevada. *Mineralogical Magazine* **70**, 517-543.

774 Claiborne, L. L., Miller, C. F. & Wooden, J. L. (2010). Trace element composition of igneous
775 zircon: a thermal and compositional record of the accumulation and evolution of a large silicic
776 batholith, Spirit Mountain, Nevada. *Contributions to Mineralogy and Petrology* **160**, 511-531.

777 Clemens, J. D. (2003). S-type granitic magmas—petrogenetic issues, models and evidence. *Earth-*
778 *Science Reviews* **61**, 1-18.

779 Collins, W. J., Huang, H.-Q. & Jiang, X. (2016). Water-fluxed crustal melting produces
780 Cordilleran batholiths. *Geology* **44**, 143-146.

781 Collins, W. J., Murphy, J. B., Johnson, T. E. & Huang, H.-Q. (2020). Critical role of water in the
782 formation of continental crust. *Nature Geoscience* **13**, 331-338.

783 Connolly, J. A. D. (2005). Computation of phase equilibria by linear programming: A tool for
784 geodynamic modeling and its application to subduction zone decarbonation. *Earth and*
785 *Planetary Science Letters* **236**, 524-541.

786 Connolly, J. A. D. & Petrini, K. (2002). An automated strategy for calculation of phase diagram
787 sections and retrieval of rock properties as a function of physical conditions. *Journal of*
788 *Metamorphic Geology* **20**, 697-708.

789 Ferry, J. M. & Watson, E. B. (2007). New thermodynamic models and revised calibrations for the
790 Ti-in-zircon and Zr-in-rutile thermometers. *Contributions to Mineralogy and Petrology* **154**,
791 429-437.

792 Frost, B. R., Barnes, C. G., Collins, W. J., Arculus, R. J., Ellis, D. J. & Frost, C. D. (2001). A
793 geochemical classification for granitic rocks. *Journal of Petrology* **42**, 2033-2048.

794 Fu, B., Page, F. Z., Cavosie, A. J., Fournelle, J., Kita, N. T., Lackey, J. S., Wilde, S. A. & Valley,
795 J. W. (2008). Ti-in-zircon thermometry: applications and limitations. *Contributions to*
796 *Mineralogy and Petrology* **156**, 197-215.

797 Gagnevin, D., Daly, J. S. & Kronz, A. (2010). Zircon texture and chemical composition as a guide
798 to magmatic processes and mixing in a granitic environment and coeval volcanic system.
799 *Contributions to Mineralogy and Petrology* **159**, 579-596.

800 Geisler, T., Schaltegger, U. & Tomaschek, F. (2007). Re-equilibration of zircon in aqueous fluids
801 and melts. *Elements* **3**, 43-50.

802 Griffin, W. L., Pearson, N. J., Belousova, E., Jackson, S. E., van Achterbergh, E., O'Reilly, S. Y.
803 & Shee, S. R. (2000). The Hf isotope composition of cratonic mantle: LAM-MC-ICPMS
804 analysis of zircon megacrysts in kimberlites. *Geochimica et Cosmochimica Acta* **64**, 133-147.

805 Griffin, W. L., Wang, X., Jackson, S. E., Pearson, N. J., O'Reilly, S. Y., Xu, X. & Zhou, X. (2002).
806 Zircon chemistry and magma mixing, SE China: In-situ analysis of Hf isotopes, Tonglu and
807 Pingtan igneous complexes. *Lithos* **61**, 237-269.

808 Harrison, T. M., Watson, E. B. & Aikman, A. B. (2007). Temperature spectra of zircon
809 crystallization in plutonic rocks. *Geology* **35**, 635-638.

810 Hildreth, W. & Moorbath, S. (1988). Crustal contributions to arc magmatism in the Andes of
811 Central Chile. *Contributions to Mineralogy and Petrology* **98**, 455-489.

812 Holland, T. J. B., Green, E. C. R. & Powell, R. (2018). Melting of Peridotites through to Granites:
813 A Simple Thermodynamic Model in the System KNCFMASHTOCr. *Journal of Petrology* **59**,
814 881-900.

815 Hoskin, P. W. O. (2005). Trace-element composition of hydrothermal zircon and the alteration of
816 Hadean zircon from the Jack Hills, Australia. *Geochimica et Cosmochimica Acta* **69**, 637-648.

817 Hoskin, P. W. O. & Schaltegger, U. (2003). The Composition of Zircon and Igneous and
818 Metamorphic Petrogenesis. *Reviews in Mineralogy and Geochemistry* **53**, 27-62.

819 Jagoutz, O. & Klein, B. (2018). On the importance of crystallization-differentiation for the
820 generation of SiO₂-rich melts and the compositional build-up of arc (and
821 continental) crust. *American Journal of Science* **318**, 29-63.

822 Ji, W.-Q., Wu, F.-Y., Chung, S.-L., Li, J.-X. & Liu, C.-Z. (2009). Zircon U–Pb geochronology and
823 Hf isotopic constraints on petrogenesis of the Gangdese batholith, southern Tibet. *Chemical*
824 *Geology* **262**, 229-245.

825 Kapp, P. & DeCelles, P. G. (2019). Mesozoic–Cenozoic geological evolution of the Himalayan-
826 Tibetan orogen and working tectonic hypotheses. *American Journal of Science* **319**, 159-254.

827 Kemp, A. I. S., Hawkesworth, C. J., Foster, G. L., Paterson, B. A., Woodhead, J. D., Hergt, J. M.,
828 Gray, C. M. & Whitehouse, M. J. (2007). Magmatic and Crustal Differentiation History of
829 Granitic Rocks from Hf-O Isotopes in Zircon. *Science* **315**, 980-983.

830 Kirkland, C. L., Yakymchuk, C., Olierook, H. K. H., Hartnady, M. I. H., Gardiner, N. J., Moyen,
831 J.-F., Hugh Smithies, R., Szilas, K. & Johnson, T. E. (2021). Theoretical versus empirical
832 secular change in zircon composition. *Earth and Planetary Science Letters* **554**, 116660.

833 Laurent, O. (2012). Les changements géodynamiques à la transition Archéen-Protérozoïque : étude
834 des granitoïdes de la marge Nord du craton du Kaapvaal (Afrique du Sud). PhD thesis
835 Université Blaise Pascal, Clermont-Ferrand.

Lee, C.-T. A. & Bachmann, O. (2014). How important is the role of crystal fractionation in making intermediate magmas? Insights from Zr and P systematics. *Earth and Planetary Science Letters* **393**, 266-274.

Liu, Y., Hu, Z., Gao, S., Günther, D., Xu, J., Gao, C. & Chen, H. (2008). In situ analysis of major and trace elements of anhydrous minerals by LA-ICP-MS without applying an internal standard. *Chemical Geology* **257**, 34-43.

Liu, Y., Hu, Z., Zong, K., Gao, C., Gao, S., Xu, J. & Chen, H. (2010). Reappraisement and refinement of zircon U-Pb isotope and trace element analyses by LA-ICP-MS. *Chinese Science Bulletin* **55**, 1535-1546.

Ludwig, K. R. (2003). *User's manual for Isoplot 3.00: a geochronological toolkit for Microsoft Excel*. Berkeley.

Ma, L., Wang, Q., Li, Z.-X., Wyman, D. A., Jiang, Z.-Q., Yang, J.-H., Gou, G.-N. & Guo, H.-F. (2013). Early Late Cretaceous (ca. 93Ma) norites and hornblendites in the Milin area, eastern Gangdese: Lithosphere–asthenosphere interaction during slab roll-back and an insight into early Late Cretaceous (ca. 100–80Ma) magmatic "flare-up" in southern Lhasa (Tibet). *Lithos* **172-173**, 17-30.

Miller, C. F., McDowell, S. M. & Mapes, R. W. (2003). Hot and cold granites? Implications of zircon saturation temperatures and preservation of inheritance. *Geology* **31**, 529-532.

Miller, J. S., Matzel, J. E. P., Miller, C. F., Burgess, S. D. & Miller, R. B. (2007). Zircon growth and recycling during the assembly of large, composite arc plutons. *Journal of Volcanology and Geothermal Research* **167**, 282-299.

Morel, M. L. A., Nebel, O., Nebel-Jacobsen, Y. J., Miller, J. S. & Vroon, P. Z. (2008). Hafnium isotope characterization of the GJ-1 zircon reference material by solution and laser-ablation MC-ICPMS. *Chemical Geology* **255**, 231-235.

Moyen, J.-F., Janoušek, V., Laurent, O., Bachmann, O., Jacob, J.-B., Farina, F., Fiannacca, P. & Villaros, A. (2021). Crustal melting vs. fractionation of basaltic magmas: Part 1, The bipolar disorder of granite petrogenetic models. *Lithos*, 106291.

Müntener, O. & Ulmer, P. (2018). Arc crust formation and differentiation constrained by experimental petrology. *American Journal of Science* **318**, 64-89.

Paton, C., Hellstrom, J., Paul, B., Woodhead, J. & Hergt, J. (2011). Iolite: Freeware for the visualisation and processing of mass spectrometric data. *Journal of Analytical Atomic Spectrometry* **26**, 2508-2518.

Reubi, O. & Blundy, J. (2009). A dearth of intermediate melts at subduction zone volcanoes and the petrogenesis of arc andesites. *Nature* **461**, 1269-1273.

Rubatto, D. & Hermann, J. (2007). Experimental zircon/melt and zircon/garnet trace element partitioning and implications for the geochronology of crustal rocks. *Chemical Geology* **241**, 38-61.

Schiller, D. & Finger, F. (2019). Application of Ti-in-zircon thermometry to granite studies: problems and possible solutions. *Contributions to Mineralogy and Petrology* **174**, 51.

Shand, S. J. (1943). *Eruptive Rocks: Their Genesis, Composition, Classification, and Their Relation to Ore-Deposits with a Chapter on Meteorite*. New York: John Wiley & Sons.

Siégel, C., Bryan, S. E., Allen, C. M. & Gust, D. A. (2018). Use and abuse of zircon-based thermometers: A critical review and a recommended approach to identify antecrystic zircons. *Earth-Science Reviews* **176**, 87-116.

Sláma, J., Košler, J., Condon, D. J., Crowley, J. L., Gerdes, A., Hanchar, J. M., Horstwood, M. S. A., Morris, G. A., Nasdala, L., Norberg, N., Schaltegger, U., Schoene, B., Tubrett, M. N. & Whitehouse, M. J. (2008). Plešovice zircon — A new natural reference material for U–Pb and Hf isotopic microanalysis. *Chemical Geology* **249**, 1-35.

884 Söderlund, U., Patchett, P. J., Vervoort, J. D. & Isachsen, C. E. (2004). The 176Lu decay constant
885 determined by Lu–Hf and U–Pb isotope systematics of Precambrian mafic intrusions. *Earth and*
886 *Planetary Science Letters* **219**, 311-324.
887 Sun, S.-s. & McDonough, W. F. (1989). Chemical and isotopic systematics of oceanic basalts:
888 implications for mantle composition and processes. *Geological Society, London, Special*
889 *Publications* **42**, 313-345.
890 Symington, N. J., Weinberg, R. F., Hasalová, P., Wolfram, L. C., Raveggi, M. & Armstrong, R. A.
891 (2014). Multiple intrusions and remelting-remobilization events in a magmatic arc: The St. Peter
892 Suite, South Australia. *Bulletin of the Geological Society of America* **126**, 1200-1218.
893 Troch, J., Ellis, B. S., Schmitt, A. K., Bouvier, A.-S. & Bachmann, O. (2018). The dark side of
894 zircon: textural, age, oxygen isotopic and trace element evidence of fluid saturation in the
895 subvolcanic reservoir of the Island Park-Mount Jackson Rhyolite, Yellowstone (USA).
896 *Contributions to Mineralogy and Petrology* **173**, 54.
897 Wang, R., Richards, J. P., Hou, Z.-q., An, F. & Creaser, R. A. (2015). Zircon U–Pb age and Sr–
898 Nd–Hf–O isotope geochemistry of the Paleocene–Eocene igneous rocks in western Gangdese:
899 Evidence for the timing of Neo-Tethyan slab breakoff. *Lithos* **224-225**, 179-194.
900 Wang, R., Weinberg, R. F., Collins, W. J., Richards, J. P. & Zhu, D.-c. (2018). Origin of
901 postcollisional magmas and formation of porphyry Cu deposits in southern Tibet. *Earth-Science*
902 *Reviews* **181**, 122-143.
903 Watson, E. B. & Harrison, T. M. (1983). Zircon saturation revisited: temperature and composition
904 effects in a variety of crustal magma types. *Earth and Planetary Science Letters* **64**, 295-304.
905 Watson, E. B., Wark, D. A. & Thomas, J. B. (2006). Crystallization thermometers for zircon and
906 rutile. *Contributions to Mineralogy and Petrology* **151**, 413.
907 Weinberg, R. F. & Dunlap, W. J. (2000a). Growth and deformation of the Ladakh batholith,
908 northwest Himalayas: Implications for timing of continental collision and origin of calc-alkaline
909 batholiths. *Journal of Geology* **108**, 303-320.
910 Weinberg, R. F. & Dunlap, W. J. (2000b). Growth and Deformation of the Ladakh Batholith,
911 Northwest Himalayas: Implications for Timing of Continental Collision and Origin of
912 Calc-Alkaline Batholiths. *Journal of Geology* **108**, 303-320.
913 Weinberg, R. F., Vernon, R. & Schmelling, H. (2021). Granitic mushes: their role in magma
914 mixing and assimilation of solids with special focus on enclaves. *Earth-Science Reviews* **220**,
915 103665.
916 White, L. T., Ahmad, T., Ireland, T. R., Lister, G. S. & Forster, M. A. (2011). Deconvolving
917 episodic age spectra from zircons of the Ladakh Batholith, northwest Indian Himalaya.
918 *Chemical Geology* **289**, 179-196.
919 Xu, W., Zhu, D.-C., Wang, Q., Weinberg, R. F., Wang, R., Li, S.-M., Zhang, L.-L. & Zhao, Z.-D.
920 (2021). Cumulate mush hybridization by melt invasion: Evidence from compositionally-diverse
921 amphiboles in ultramafic-mafic arc cumulates within the eastern Gangdese Batholith, southern
922 Tibet. *Journal of Petrology* **61**, ega073.
923 Yin, A. & Harrison, T. M. (2000). Geologic evolution of the Himalayan-Tibetan orogen. *Annual*
924 *Review of Earth and Planetary Sciences*, 211-280.
925 Zhang, L.-L., Zhu, D.-C., Wang, Q., Zhao, Z.-D., Liu, D. & Xie, J.-C. (2019). Late Cretaceous
926 volcanic rocks in the Sangri area, southern Lhasa Terrane, Tibet: Evidence for oceanic ridge
927 subduction. *Lithos* **326-327**, 144-157.
928 Zhang, Z., Ding, H., Palin, R. M., Dong, X., Tian, Z. & Chen, Y. (2020). The lower crust of the
929 Gangdese magmatic arc, southern Tibet, implication for the growth of continental crust.
930 *Gondwana Research* **77**, 136-146.

931 Zhang, Z., Zhao, G., Santosh, M., Wang, J., Dong, X. & Shen, K. (2010). Late Cretaceous
932 charnockite with adakitic affinities from the Gangdese batholith, southeastern Tibet: Evidence
933 for Neo-Tethyan mid-ocean ridge subduction? *Gondwana Research* **17**, 615-631.
934 Zhu, D.-C., Wang, Q., Chung, S.-L., Cawood, P. A. & Zhao, Z.-D. (2019). Gangdese magmatism
935 in southern Tibet and India–Asia convergence since 120 Ma. *Geological Society, London,*
936 *Special Publications* **483**, 583-604.
937 Zhu, D.-C., Wang, Q., Weinberg, R. F., Cawood, P. A., Chung, S.-L., Zheng, Y.-F., Zhao, Z.,
938 Hou, Z.-Q. & Mo, X.-X. (2022). Interplay between oceanic subduction and continental collision
939 in building continental crust. *Nature Communications* **13**, 7141.
940 Zhu, D.-C., Wang, Q., Zhao, Z.-D., Chung, S.-L., Cawood, P. A., Niu, Y., Liu, S.-A., Wu, F.-Y. &
941 Mo, X.-X. (2015). Magmatic record of India-Asia collision. *Scientific Reports* **5**, 14289.
942 Zhu, D.-C., Zhao, Z.-D., Niu, Y., Mo, X.-X., Chung, S.-L., Hou, Z.-Q., Wang, L.-Q. & Wu, F.-Y.
943 (2011). The Lhasa Terrane: Record of a microcontinent and its histories of drift and growth.
944 *Earth and Planetary Science Letters* **301**, 241-255.
945

946 **Figure Captions**

947 Fig. 1. a) Geological map of the Gangdese Batholith linking to the Ladakh Batholith in the west.
948 Small rectangle in the east shows the location of (b). Inset shows the location of (a). b)
949 Geological map of the area surrounding the village of Dabu and the dykes investigated here.
950 BNSZ refers to the Bangong-Nujiang Suture Zone, SNMZ to the Shiquanhe–Nam Tso Mélange
951 Zone, LMF to Luobadui-Milashan Fault, IYZSZ to the Indus-Yarlung Tsangpo Suture Zone,
952 and MBT refers to the Main Boundary Thrust.

953 Fig. 2. Field relationships. a) Diorite dykes cutting through tonalite close to Dabu village. All
954 samples and photographs are from this location. Small black ellipse on lower left indicates a
955 small van for scale. Rectangle on right-hand side marks the position of (b). b) Tip of dykes with
956 variable width and orientation. Vertical scale is ~3m. (c) irregular boundary between dyke and
957 tonalite with back-veining of a finer granitic rock. d) Irregularities at the contact at cm-scale. e)
958 and f) Heterogeneous diorite with irregular veins with sharp to diffuse margins linked to
959 irregular patches with gradational contact with the diorite. These are interpreted to record the
960 nature of mingling and mixing of between granitic and dioritic magmas.

961 Fig. 3. Major element features of the studied samples (Frost *et al.*, 2001). a) FeO/(FeO+MgO) vs
962 SiO2 showing the boundary between ferroan and magnesian plutonic rocks; b) SiO2–MALI
963 (wt.%) binary diagram (MALI = Modified alkali-lime index, Na_2O+K_2O-CaO) from Frost et al.
964 (2001); (c) ASI vs. A/NK diagram [atomic Al/Ca+Na+K vs. Al/Na+K] (Shand, 1943). Tonalites
965 and diorites are magnesian, calc-alkalic and metaluminous to weakly peraluminous.

966 Fig. 4. MORB-normalized (Sun & McDonough, 1989) trace element patterns for the studied
967 samples.

968 Fig. 5. Photomicrographs of diorite samples. a) Sample 18DB01-2 showing euhedral to
969 subhedral biotite in brown tones and hornblende in green tones. Notice apatite needles in
970 plagioclase dominated areas (transparent) (ppl); b) sample 8DB01-2 showing biotite in an
971 equant matrix of twinned plagioclase. Note labelled epidote inclusion in biotite (xpl); c) sample
972 17DB01-2 (ppl); d) sample 18DB01-4 showing anhedral hornblende and subhedral biotite
973 surrounding aggregates of plagioclase (transparent) (ppl). Apatite and epidote grains are
974 indicated. Note absence of pleochroic haloes in biotite in all photomicrographs.

975 Fig. 6. Zircon CL images. Diorite samples 17DB01-2 (a) and 18DB01-2 (b). Zircons have
976 roughly rectangular shapes with two parallel rational faces and two irregular sides. They are
977 generally dark, but some are grey or bright, with either no zoning, irregular zoning or wide

bands. The two samples have contrasting zircon sizes. c) Tonalite sample 18DB01-3 showing representative grains similar to the other two tonalite samples. Zircons are euhedral, bright with well-developed, continuous oscillatory zoning. Some rare grains show a quenched region overprinting the early-formed zoning (left-side of bottom grain). d) Diorite sample 18DB01-4 with two distinct zircon morphological groups: a small group of euhedral zircons labelled xenocrysts, similar to those from the tonalite in (c), and a larger group similar to those from the diorites in (a) and (b). The xenocrysts have ages that coincide with those of the tonalite samples. Green, red and black dashed circles indicate position of analytical spot and colour indicates origin of the zircon: diorite, tonalite and xenocryst in diorite, respectively. Numbers indicate U-Pb age obtained. The scale in (a) applies to all images.

Fig. 7. a) REE plot normalized to chondrite (Sun & McDonough, 1989). Zircons from the tonalitic host define similar patterns to the xenocrysts in the diorite sample 18DB01-4, both dated at between 70 and 80 Ma (see Fig. 11d). Diorite zircon autocrysts have higher values than the tonalite zircons and show a wide variation in LREE values (six orders of magnitude for La) reflecting alteration effects (e.g. Bell *et al.*, 2016). b) Yb/Dy vs Eu/Eu* showing trace element similarity between the xenocryst zircons in diorite and tonalite autocrysts.

Fig. 8. Zircon trace element versus the Light Rare Earth Element Index [LREE-I = (Dy/Nd + Dy/Sm)] (a proxy for zircon alteration Bell *et al.*, 2016) and U content. Diorite zircon analyses are divided into two groups based on CL: types 1-2 clean grey sections of grains and types 3-4 regions dominated by metamictization and CL quenching; see Supplementary Data Electronic Appendix 2). There is considerable overlap between the two groups but types 3-4 have systematically lower LREE-1 and higher contents of all trace elements. In (a) and (b) Fe and Ti define negative trends with LREE-1 (in these figures, types 3-4 symbols were placed in front of types 1-2 for better visualization of the link between zircons deemed altered and LREE-I values. Types 3-4 zircon analyses concentrate, as expected, in the lower end of LREE-1, indicative of alteration, but reach values of 100, considerably higher than the cutoff value of 30 for alteration of Bell et al. (2016). Up to 100, types 3-4 overlap with types 1-2, and these can have very high contents of Ti. In (c) to (h), Fe, Ca, Th, Y reach values close to 10,000 ppm or 1 wt.%, defining positive trends with U, which reaches up to 9000 ppm. Titanium also defines a positive trend with U, with numerous analyses above 30 ppm, some reaching a few 100 ppm. The trend defined by Hf and Ti in diorite zircons are the opposite to those found for granitic rocks by Claiborne et al. (2010) shown by the grey fields, and similar to the high-U zircons in Fig. 6 in Troch et al. (2018). In (c) to (h), types 3-4 zircon symbols were placed behind types 1-2. For

tonalite zircons, the trends are similar to those in Claiborne et al. (2010). Tonalite zircons and xenocrysts in diorite sample 18DB01-4 are not differentiated and overlap in the plots. All plots are log-log scale.

Fig. 9. (a-d) Binary plots of typically incompatible elements versus Ti in zircon. For tonalite samples Hf behaves incompatibly defining negative, but all other elements define a curved shape changing from a positive (compatible) to a negative (incompatible) trend as Ti increases. This is not the case for the diorite sample for which U, Th, and Yb, define only positive or compatible trends with Ti, and only Hf defines a negative (incompatible) trend. The compatible trends are surprising and contrast with the incompatible trends found by Claiborne et al (2010) indicated by grey fields. Ti-values higher than 40 ppm were not plotted as they correspond to unrealistically high T and therefore probably correspond to altered zircons. Grey empty symbols indicate analyses with anomalous peaks or plateaus of Fe and Ca, key indicators of metamictization and zircon re-equilibration (see section 9.2 for discussion). All plots are log-log scale and symbols are as in legend for Fig. 8.

Fig. 10. Concordia diagrams for zircon analyses from diorite samples. a-c) Diorite dyke samples 17DB01-2, 18DB01-2 and 18DB01-4 with ages centred around 46 to 47 Ma. Samples 18DB01-2 and 18DB01-4 also contained 70-80 Ma xenocrysts shown in Fig. 11. d) Comparison between ages of zircon analyses from diorite sample 18DB01-4 as a function of CL type shows no systematic shift between CL types 1-2, and the quenched CL types 3-4 despite the anomalously high values of Th+U and other trace elements in the latter (Fig. 8). All ellipses in (a-c) and bars in (d) mark the 2σ confidence level. A number of analyses have been excluded: 2 of 74 analyses for 17DB01-2 (1 with large error, 1 with fluctuating age signals), 18 out of 75 for 18DB01-2 (16 discordant and 2 outliers), 25 out of 111 for 18DB01-4 (23 discordant, 1 outlier and 1 with large error). A small number of outlier dates were removed from the calculation of the mean age by Isoplot: 2 out of 72 for sample 17DB01-2, 2 out of 57 for sample 18DB01-2, 4 out of 86 for sample 18DB01-4. In (d), analyses in light grey at the high-end of values, have been dates removed from the calculation of the mean age.

Fig. 11. Concordia diagrams for zircon analyses from tonalite samples and xenocrysts in diorite samples. a-c) Tonalite samples 17DB01-1, 18DB01-1, 18DB01-3 showing ages centred between 77 and 79 Ma and lacking older xenocrysts. d) and e) Xenocrysts from diorite dyke sample 18DB01-4 and 18DB01-2. The spread of dates in (d) and (e) imply that the mean ages are not meaningful with MSWD>10. All ellipses mark the 2σ confidence level. A small number of analyses have been excluded from the diagrams: 1 of 18 analyses for sample 17DB01-1 (>10%

discordant), 5 of 68 for 18DB01-1 (2 discordant and 3 outlier), and 3 of 19 for 18DB01-4 (2 with very large errors and 1 outlier). A small number of outliers were removed from the calculation of the mean age by Isoplot: 4 out of 63 for sample 18DB01-1, and 2 out of 18 for sample 18DB01-3.

Fig. 12. $^{206}Pb/^{238}U$ ages for zircons from diorites show no systematic trend with Th+U content. Symbols as in legend for Fig. 8 where empty symbols are types 3-4.

Fig. 13. $\varepsilon_{Hf(t)}$ values for all six samples plotted against zircon U-Pb age. The ~77-79 Ma tonalite zircons have $\varepsilon_{Hf(t)}$ centred around +9 ± 1, whereas the ~46-47 Ma diorite analyses are more spread between +6 and +11. N=344 analyses, with 78 from tonalite zircons and 266 from diorite.

Fig. 14. Model of crystallization for a diorite melt with 73 ppm Zr and a tonalite melt with 144 ppm Zr. H_2O contents for the diorite of 3 wt.% H_2O (left column), and 6 wt.% H_2O (middle column) are shown. Tonalite melt contains 2 wt.% H_2O. Low H_2O content was assumed in order to investigate its remelting by H_2O derived from the diorite intrusion. a) Minerals and melt/H_2O proportions. Diorite solidus T (T_{sol}) is 677 ^oC, and 650 ^oC for the tonalite. The two diorite models show nearly 70 ^oC difference water saturation T. Sphene, spinel and ilmenite form in diorite and tonalite not shown because of low proportions. b) Melt fraction. For all three cases the last ~20% crystallizes within 10 ^oC of the solidus. c) Zr content in melt. Values increase until the curve intersects the zircon saturation curves calculated using M-values in (d) and calibrations in Boehnke et al. (2013) and Watson and Harrison (1983). Zircon saturation for the diorites is reached at 714 and 711 ^oC, for 3 and 6 wt.% H_2O, respectively, where ~23% melt (for 3% H_2O) or ~ 26% melt (for 6% H_2O) remain. Tonalite reaches ~ 20% melt at ~650 ^oC solidus, where ~ 90% of the zircons are stable. d) M-value of residual melt used to determine the zircon saturation curve in (c). M-value for diorites steadily decrease to reach a value of 1.4 close to the solidus. For the tonalite M first decreases from a value of 1.45 at the liquidus (not shown) and then increases to ~1.4 at the solidus, due to stabilization of Bt and Qtz. e) $a(SiO_2)$ and $a(TiO_2)$. f) Ti-in-zircon calculated using curves in (e) (solid lines) or assuming a fixed value of $a(SiO_2)=1$ and $a(TiO_2)=0.7$ (dashed lines; similar to Claiborne et al. (2010)). The differences between the two curves are small. Calculations use Ferry and Watson (2007). g) Zr content in melt, non-zircon phases and zircon as a function of temperature (note different scale in x-axis). Zircons are saturated close to the solidus for diorite. Diorite composition is similar to the basalt modelled by

Lee and Bachmann (2014) (their Fig. 2b), but despite higher Zr in our starting composition, melt never reaches the > 300 ppm Zr in their model, peaking instead at ~ 150 ppm, due to significant intake of Zr in non-zircon minerals excluded in their model.

Fig. 15. Comparison of signal outputs from zircon analyses for sample 18DB01-4: a) spot 1-04 in a type 1 zircon, and b) spot 2-41 in a type 2 zircon. Data from (b) was excluded from consideration because of anomalous plateaus of Fe, Ca, Ti, and a sudden drop in Th, U counts.

Fig. 16. Zircon chemistry modelling. a) Modelled zircon Th vs Ti composition for the diorite and tonalite (thick black lines) compared with data for zircons from diorite dykes, xenocrystic zircons in diorite and tonalite host rock zircons; b) same for Nd vs Ti. Analysed zircon grains are colour coded according to "reliability": if the zircon analysis has anomalous Fe or Ca signal it is deemed unreliable, if it has anomalous peaks or plateaus of Y, Th, Ti or HREE it is deemed dubious, otherwise it is classified as magmatic. Models are calculated as discussed in the text and uses Boehnke et al.'s (2013) model for saturation, but the results are very similar using Watson & Harrison (1983). For comparison (a) shows the approximate slope of the trend (thick grey arrow) defined by the data for granitic rocks in Claiborne et al. (2006), which is similar to the modelled slope for the tonalite (thick dashed line). The yellow band in (b) defines the field generated by mixing a zircon composition with 3 ppm Ti and 1 ppm Nd, with titanite with 24.4 % Ti and between 1000 and 10000 ppm Nd (Bruand *et al.*, 2020). The band indicates that mixing with titanite is unlikely to explain the trend because it causes a stronger enrichment in Ti compared to Nd.

Fig. 17. Assimilation of host rock through anatexis, back-veining and mixing with zircon transfer. a) Original dioritic magma intrusion at temperatures above zircon saturation. As magma flows and cools, it heats-up the surrounding and releases H_2O. b) The tonalite melts at relatively low temperatures lacking anhydrous peritectic minerals. Granitic dykelets derived from tonalite anatexis back-veins the diorite that is now a cool zircon-saturated mush. The mush deforms in a ductile fashion and granitic melt flow through the pore space of the mush (inset) transferring tonalite zircons and hybridizing the diorite. Zircon xenocrysts are preserved in the zircon-saturated diorite. Size of zircons is exaggerated.

Table 1. Major element composition of the tonalite and diorite samples.

No.	Label	Lithology	[SiO_2]	[TiO_2]	[Al_2O_3]	[TFe_2O_3]	[MnO]	[MgO]	[CaO]	[Na_2O]	[K_2O]
1	17DB01-2	diorite	57.76	0.69	17.98	7.04	0.14	3.66	6.65	3.98	1.85
2	18DB01-2	diorite	58.45	0.49	18.86	6.40	0.09	2.66	6.95	4.54	1.20
3	18DB01-4	diorite	54.06	0.73	18.29	8.67	0.17	4.68	7.60	3.83	1.72
4	17DB01-1	tonalite	69.91	0.24	16.24	2.30	0.07	0.58	2.91	4.37	3.28
5	18DB01-1	tonalite	68.42	0.26	16.85	2.56	0.07	0.64	2.92	4.35	3.81
6	18DB01-3	tonalite	68.96	0.29	16.96	2.80	0.05	0.74	3.43	4.56	2.08
	average tonalite		69.10	0.26	16.68	2.55	0.06	0.65	3.08	4.43	3.06

[P_2O_5]	Mg#	A/CNK	K_2O/Na_2O	Zr
0.25	51	0.87	0.46	73.2
0.36	45	0.88	0.26	102
0.26	52	0.83	0.45	74.1
0.10	33	1.01	0.75	132
0.12	33	1.01	0.88	134
0.14	35	1.06	0.46	163
0.12	34	1.03	0.69	143

A complete list of trace elements and repeat analyses are listed in Supplementary Data Electronic Appendix 4. Zr contents in the repeat vary typically by 2 to 10 ppm, except for sample 17DB01-1 for which the repeat yielded 114 ppm instead of 132 ppm. The results are normalized to anhydrous values (LOI-free). Values in the Supplementary Data Electronic Appendix 4 are not normalized and include the LOI values that vary from 0.2 to 0.7% for the tonalites and 0.4 to 0.9% for the diorites. Tonalite average corresponds to the composition used in the model calculations. Mg# = [MgO/(MgO+FeO) x 100], A/CNK = molar ratio $Al_2O_3/ (CaO+Na_2O+K_2O)$.

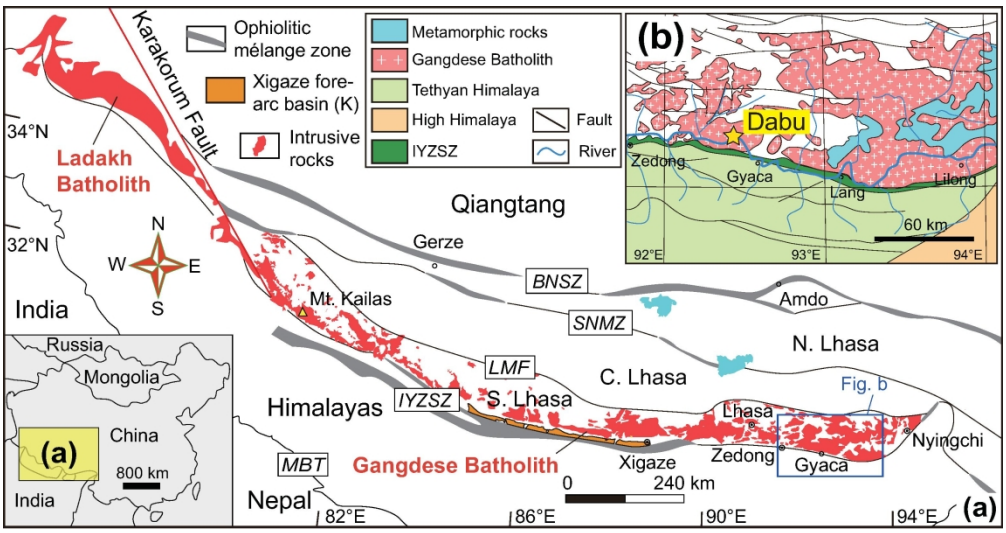

Fig. 1. a) Geological map of the Gangdese Batholith linking to the Ladakh Batholith in the west. Small rectangle in the east shows the location of (b). Inset shows the location of (a). b) Geological map of the area surrounding the village of Dabu and the dykes investigated here. BNSZ refers to the Bangong-Nujiang Suture Zone, SNMZ to the Shiquanhe–Nam Tso Mélange Zone, LMF to Luobadui-Milashan Fault, IYZSZ to the Indus-Yarlung Tsangpo Suture Zone, and MBT refers to the Main Boundary Thrust.

131x68mm (600 x 600 DPI)

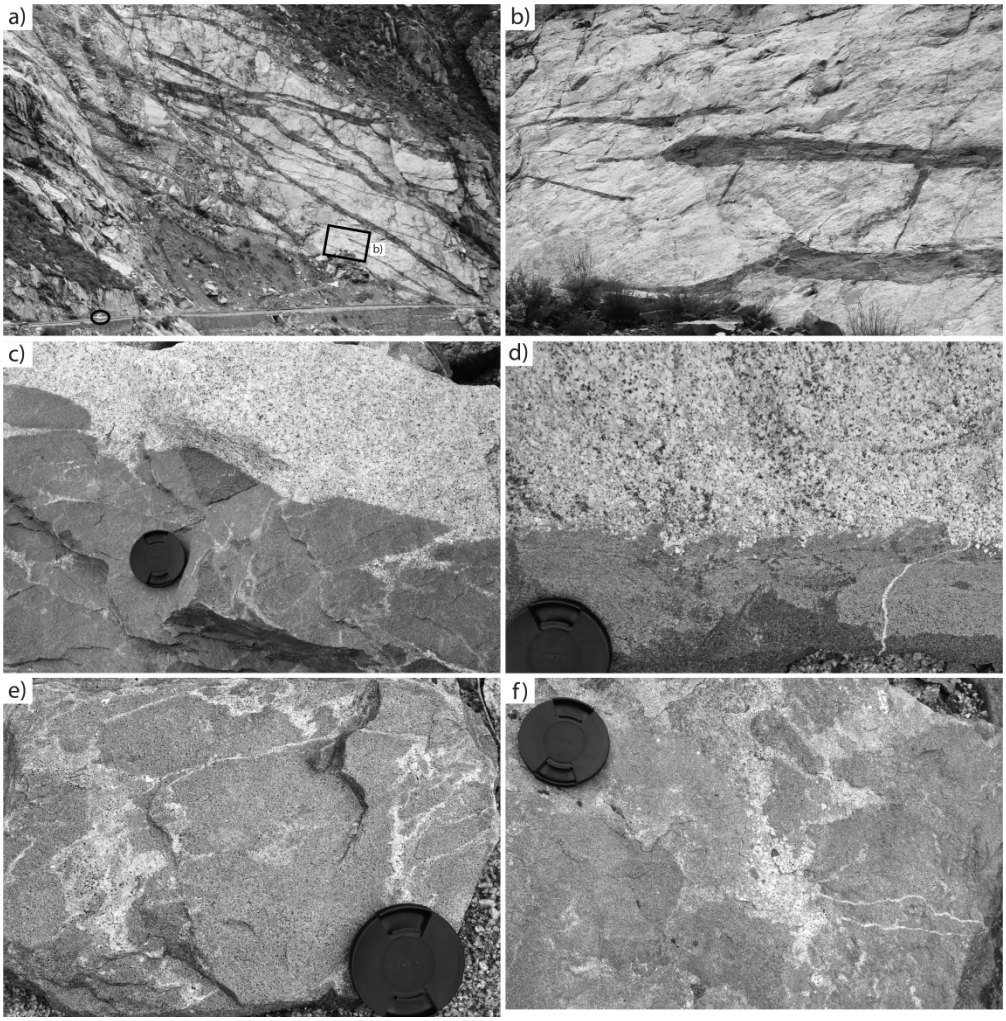

Fig. 2. Field relationships. a) Diorite dykes cutting through tonalite close to Dabu village. All samples and photographs are from this location. Small black ellipse on lower left indicates a small van for scale. Rectangle on right-hand side marks the position of (b). b) Tip of dykes with variable width and orientation. Vertical scale is ~3m. (c) irregular boundary between dyke and tonalite with back-veining of a finer granitic rock. d) Irregularities at the contact at cm-scale. e) and f) Heterogeneous diorite with irregular veins with sharp to diffuse margins linked to irregular patches with gradational contact with the diorite. These are interpreted to record the nature of mingling and mixing of between granitic and dioritic magmas.

402x407mm (300 x 300 DPI)

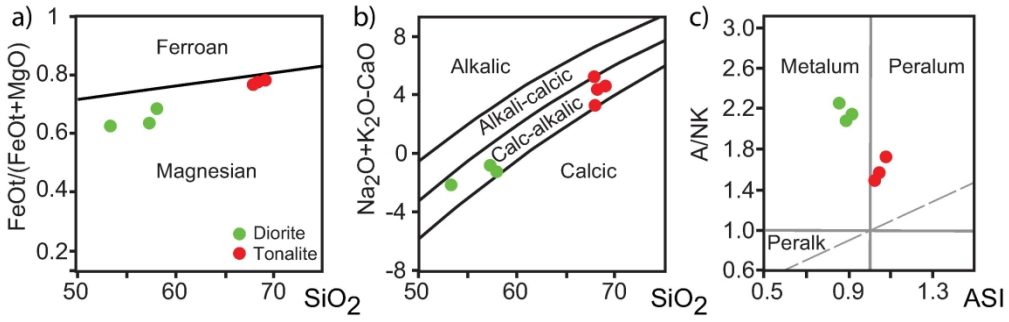

Fig. 3. Major element features of the studied samples (Frost et al., 2001). a) FeO/(FeO+MgO) vs SiO_2 showing the boundary between ferroan and magnesian plutonic rocks; b) SiO_2–MALI (wt.%) binary diagram (MALI = Modified alkali-lime index, Na_2O+K_2O-CaO) from Frost et al. (2001); (c) ASI vs. A/NK diagram [atomic Al/Ca+Na+K vs. Al/Na+K] (Shand, 1943). Tonalites and diorites are magnesian, calc-alkalic and metaluminous to weakly peraluminous.

136x43mm (600 x 600 DPI)

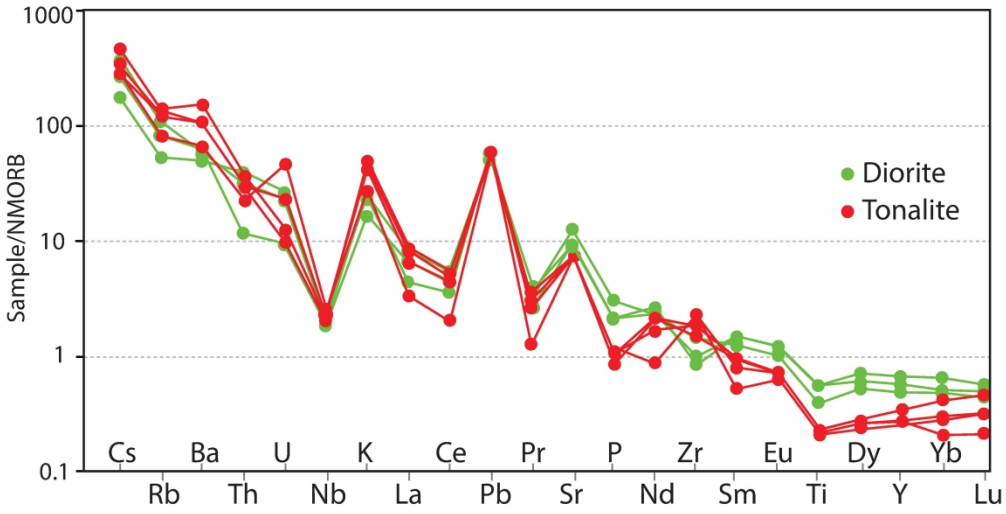

Fig. 4. MORB-normalized (Sun & McDonough, 1989) trace element patterns for the studied samples.

167x85mm (600 x 600 DPI)

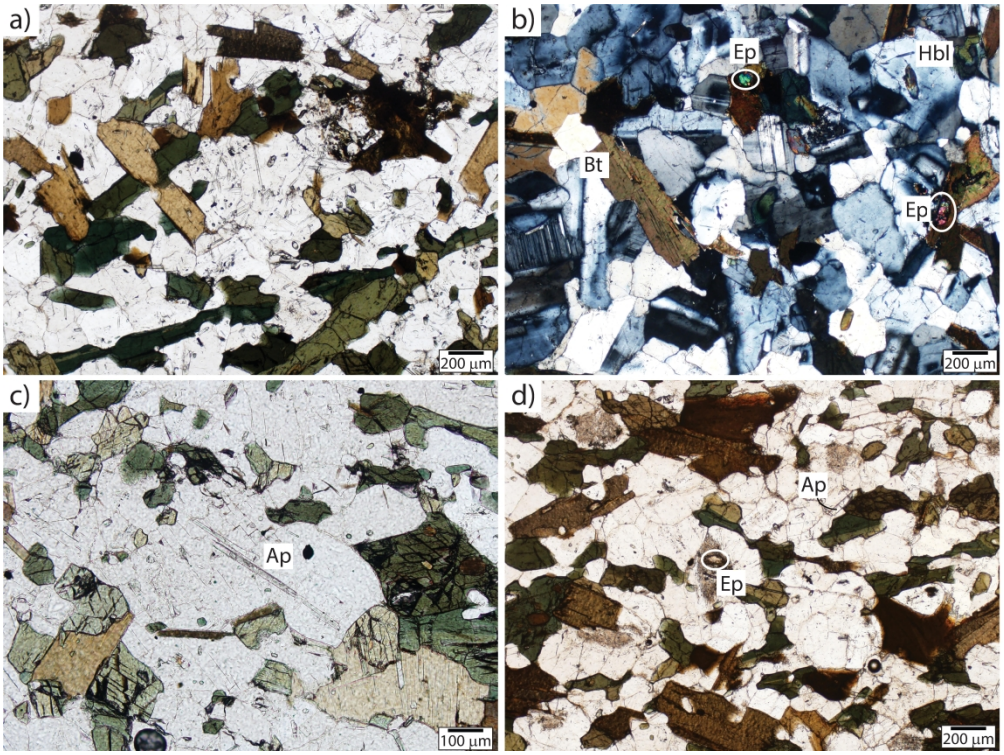

Fig. 5. Photomicrographs of diorite samples. a) Sample 18DB01-2 showing euhedral to subhedral biotite in brown tones and hornblende in green tones. Notice apatite needles in plagioclase dominated areas (transparent) (ppl); b) sample 8DB01-2 showing biotite in an equant matrix of twinned plagioclase. Note labelled epidote inclusion in biotite (xpl); c) sample 17DB01-2 (ppl); d) sample 18DB01-4 showing anhedral hornblende and subhedral biotite surrounding aggregates of plagioclase (transparent) (ppl). Apatite and epidote grains are indicated. Note absence of pleochroic haloes in biotite in all photomicrographs.

323x241mm (600 x 600 DPI)

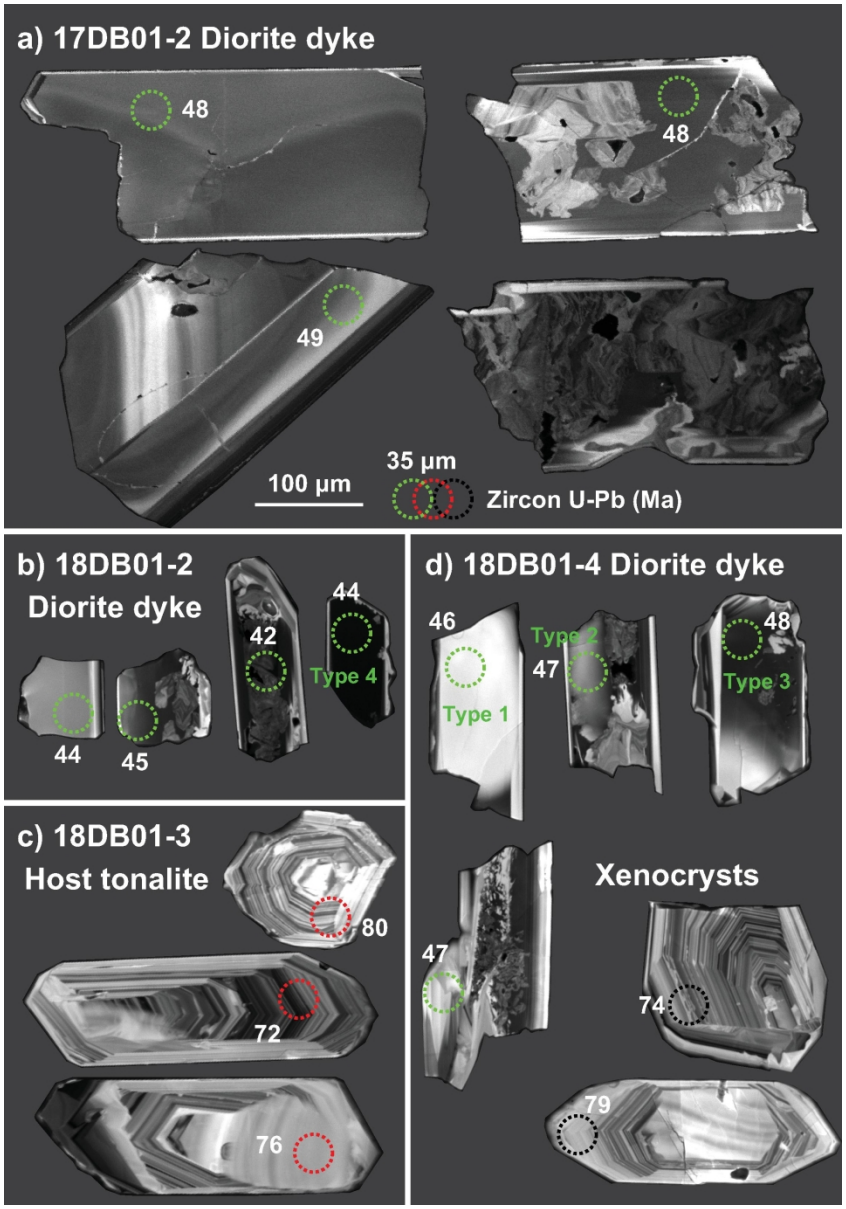

Fig. 6. Zircon CL images. Diorite samples 17DB01-2 (a) and 18DB01-2 (b). Zircons have roughly rectangular shapes with two parallel rational faces and two irregular sides. They are generally dark, but some are grey or bright, with either no zoning, irregular zoning or wide bands. The two samples have contrasting zircon sizes. c) Tonalite sample 18DB01-3 showing representative grains similar to the other two tonalite samples. Zircons are euhedral, bright with well-developed, continuous oscillatory zoning. Some rare grains show a quenched region overprinting the early-formed zoning (left-side of bottom grain). d) Diorite sample 18DB01-4 with two distinct zircon morphological groups: a small group of euhedral zircons labelled xenocrysts, similar to those from the tonalite in (c), and a larger group similar to those from the diorites in (a) and (b). The xenocrysts have ages that coincide with those of the tonalite samples. Green, red and black dashed circles indicate position of analytical spot and colour indicates origin of the zircon: diorite, tonalite and xenocryst in diorite, respectively. Numbers indicate U-Pb age obtained. The scale in (a) applies to all images.

96x138mm (600 x 600 DPI)

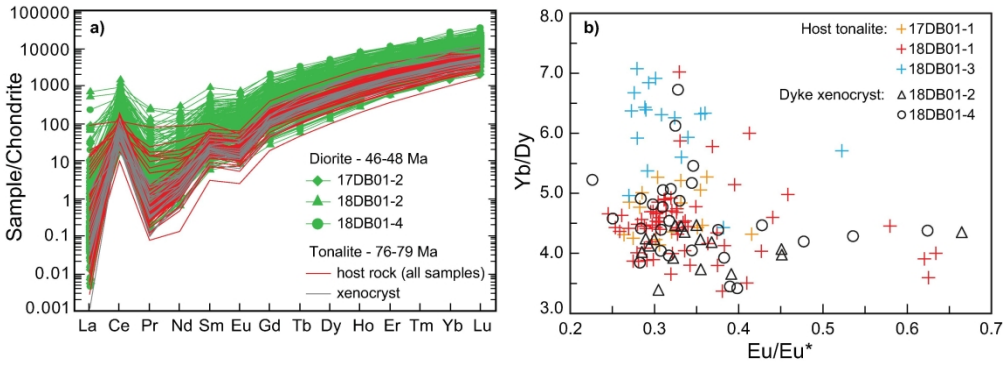

Fig. 7. a) REE plot normalized to chondrite (Sun & McDonough, 1989). Zircons from the tonalitic host define similar patterns to the xenocrysts in the diorite sample 18DB01-4, both dated at between 70 and 80 Ma (see Fig. 11d). Diorite zircon autocrysts have higher values than the tonalite zircons and show a wide variation in LREE values (six orders of magnitude for La) reflecting alteration effects (e.g. Bell et al., 2016). b) Yb/Dy vs Eu/Eu* showing trace element similarity between the xenocryst zircons in diorite and tonalite autocrysts.

166x60mm (600 x 600 DPI)

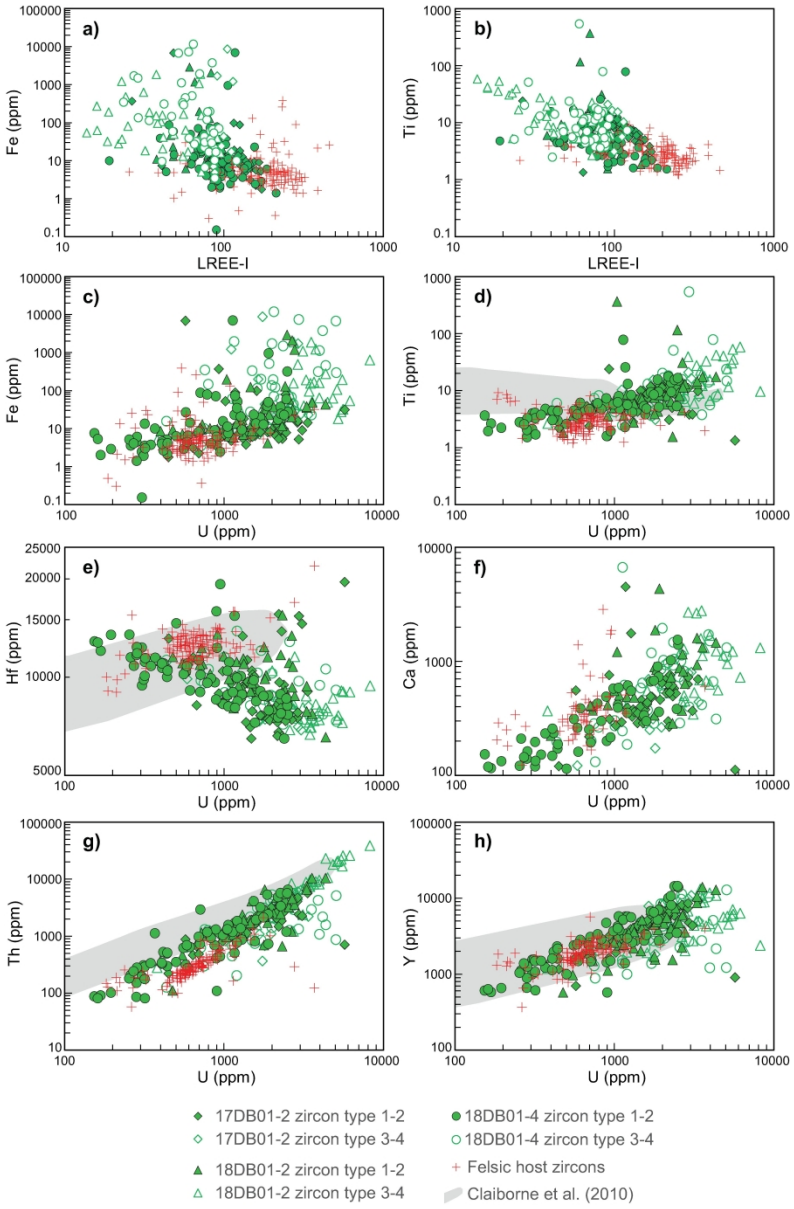

Fig. 8. Zircon trace element versus the Light Rare Earth Element Index [LREE-I = (Dy/Nd + Dy/Sm)] (a proxy for zircon alteration Bell et al., 2016) and U content. Diorite zircon analyses are divided into two groups based on CL: types 1-2 clean grey sections of grains and types 3-4 regions dominated by metamictization and CL quenching; see Supplementary Data Electronic Appendix 2). There is considerable overlap between the two groups but types 3-4 have systematically lower LREE-1 and higher contents of all trace elements. In (a) and (b) Fe and Ti define negative trends with LREE-1 (in these figures, types 3-4 symbols were placed in front of types 1-2 for better visualization of the link between zircons deemed altered and LREE-I values. Types 3-4 zircon analyses concentrate, as expected, in the lower end of LREE-1, indicative of alteration, but reach values of 100, considerably higher than the cutoff value of 30 for alteration of Bell et al. (2016). Up to 100, types 3-4 overlap with types 1-2, and these can have very high contents of Ti. In (c) to (h), Fe, Ca, Th, Y reach values close to 10,000 ppm or 1 wt.%, defining positive trends with U, which reaches up to 9000 ppm. Titanium also defines a positive trend with U, with numerous analyses above 30 ppm, some reaching a few 100 ppm. The trend defined by Hf and Ti in diorite zircons are the opposite to those found for granitic rocks by Claiborne et al. (2010) shown by the grey fields, and

similar to the high-U zircons in Fig. 6 in Troch et al. (2018). In (c) to (h), types 3-4 zircon symbols were placed behind types 1-2. For tonalite zircons, the trends are similar to those in Claiborne et al. (2010). Tonalite zircons and xenocrysts in diorite sample 18DB01-4 are not differentiated and overlap in the plots. All plots are log-log scale.

172x263mm (600 x 600 DPI)

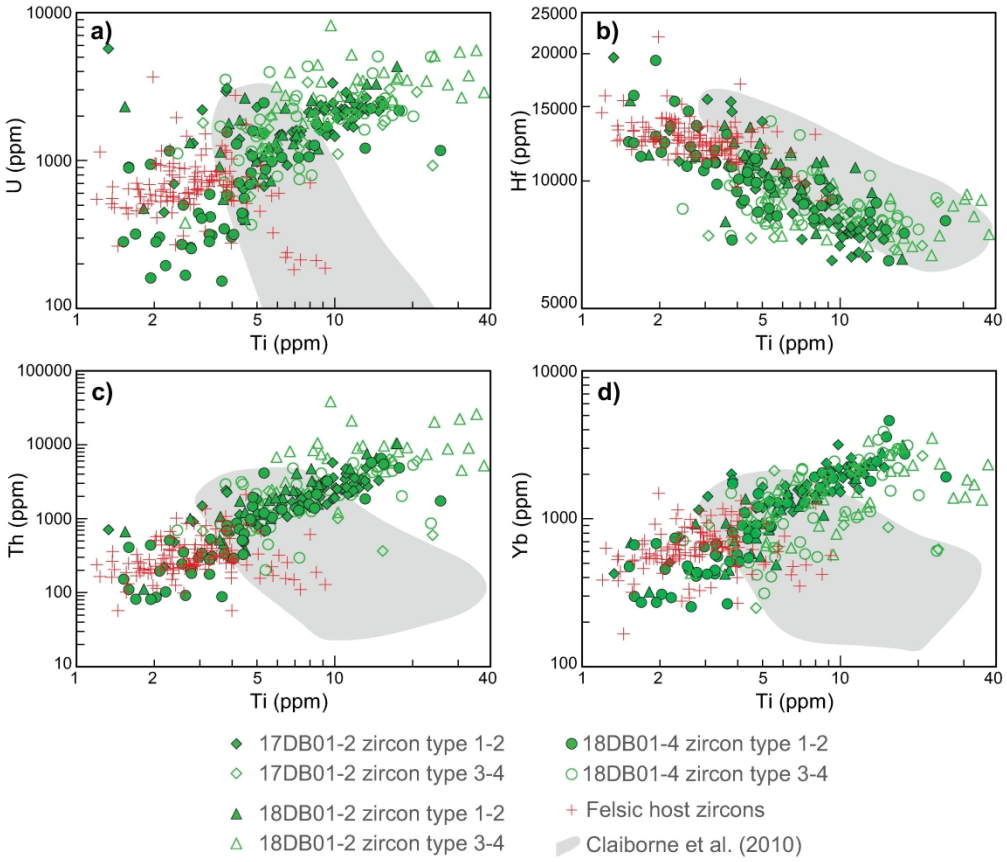

Fig. 9. (a-d) Binary plots of typically incompatible elements versus Ti in zircon. For tonalite samples Hf behaves incompatibly defining negative, but all other elements define a curved shape changing from a positive (compatible) to a negative (incompatible) trend as Ti increases. This is not the case for the diorite sample for which U, Th, and Yb, define only positive or compatible trends with Ti, and only Hf defines a negative (incompatible) trend. The compatible trends are surprising and contrast with the incompatible trends found by Claiborne et al (2010) indicated by grey fields. Ti-values higher than 40 ppm were not plotted as they correspond to unrealistically high T and therefore probably correspond to altered zircons. Grey empty symbols indicate analyses with anomalous peaks or plateaus of Fe and Ca, key indicators of metamictization and zircon re-equilibration (see section 9.2 for discussion). All plots are log-log scale and symbols are as in legend for Fig. 8.

169x144mm (600 x 600 DPI)

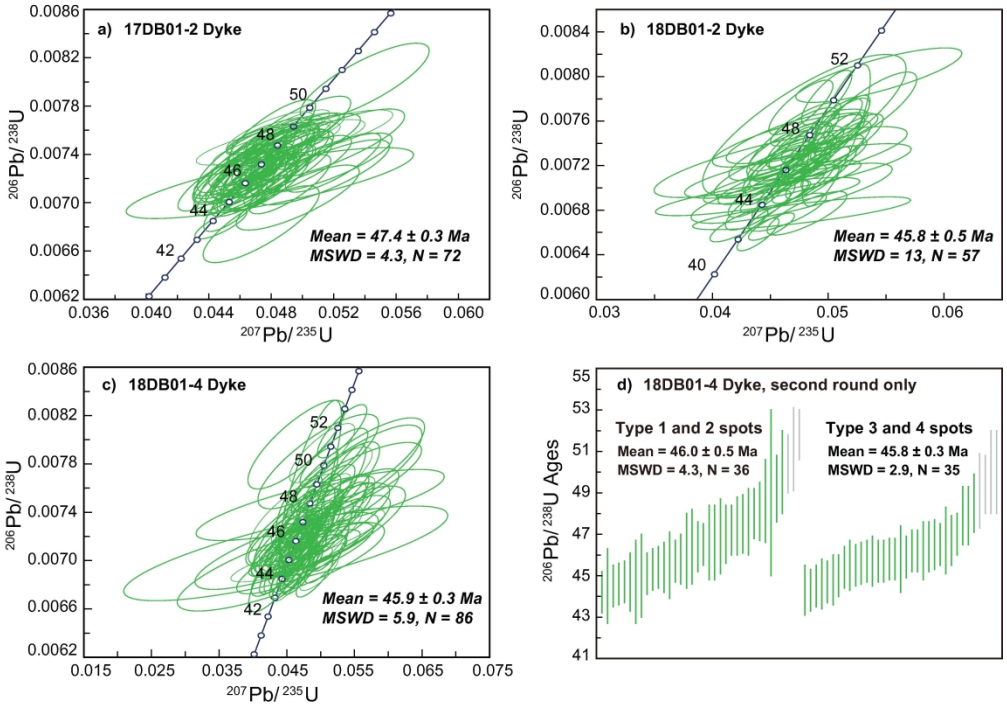

Fig. 10. Concordia diagrams for zircon analyses from diorite samples. a-c) Diorite dyke samples 17DB01-2, 18DB01-2 and 18DB01-4 with ages centred around 46 to 47 Ma. Samples 18DB01-2 and 18DB01-4 also contained 70-80 Ma xenocrysts shown in Fig. 11. d) Comparison between ages of zircon analyses from diorite sample 18DB01-4 as a function of CL type shows no systematic shift between CL types 1-2, and the quenched CL types 3-4 despite the anomalously high values of Th+U and other trace elements in the latter (Fig. 8). All ellipses in (a-c) and bars in (d) mark the 2σ confidence level. A number of analyses have been excluded: 2 of 74 analyses for 17DB01-2 (1 with large error, 1 with fluctuating age signals), 18 out of 75 for 18DB01-2 (16 discordant and 2 outliers), 25 out of 111 for 18DB01-4 (23 discordant, 1 outlier and 1 with large error). A small number of outlier dates were removed from the calculation of the mean age by Isoplot: 2 out of 72 for sample 17DB01-2, 2 out of 57 for sample 18DB01-2, 4 out of 86 for sample 18DB01-4. In (d), analyses in light grey at the high-end of values, have been dates removed from the calculation of the mean age.

172x123mm (600 x 600 DPI)

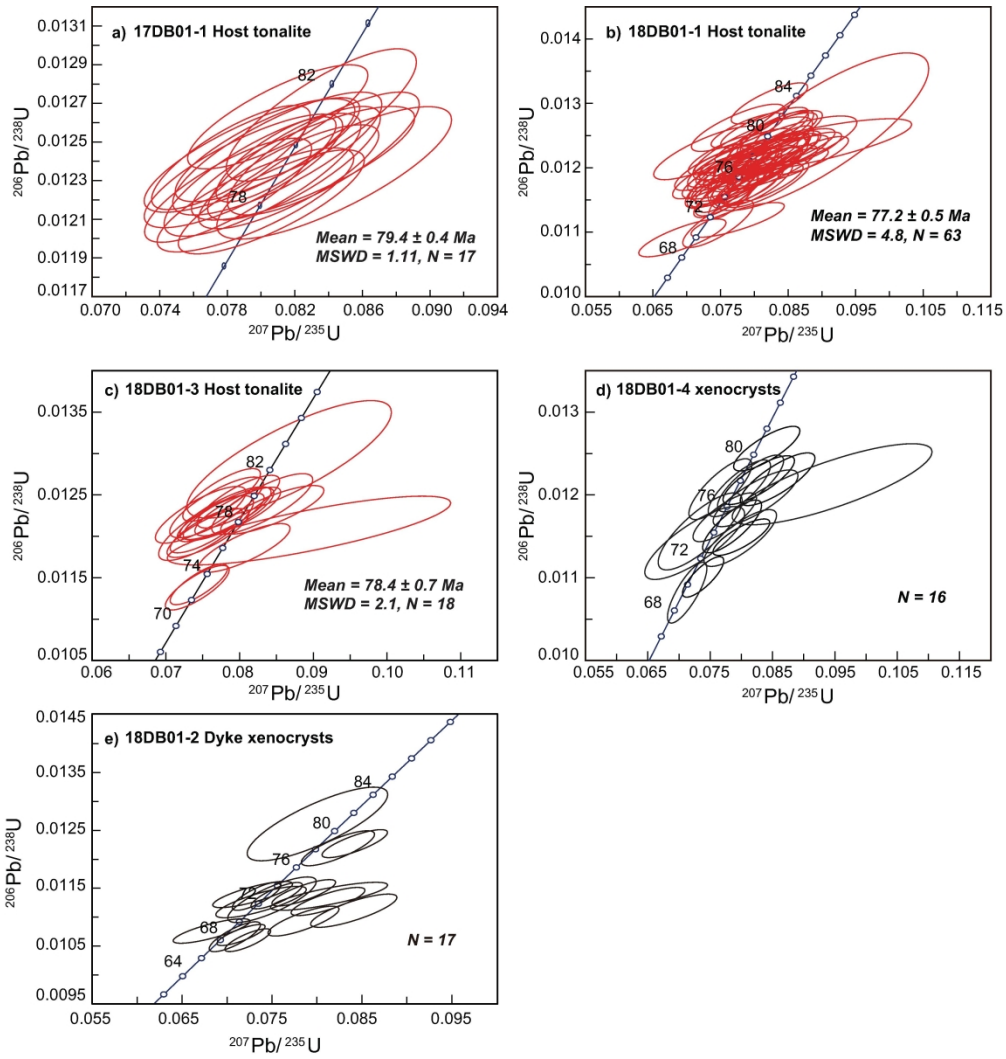

Fig. 11. Concordia diagrams for zircon analyses from tonalite samples and xenocrysts in diorite samples. a-c) Tonalite samples 17DB01-1, 18DB01-1, 18DB01-3 showing ages centred between 77 and 79 Ma and lacking older xenocrysts. d) and e) Xenocrysts from diorite dyke sample 18DB01-4 and 18DB01-2. The spread of dates in (d) and (e) imply that the mean ages are not meaningful with MSWD>10. All ellipses mark the 2σ confidence level. A small number of analyses have been excluded from the diagrams: 1 of 18 analyses for sample 17DB01-1 (>10% discordant), 5 of 68 for 18DB01-1 (2 discordant and 3 outlier), and 3 of 19 for 18DB01-4 (2 with very large errors and 1 outlier). A small number of outliers were removed from the calculation of the mean age by Isoplot: 4 out of 63 for sample 18DB01-1, and 2 out of 18 for sample 18DB01-3.

172x181mm (600 x 600 DPI)

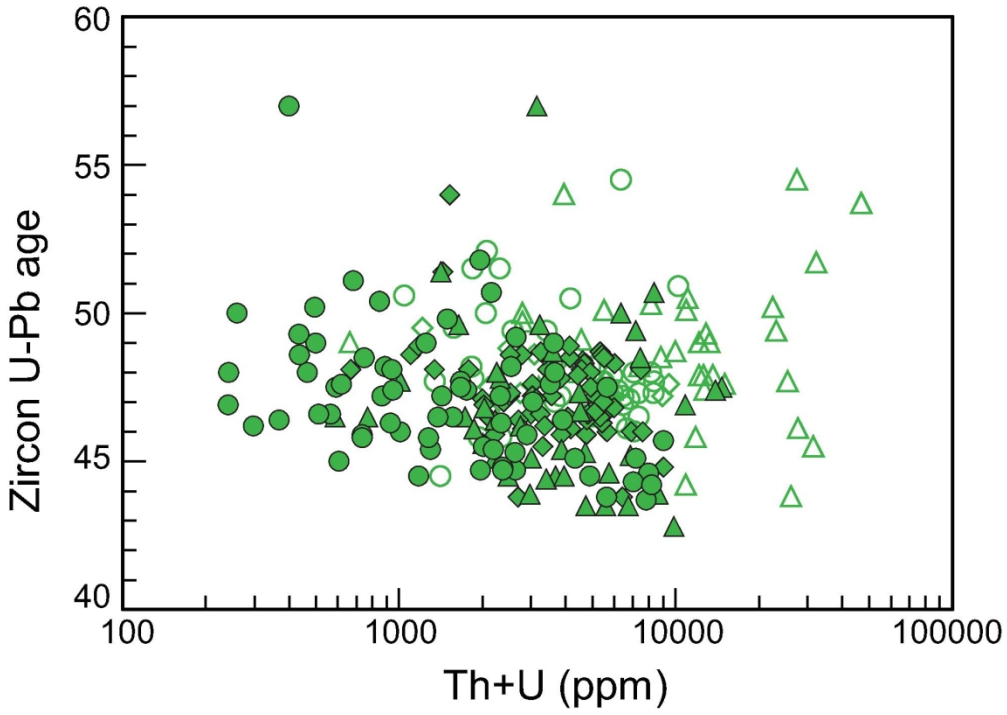

Fig. 12. 206Pb/238U ages for zircons from diorites show no systematic trend with Th+U content. Symbols as in legend for Fig. 8 where empty symbols are types 3-4.

84x59mm (600 x 600 DPI)

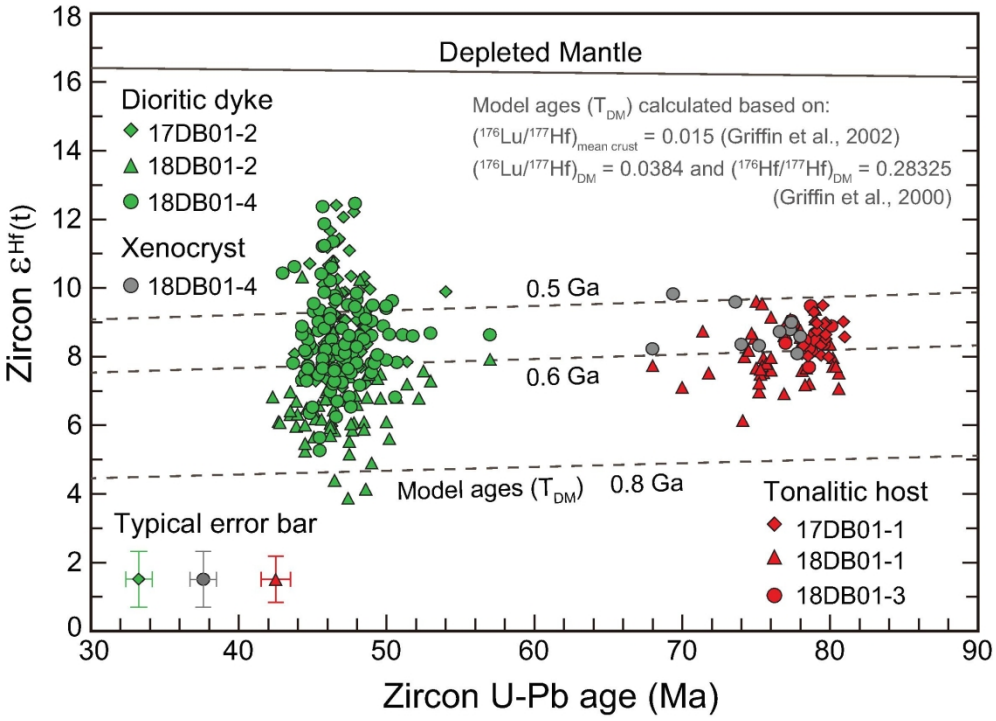

Fig. 13. εHf(t) values for all six samples plotted against zircon U-Pb age. The ~77-79 Ma tonalite zircons have εHf(t) centred around +9 ± 1, whereas the ~46-47 Ma diorite analyses are more spread between +6 and +11. N=344 analyses, with 78 from tonalite zircons and 266 from diorite.

100x72mm (600 x 600 DPI)

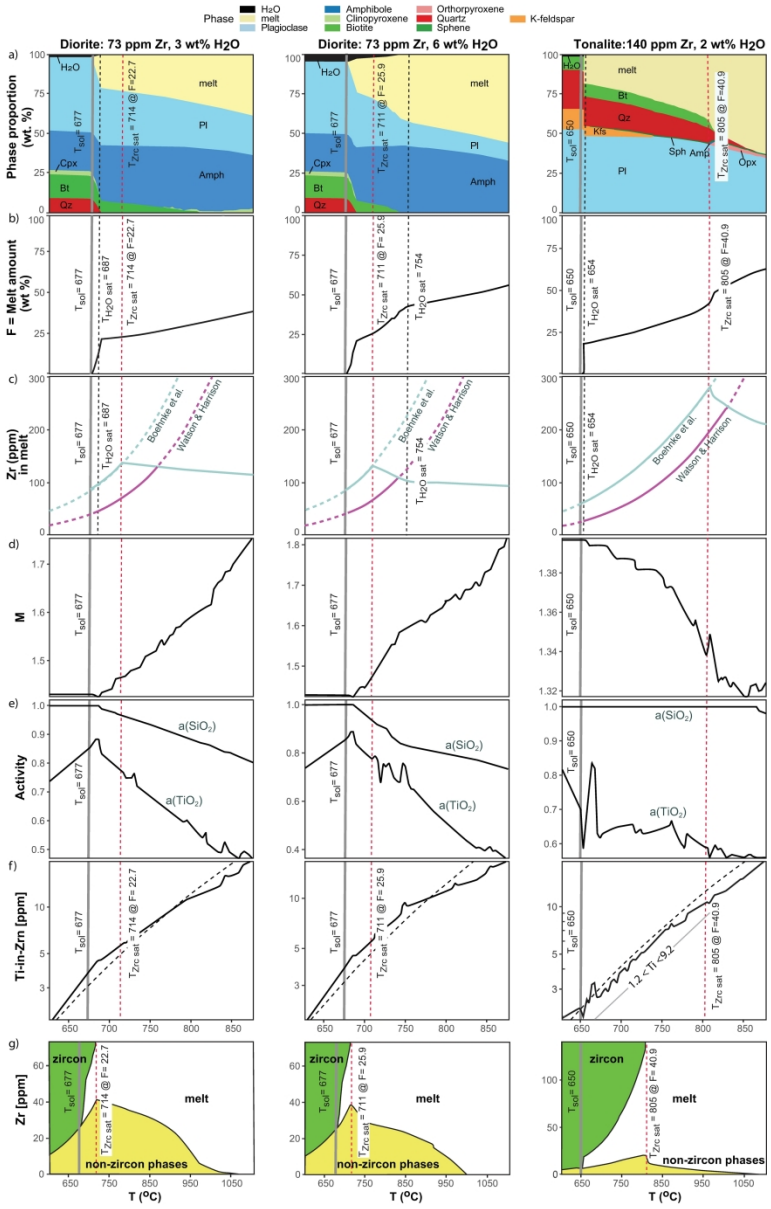

Fig. 14. Model of crystallization for a diorite melt with 73 ppm Zr and a tonalite melt with 144 ppm Zr. H2O contents for the diorite of 3 wt.% H2O (left column), and 6 wt.% H2O (middle column) are shown. Tonalite melt contains 2 wt.% H2O. Low H2O content was assumed in order to investigate its remelting by H2O derived from the diorite intrusion. a) Minerals and melt/H2O proportions. Diorite solidus T (Tsol) is 677 oC, and 650 oC for the tonalite. The two diorite models show nearly 70 oC difference water saturation T. Sphene, spinel and ilmenite form in diorite and tonalite not shown because of low proportions. b) Melt fraction. For all three cases the last ~20% crystallizes within 10 oC of the solidus. c) Zr content in melt. Values increase until the curve intersects the zircon saturation curves calculated using M-values in (d) and calibrations in Boehnke et al. (2013) and Watson and Harrison (1983). Zircon saturation for the diorites is reached at 714 and 711 oC, for 3 and 6 wt.% H2O, respectively, where ~23% melt (for 3% H2O) or ~ 26% melt (for 6% H2O) remain. Tonalite reaches ~ 20% melt at ~650 oC solidus, where ~ 90% of the zircons are stable. d) M-value of residual melt used to determine the zircon saturation curve in (c). M-value for diorites steadily decrease to reach a value of 1.4 close to the solidus. For the tonalite M first decreases from a value of 1.45 at the liquidus (not shown) and then increases to ~1.4 at the solidus, due to stabilization of

Bt and Qtz. e) a(SiO2) and a(TiO2). f) Ti-in-zircon calculated using curves in (e) (solid lines) or assuming a fixed value of a(SiO2)=1 and a(TiO2)=0.7 (dashed lines; similar to Claiborne et al. (2010)). The differences between the two curves are small. Calculations use Ferry and Watson (2007). g) Zr content in melt, non-zircon phases and zircon as a function of temperature (note different scale in x-axis). Zircons are saturated close to the solidus for diorite. Diorite composition is similar to the basalt modelled by Lee and Bachmann (2014) (their Fig. 2b), but despite higher Zr in our starting composition, melt never reaches the > 300 ppm Zr in their model, peaking instead at ~ 150 ppm, due to significant intake of Zr in non-zircon minerals excluded in their model.

277x436mm (300 x 300 DPI)

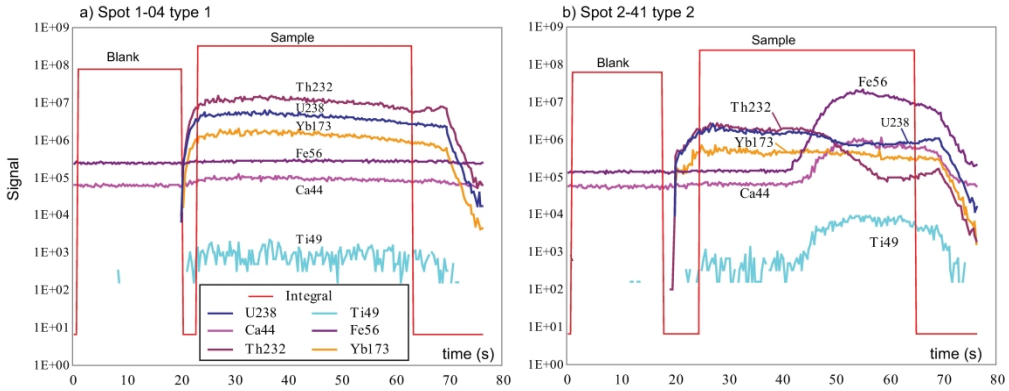

Fig. 15. Comparison of signal outputs from zircon analyses for sample 18DB01-4: a) spot 1-04 in a type 1 zircon, and b) spot 2-41 in a type 2 zircon. Data from (b) was excluded from consideration because of anomalous plateaus of Fe, Ca, Ti, and a sudden drop in Th, U counts.

274x105mm (600 x 600 DPI)

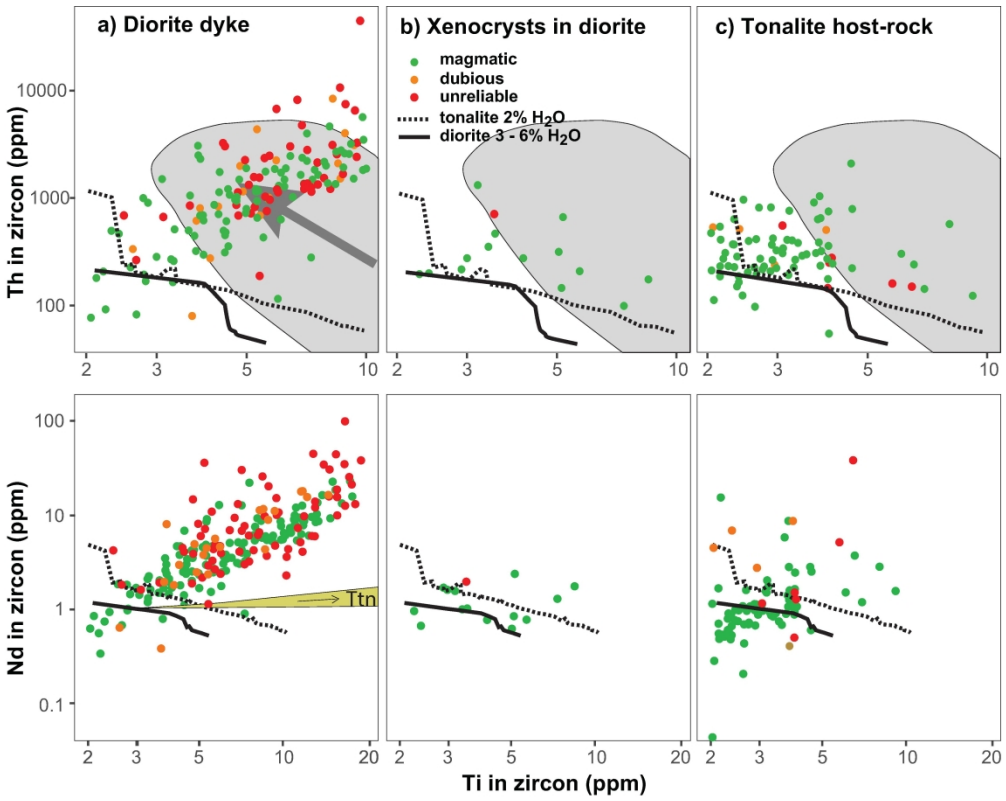

Fig. 16. Zircon chemistry modelling. a) Modelled zircon Th vs Ti composition for the diorite and tonalite (thick black lines) compared with data for zircons from diorite dykes, xenocrystic zircons in diorite and tonalite host rock zircons; b) same for Nd vs Ti. Analysed zircon grains are colour coded according to "reliability": if the zircon analysis has anomalous Fe or Ca signal it is deemed unreliable, if it has anomalous peaks or plateaus of Y, Th, Ti or HREE it is deemed dubious, otherwise it is classified as magmatic. Models are calculated as discussed in the text and uses Boehnke et al.'s (2013) model for saturation, but the results are very similar using Watson & Harrison (1983). For comparison (a) shows the approximate slope of the trend (thick grey arrow) defined by the data for granitic rocks in Claiborne et al. (2006), which is similar to the modelled slope for the tonalite (thick dashed line). The yellow band in (b) defines the field generated by mixing a zircon composition with 3 ppm Ti and 1 ppm Nd, with titanite with 24.4 % Ti and between 1000 and 10000 ppm Nd (Bruand et al., 2020). The band indicates that mixing with titanite is unlikely to explain the trend because it causes a stronger enrichment in Ti compared to Nd.

190x151mm (600 x 600 DPI)

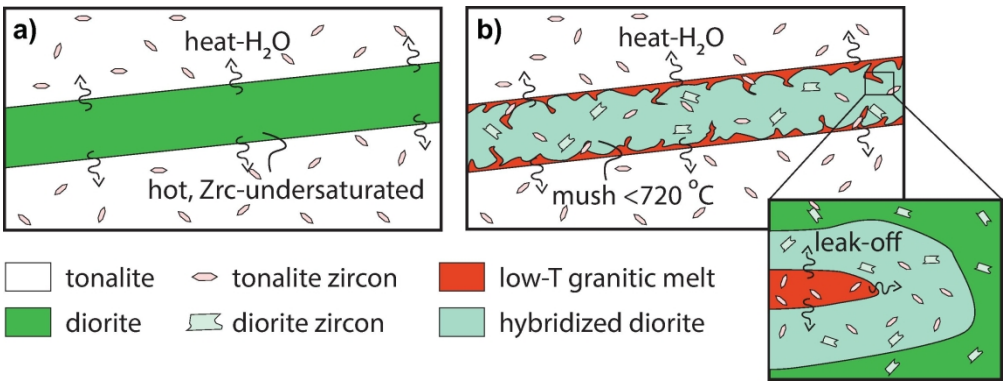

Fig. 17. Assimilation of host rock through anatexis, back-veining and mixing with zircon transfer. a) Original dioritic magma intrusion at temperatures above zircon saturation. As magma flows and cools, it heats-up the surrounding and releases H2O. b) The tonalite melts at relatively low temperatures lacking anhydrous peritectic minerals. Granitic dykelets derived from tonalite anatexis back-veins the diorite that is now a cool zircon-saturated mush. The mush deforms in a ductile fashion and granitic melt flow through the pore space of the mush (inset) transferring tonalite zircons and hybridizing the diorite. Zircon xenocrysts are preserved in the zircon-saturated diorite. Size of zircons is exaggerated.

126x47mm (600 x 600 DPI)